Master Thesis

Synthetic Natural Gas: A Study of CO_2 Methanation Kinetics in a Catalytic Plate Reactor

carried out for the purpose of obtaining the degree of

Diplom-Ingenieur_in (Dipl.-Ing.in oder DI)

submitted at TU Wien

Faculty of Mechanical and Industrial Engineering

by

Kevin KOFLER

Mat.No.: 01127812

under the supervision of

Ao.Univ.Prof. Dipl.-Ing. Dr.techn Michael, Harasek

Institute of Chemical, Environmental and Bioscience Engineering, E166

Wien, 19.01.2024

_____

Signature

Affidavit

I declare in lieu of oath, that I wrote this thesis and carried out the associated research myself, using only the literature cited in this volume. If text passages from sources are used literally, they are marked as such.

I confirm that this work is original and has not been submitted for examination elsewhere, nor is it currently under consideration for a thesis elsewhere.

I acknowledge that the submitted work will be checked electronically-technically using suitable and state-of-the-art means (plagiarism detection software). On the one hand, this ensures that the submitted work was prepared according to the high-quality standards within the applicable rules to ensure good scientific practice "Code of Conduct" at the TU Wien. On the other hand, a comparison with other student theses avoids violations of my personal copyright.

Wien, 19.01.2024 _____

Place and Date

_____

Signature

Acknowledgement

First of all I want to thank my mother Melissa who supported me over all those years through every up and down. Without you my studies would not have been possible. Thank you and love you. Second, I would like to thank my other family members, Benjamin & Albert and my grandparents Mima, Pepa and Oma.

Next, I just want to say thank you to all my friends at University, it is a pleasure knowing you, you formed my personality massively and I am so thankful for this.

Last but not least I want to say thank you to my colleagues and friends at McGill University. First of all my mentors Jose and Jan even though we did not manage to stay in contact. I hope you are doing well. Second, my lab partners Ali, Kanchan (thanks for saying I should not be grumpy because it does not suit me), Daniel, Pranjal, Jessica and Gabriel.

English Abstract

‘World Scientists´ Warning to Humanity’ in 1992 was not taken seriously thus, research 25 years later is needed more than ever to stop climate change. Excess electricity in daily and seasonal shifts needs to be stored and easily available. Therefore, several concepts are investigated simultaneously whereby, one promising concept is a Power-to-Gas process.

An important part of Power-to-Gas is the conversion of carbon dioxide to synthetic natural gas. To increase efficiency of the reaction it is crucial to gain knowledge about reaction kinetics of CO_2 methanation to develop better catalysts.

The investigation of the chemical reaction and its rate determining step was done by experiments with a Ni-Al_2O_3 catalyst in an optical accessible reactor. The design of experiments was stated for a temperature range from 300 to 450 °C and a flowrate from 55 to 220 $ml_N \cdot min^{-1}$.

Subsequently, eleven rate equations were built up based on two different reaction mechanism (mechanism A and B). It was shown how to use them for modeling and the determination of kinetic parameters.

Finally, two models with a rate determining step which includes either a COH* or a COOH* complex were investigated within this thesis. Hereby, the Ni-Al_2O_3 catalyst was covered with a hydroxyl species in form of OH*, hydrogen H*, the COX* complex or had a free active side (*).

The modeling results indicate a slight trend towards the COOH* complex as the rate determining step which is part of mechanism B. Even though the residual sum of squares is within a small range for both estimations the highest posterior density interval for the activation energy of the COH* formation is significantly higher and therefore more uncertain.

Deutsche Kurzfassung

Die „Warnung der Wissenschaftler an die Menschheit“ im Jahre 1992 wurde nicht ernst genug genommen und daher ist es 25 Jahre später wichtiger den je den Klimawandel zu stoppen. Überschussenergie aus täglichen und saisonalen Änderung muss dafür gespeichert werden und leicht verfügbar sein können. Aktuell wird an mehreren Konzepten geforscht, wobei das Power-to-Gas Konzept ein vielversprechender Ansatz ist.

Ein wichtiger Teil von Power-to-Gas ist die Umwandlung von Kohlendioxid in synthetisches Erdgas. Um den Wirkungsgrad des Prozesses zu erhöhen, ist es notwendig die Reaktionskinetik der CO_2 Methanisierung besser zu verstehen und bessere Katalysatoren zu entwickeln.

Zum Erreichen dieses Ziels wurde ein optisch zugänglicher Reaktor mit einem Ni-Al_2O_3 Katalysator verwendet. Die Versuchsplanung erstreckt sich über einen Temperaturbereich von 300 bis 450 °C und die Variation im Volumenstrom beträgt 55 bis 220 $ml_N \cdot min^{-1}$.

In weiterer Folge wurden elf Reaktionsgleichungen, basierend auf zwei Reaktionsmechanismen (Mechanismus A und B) aufgestellt und gezeigt, wie diese zur Modellierung und Bestimmung von kinetischen Parametern verwendet werden können.

Schlussendlich wurden zwei Modelle, die als geschwindigkeits-bestimmenden Schritt entweder einen COH* oder COOH* Komplex aufweisen, in dieser Arbeit behandelt. Der Ni-Al_2O_3 Katalysator war dabei bedeckt durch eine Hydroxyl Gruppe in Form von OH*, Wasserstoff H*, dem COX* Komplex oder wies eine freie aktive Seite auf (*).

Die Ergebnisse der Modellierung dieser beiden Komplexe zeigten einen leichten Trend in Richtung der COOH* Gruppe als geschwindigkeits-bestimmenden Schritt. Auch wenn die Quadratsumme der Residuen beider Modelle sehr ähnlich sind, ist das Glaubwürdigkeitsintervall für die Aktivierungsenergie des COH* Komplexes signifikant höher und daher das Ergebnis ungewisser.

Table of Content

Chapter 1

1 Introduction

1.1 Motivation

'World Scientists´ Warning to Humanity' – was the slogan of a publication by the Union of Concerned Scientists in 1992 [1]. This manifesto which was endorsed by more than a thousand independent scientists showed concern about the threat to Earth's ecosystem by global warming and emphasized to reduce greenhouse gas emissions and deforestation [1]. As of November 2017, 25 years later, a 'Second Notice' of this organisation pointed out that most of their claims have not been implemented by this day [2].

To reduce the effect of greenhouse gas emissions on global warming the European Council set out a target of 27 % for renewable energy consumption by the year 2030 [3]. Likewise, Canada's 2030 target to reduce greenhouse emissions by 30 % below levels of 2005 has been declared in the Pan-Canadian Framework on Clean Growth and Climate Change [4]. However, energy from renewable sources like wind or sunlight are not easy to predict and cannot produce energy on demand. Due to this, a decoupling of production and consumption is inevitable to challenge future energy goals. Depending on regional circumstances there are several different possibilities to store renewable energy sources. Advantages and disadvantages of different storage technologies were discussed in length over the last couple of years [5]–[8]. However, a promising method to ensure long term power

supply is the Power-to-Gas (P2G) concept. A schematic overview about this concept is shown in Figure 1-1.

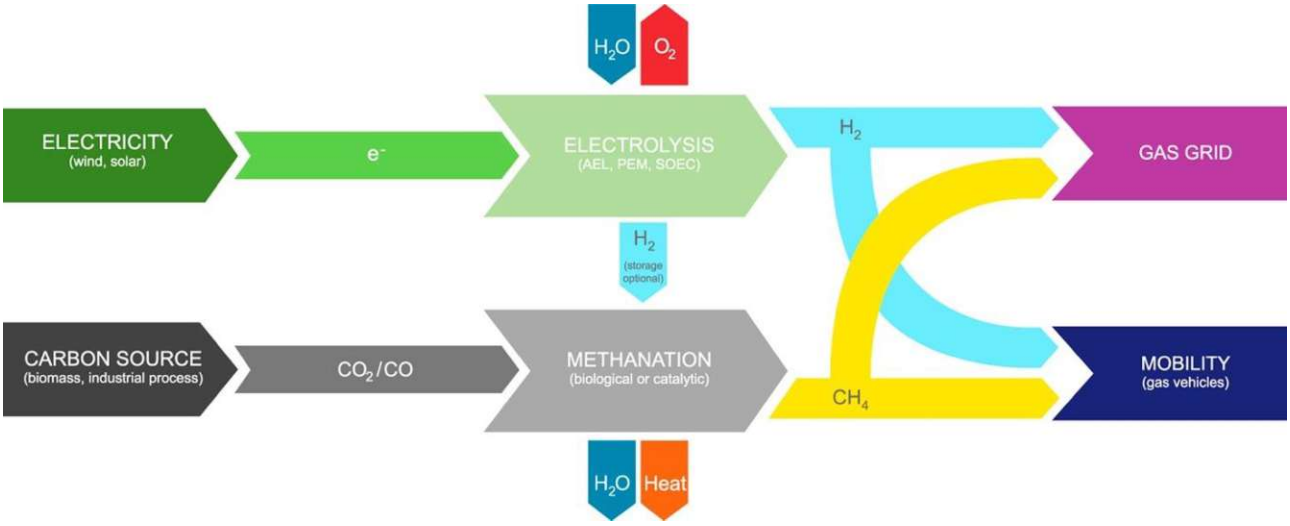

Figure 1-1 Schematic flow diagram of a Power-to-Gas process [9] where H_2 produced by excess energy and CO_2 from carbon source are used for the methanation process

Excess electricity from solar photo voltaic or wind turbine source is used in the P2G process to produce hydrogen by water electrolysis. An optional storage of hydrogen can be provided by the existing natural gas pipeline system, conventional pressure tanks or as metal hydrates. Low hydrogen storage capacities in natural gas pipelines and a high energy input to pressurize hydrogen up to 200 bar for storage in metal hydrates are responsible to take a further conversion of H_2 to methane into account [10]. A requirement for this process step is a high concentrated carbon oxide source (e.g. biogas, industrial process etc.). Such produced methane or Synthetic Natural Gas (SNG) is fully capable to be stored and transferred in natural gas grid systems. Furthermore, it could be an excellent way to bypass long term carbon capture and storage. However, the process step to convert carbon oxides into SNG is challenging and not fully understood yet. This thesis focuses on kinetics of a thermo-chemical reaction of carbon dioxide to methane. Other pathways like electro- or bio-chemical methanation are investigated in other research projects. The production of SNG requires a deep knowledge of catalyst and reactor design, heat integration and as mentioned above usable carbon oxide sources have to be further evaluated. For this work an optical accessible catalytic plate reactor with spatially resolved measurement techniques was used to study the CO_2 methanation reaction. The setup allows to determine the gas composition and catalyst surface temperature profile along the reactor axis by means of a small movable sampling capillary and infrared thermography, respectively. A plate reactor combines excellent heat integration and scaling-up is based on a modular way.

1.2 Organization of Thesis

This thesis is divided into four parts. An overview of the main covered topics is shown below:

Chapter 2 gives a theoretical background of the CO_2 methanation and reaction kinetics as well as catalysts and reactor development.
Chapter 3 provides information about preliminary work such as catalyst preparation and plate coating up to an implementation of experimental procedures.
Chapter 4 shows and discusses results of all experiments and how to set up a computational model. A comparison of experimental and modeled gas compositions finishes this chapter.
Chapter 5 contains a short glance at a further reaction mechanism from literature and recommendations for further research.

Chapter 2

2 Theoretical Background

The catalytic conversion of carbon dioxide and hydrogen to methane and water was discovered first by Paul Sabatier at the beginning of the 20th century [11]. Since then, many aspects of this process have been thoroughly investigated [12]–[14]. A summarize of relevant aspects is given in the following subchapters.

2.1 Chemistry and Thermodynamics

The hydrogenation of CO_2 can be described by three main reactions: The general methanation equation (Rx 1), a competing reversed water-gas shift reaction (Rx 2) and a subsequent CO methanation (Rx 3).

$4\,H_2 + CO_2 \leftrightarrow CH_4 + 2\,H_2O$	$\Delta H_R^0 = -164.65\ \mathrm{kJ \cdot mol^{-1}}$	CO_2 methanation	**Rx 1**
$H_2 + CO_2 \leftrightarrow CO + H_2O$	$\Delta H_R^0 = 41.16\ \mathrm{kJ \cdot mol^{-1}}$	Reversed WGS	**Rx 2**
$3\,H_2 + CO \leftrightarrow CH_4 + H_2O$	$\Delta H_R^0 = -205.81\ \mathrm{kJ \cdot mol^{-1}}$	CO methanation	**Rx 3**

It has to be noticed that Rx 1 is a linear combination of Rx 2 and Rx 3. Thus, it is not totally clear if CO_2 is converted directly into CH_4 or the water-gas shift reaction works as an intermediate step. However, as additional information the heat of reaction ΔH_R^0 is given which can be calculated directly from the ideal gas enthalpy of formation $\Delta H_{f,i}^0$. The data for the correlation is provided by DIPPR 801 database [15]. The heat of reaction shows whether a reaction is exothermic ($\Delta H_R^0 < 0$) or endothermic ($\Delta H_R^0 > 0$). Thus, exothermic reactions are thermodynamically favoured at lower temperatures. To investigate the preferred temperature area of each reaction a closer look at the change of reaction enthalpy over temperature has to be taken into account. For a certain temperature equation 2-1 is used to calculate a corresponding heat of reaction.

$$\Delta H_R(T) = \Delta H_R^0 + \int_{T_0}^{T} \nu_i \cdot c_{p,i} \cdot dT \qquad \textbf{2-1}$$

The reference temperature T_0 is defined at 298.15 K (25 °C), ν_i stands for the stoichiometric coefficient and $c_{p,i}$ for the specific heat capacity of each species respectively. The corresponding values for $c_{p,i}$ are derived from DIPPR 801 database [15].

The correlation between temperature and chemical equilibrium constant K_P is described by van't Hoff's equation (2-2). As shown above the heat of reaction also changes with temperature thus a simple integration of the following equation is not possible. Hence a program named HSC Chemistry is used to calculate the equilibrium constant.

$$\frac{\partial ln(K_p)}{\partial T} = \frac{\Delta H_R}{\Re \cdot T^2} \qquad \textbf{2-2}$$

The results for ΔH_R and K_P are shown in Figure 2-1 (A) and (B). The change in the heat of reaction (A) of the CO_2 methanation is bigger than the one of the reversed water-gas shift reaction. The reason for this is the high specific capacity of hydrogen. However, as Figure 2-1 (B) shows the equilibrium constant of the methanation is much higher at lower temperatures and decreases constantly as temperature rises. A contrary behavior for the reversed WGS is noticeable. This corresponds to the statement which was mentioned before as exothermic reaction favours low temperatures compared to endothermic reactions. As shown, at a temperature of 600 °C upwards the K_P value of the reversed water-gas shift reaction is higher than the equilibrium constant of methanation.

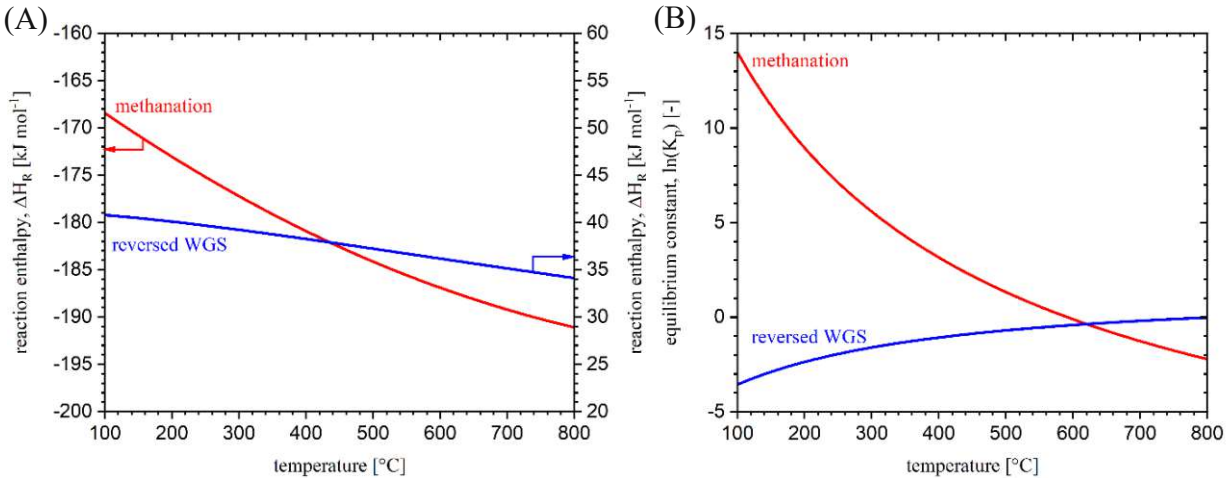

Figure 2-1 Change of reaction enthalpy (A) and equilibrium constant (B) according to van't Hoff's equation for CO_2 methanation and reversed WGS over temperature (100 – 800 °C)

Results of molar fractions at thermodynamic equilibrium of the CO_2 methanation are illustrated in Figure 2-2 using minimization of Gibbs energy. The influence of temperature is shown in Figure 2-2(A). As can be seen, methane production is thermodynamically favoured at lower temperatures and declines as temperatures increases. Compared to this the influence of higher pressures as shown in Figure 2-2(B) is not as big but still noticeable. A short glance at Rx 1 shows that with the conversion of carbon dioxide and hydrogen to methane and water a volume contraction of 40 % occurs, thus favoring the reaction products at higher pressure according to le Châtelier's principle [16]. A stoichiometric H_2/CO_2 ratio of 4:1 is used for Figure 2-2. A deviation of the stoichiometric ratio was also investigated revealing comparable temperature and pressure dependences (not shown here).

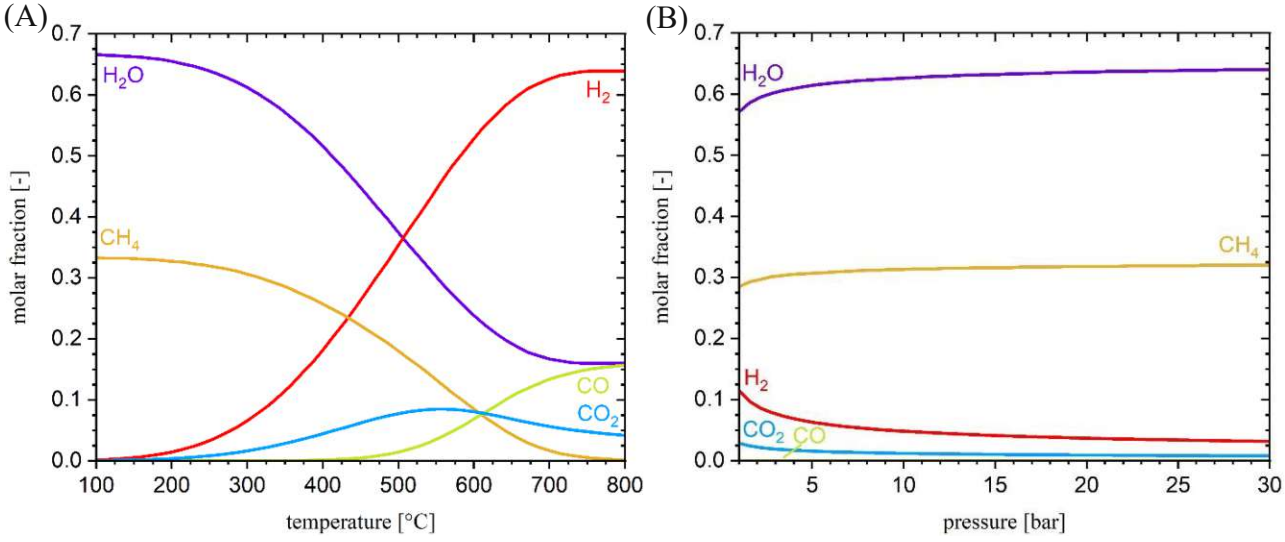

Figure 2-2 Change of equilibrium composition for CO_2 methanation at a stoichiometric H_2:CO_2 ratio of 4:1. Graph (A) shows a fixed pressure of 1.0 bar and a temperature range of 100 to 800°C, Graph (B) is at a fixed temperature of 350 °C and a pressure range of 1.0 to 30.0 bar

2.2 Reaction Mechanisms

The correct reaction mechanism for the methanation of CO_2 is still subject to debates. Different approaches and thus experimental conditions (e.g., temperature, pressure, choice of catalyst) might be responsible for this [17]. Furthermore, no spatially resolved measurement was taken into account so the gas composition was only measured at the exit of a reactor. This leads to a deviation of the chemical equilibrium and thereby to an increasing inaccuracy for the determination of a reaction mechanism. Thus, to gain deeper knowledge of a reaction mechanism a spatially resolved measurement is advantageous.

In general, a heterogeneous catalyzed reaction follows the pathway which is shown in Figure 2-3. First, reactants diffuse from the bulk to the catalyst phase where molecules are adsorbed to the surface. Then, the reaction step takes place followed by desorption of products and a diffusion to the bulk phase.

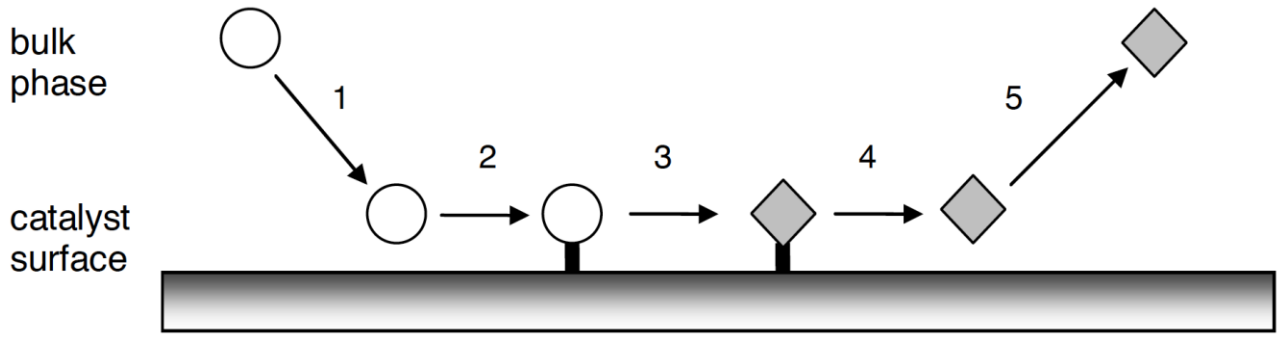

Figure 2-3 Reaction pathway of heterogeneous catalyzed reaction: (1) diffusion of educts to catalyst surface (2) adsorption (3) and reaction of educts (4) desorption (5) diffusion of products to bulk phase [17]

For a kinetic study, all five elementary steps must be considered and the overall reaction rate is a summation of the whole pathway. In theory one of these steps is much slower than all the others which can be referred as rate determining step (RDS). Besides of the RDS the difference in reactant concentrations in the bulk and on the catalyst surface needs to be considered in order to avoid mass transfer limitation on the reaction rate. Mass transfer limitation can occur if diffusion of educts to the catalyst (step 1) is low compared to the chemical reaction on the catalyst surface itself (step 3). Likewise, the diffusion of products to the bulk (step 5) could also lead to an adverse effect on reaction rate. In detail, a slow diffusion step leads to a chemical reaction closer to equilibrium. Thus, the driving force of reaction is lower which leads to an effect that the overall kinetics of chemical

reactions is not controlled by the reaction itself but by mass transfer. So, a rate determining step which is controlled by mass transfer must be avoided for kinetic investigations.

The detailed reaction pathway and reaction mechanism is still much debated. In the literature there are two different reaction theories discussed [17]–[20]. The two main mechanism, (A) the direct and (B) the hydrogen assisted mechanisms are illustrated in Figure 2-4. The first reaction mechanism (*mechanism A*) works by dissociation of CO_2 on the catalyst surface to CO and which subsequently leads to adsorbed carbon (C*). A stepwise hydrogenation of C* until CH_4 follows as shown in Table 2-1. It must be noted that the hydrogenation of carbon dioxide does not follow exactly the pathway which is shown below, it is rather an accumulation of all possible steps. The rate-determining step for the CO methanation has been investigated by Kopyscinski et al. and is adopted by Hernandez Lalinde for the hydrogenation of CO_2 [20].

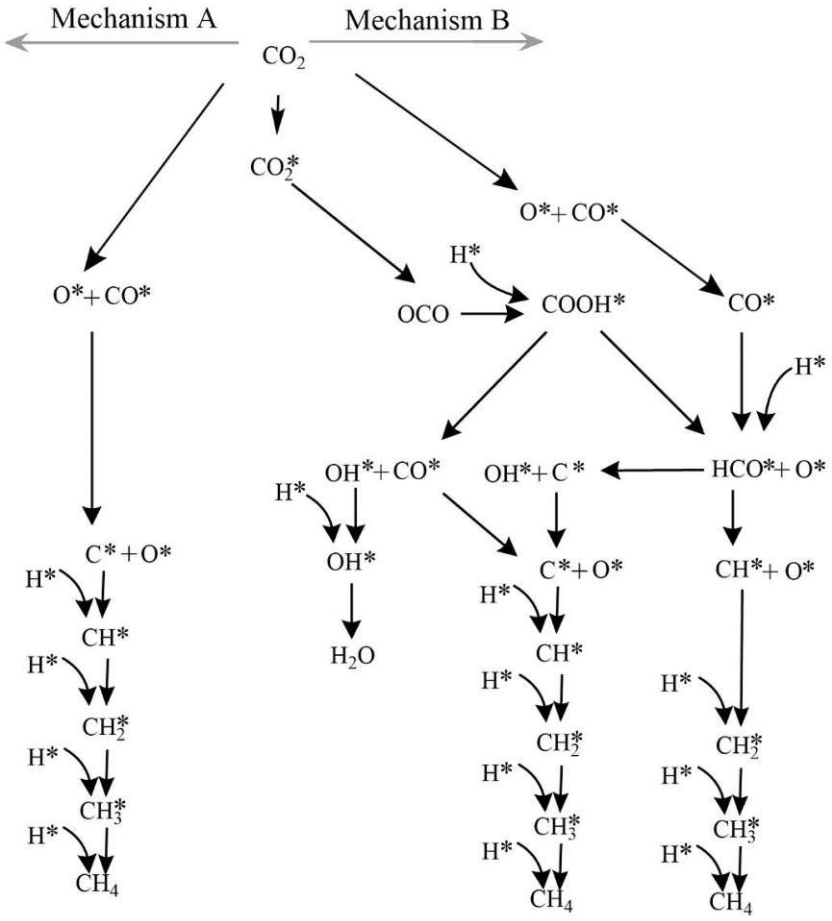

Figure 2-4 Possible CO_2 methanation reaction pathways (C* refers to adsorbed species). Mechanism A works by a stepwise dissociation of CO_2 to carbon and mechanism B with a formation of oxygenates (COHx) [20]

Table 2-1 Step-by-step reaction pathways for mechanism A with possible rate-determining steps (RDS)

H_2	+ 2*	↔	2 H*			Dissociation and adsorption of H_2	**A1**
CO_2	+ *	↔	CO_2*		RDS	Adsorption of CO_2	**A2**
CO_2*	+ *	↔	CO*	+ O*	RDS	Dissociation of CO_2	**A3**
CO*		↔	CO(g)	+ *	RDS	Desorption of CO	**A4**
CO*	+ *	↔	C*	+ O*	RDS	Dissociation of CO to surface C	**A5**
C*	+ H*	↔	CH*	+ *	RDS	Hydrogenation of C	**A6**
CH*	+ H*	↔	CH_2*	+ *	RDS	Hydrogenation of CH	**A7**
CH_2*	+ H*	↔	CH_3*	+ *	RDS	Hydrogenation of CH_2	**A8**
CH_3*	+ H*	↔	CH_4*	+ *		Hydrogenation of CH_3	**A9**
CH_4*		↔	CH_4(g)	+ *		Desorption of CH_4	**A10**
O*	+ H*	↔	OH*	+ *		OH formation	**A11**
OH*	+ H*	↔	H_2O*	+ *		H_2O formation	**A12**
H_2O*		↔	H_2O(g)	+ *		H_2O desorption	**A13**

Table 2-2 Step-by-step reaction pathways for mechanism B with possible rate-determining steps (RDS)

H_2	+ 2*	↔	2 H*			Adsorption of H_2	**B1**
CO_2	+ *	↔	CO_2*		RDS	Adsorption of CO_2	**B2**
CO_2	+ 2*	↔	CO*	+ O*	RDS	Adsorption of CO_2	**B3**
CO_2*	+ H*	↔	HCOO*	+ *	RDS	Formation of formates	**B4**
HCOO*	+ *	↔	HCO*	+ O*	RDS	Dissociation of formates	**B5**
CO*	+ H*	↔	HCO*	+ *	RDS	Formation of formyl	**B6**
HCO*	+ *	↔	CH*	+ O*	RDS	Formation of CH species	**B7**
CH*	+ H*	↔	CH_2*	+ *	RDS	Hydrogenation of CH	**B8**
CH_2*	+ H*	↔	CH_3*	+ *	RDS	Hydrogenation of CH_2	**B9**
CH_3*	+ H*	↔	CH_4*	+ *		Hydrogenation of CH_3	**B10**
CH_4*		↔	CH_4(g)	+ *		Desorption of CH_4	**B11**
O*	+ H*	↔	OH*	+ *		OH formation	**B12**
OH*	+ H*	↔	H_2O*	+ *		H_2O formation	**B13**
H_2O*		↔	H_2O(g)	+ *		H_2O desorption	**B14**
H_2	+ 2*	↔	2 H*			Adsorption of H_2	**B15**

* free active side
CO* Adsorbed species (e.g. adsorbed carbon monoxide)
RDS Rate-determining step (proposed from literature)

A second theory (*mechanism B*) works with a formation of oxygenates (COH_x). Research showed that carbon monoxide does not dissociate in the presence of hydrogen because of a high energy barrier. In contrast to this, the energy barrier to break the C – O double bond is much lower for an oxygenated compound (e.g., HCOO) [17]. However, a formate is assumed to be the most complex oxygenated species. A list of all possible steps for reaction mechanism B is shown in Table 2-2.

2.3 Methanation Catalysts

The choice of a proper catalyst is essential for the methanation of carbon oxides and has been investigated in the past. A review of novel and heterogeneous catalysts is given by Frontera et al [21]. The most important properties for a catalyst are a high selectivity and long-term stability. Group VIII metals like cobalt (Co), iron (Fe), nickel (Ni), rhodium (Rh) and ruthenium (Ru) are promising candidates, especially Ru and Ni are favored in terms of high activity. From an economic perspective costs for ruthenium are relatively high so nickel is the material of choice even though the stability of Ni for a catalyzed CO_2 methanation is not proven on commercial scale yet [22]. Beside the active metal itself, the catalyst support is very important as it provides the high surface area, mechanical strength, dispersion of the active phase and may assist in suppressing of sintering of the metals [22], [23]. The most common support materials are metal oxides (e.g., Al_2O_3, CeO_2, SiO_2, TiO_2) [24]. Tian et al. described four different approaches for encapsulated catalyst support: (1) core@shell, (2) core@tube, (3) mesoporous structure and (4) lamellar structure [25]. However, an ordered mesoporous structure is a promising candidate because it combines all positive properties, a high surface area, good mechanical strength and a well-dispersed catalyst. In addition, a pore size of 2 to 50 nm provides sufficient accessibility for reactants to enter the support structure [26].

A common way to synthesize ordered mesoporous catalysts (OM) is the evaporation-induced self-assembly method (EISA) [27]. EISA works as a one pot technique where a copolymer (e.g., Pluronic P123) is dissolved in a polar organic liquid (e.g., ethanol). A non-polar solvent would lead to a non-mesoporous structure [22]. After an acidification of the solution the support material as well as the metal precursors are mixed together. An acidic environment is essential for the synthesis of OM because polymerization and cross–linking are too fast at a pH of 6 – 8.5 and this would lead to a non-ordered structure [22]. Subsequent drying and calcination steps are required to burn the copolymer, thus, to form ordered mesopores and to achieve a good metal to support adhesion. The influence of calcination temperature is an important parameter on the catalyst performance and has been recently investigated [22], [28]. An overview of the results by A. Aljishi et al. is given in Table 2-3. It has to be noted that a calcination ensures also that the catalyst does not change its properties during reaction.

Table 2-3 Influence of calcination temperature on total and mesoporous surface area (Ni loading = 15 wt.%, acid HNO_3), adapted from [22]

Sample	T_{cal} [°C]	S_{BET} [$m^2 \cdot g^{-1}$]	S_{Meso} [$m^2 \cdot g^{-1}$]
OMA-15Ni-400	400	140	124
OMA-15Ni-500	500	242	234
OMA-15Ni-700	700	206	198
OMA-15Ni-900	900	123	115

OMA Ordered mesoporous alumina supported catalyst
S_{BET} BET total specific surface area obtained from adsorption data (p/p_0 range 0.05-0.2)
S_{MESO} mesoporous surface area determined via subtracting the microporous surface area

2.4 Reactor Concepts

A well-designed reactor is inevitable for the methanation of carbon oxides due to the exothermic nature of the reaction and the intermittency of the hydrogen production from renewable energy sources. Therefore, the major challenges are the temperature control and possible fluctuations in the feed gas composition. As shown in chapter 2.1, temperatures below 500 °C are required to avoid low methane yield due to equilibrium limitations. Besides, high temperatures may lead to sintering and increased carbon deposition and thus to catalyst deactivation.

For the methanation of CO_2 there are four basic reactor concepts applicable: (1) fixed bed reactor, (2) fluidized bed reactor, (3) microchannel reactor and (4) plate reactor [17], [29], [30]. Fluidized bed reactors are favoured to achieve isothermal behavior as they have an excellent heat transfer capacity. Nevertheless, there is a disadvantage concerning flexible loading, fast shut down and turn on and scale-up [31]. To stabilize a fluidized bed reactor a certain minimum fluid velocity is necessary. A lack of reactants leads to a higher amount of inert gases which leads subsequently to a useless energy input to heat up the inert gas. However, a major problem for the fixed bed technology are hotspots and therefore formation of coke and catalyst instability. For microchannel- and plate reactors the formation of coke and catalyst stability is not determined yet, though. In terms of heat removal, a plate reactor is the most promising technology. It is built like a stacked heat exchanger where one level operates as a reactor and the other as a cooler respectively. The modular design is additionally not difficult to scale up and fluctuations can be controlled easily by switching on and off different modules. An overview of all basic concepts and their properties is given in Table 2-3.

Table 2-4 Advantages and disadvantages of different reactor concepts

	Fixed bed	**Fluidized bed**	**Microchannel**	**Plate**
Temperature	High	Low	High	High
Fluctuation	No	No	Yes	Yes
Hot spots	Possible	No	No	No
Coke formation	Possible	Not possible	n/a	n/a
Catalyst stability	Not stable	Stable	n/a	n/a
Scale-up	Easy	Difficult	Easy	Easy

n/a data not available

It has to be noted that there are more complex reactor designs (e.g., Lurgi, TREMP) which operate with two or more fixed bed reactors and an intermediate cooling step or even an integrated heat exchanger. A summary of current projects and technologies were evaluated by Kopyscinski et al. [29] and Rönsch et al [30].

Chapter 3

3 Experimental Procedures

3.1 Reactor Setup

For the study of CO_2 methanation kinetics a catalytic plate reactor (CPR) was used. A schematic P&ID drawing of the reactor is shown in Figure 3-1. The reactants, carbon dioxide and hydrogen (purity of 99.99 % and 99.999 %, respectively) were mixed together with argon. A Vögtlin red-y smart controller GSC was used as a mass flow controller for all inlet gases. Before entering the reactor, the reactants were preheated to a temperature of approximately 250 °C. Below the reactive channel, six INCOLOY® heating cartridges evenly heated up the CPR to its reaction temperature, whereby two cartridges on the left, in the middle and on the right are linked together, respectively. Between the heating zone and the inner channel three K-Type thermocouples (Omega KMTXL) were measuring the temperature. The pressure inside the reaction chamber was controlled by an Equilibar LF backpressure regulator. The dimensions of this channel are 100 mm in length, 40 mm in width and 5 mm in height. In the CPR a stainless steel capillary was located in a height of 2.5 mm above the catalytic plate. A more detailed view of the reactor cross-section, the possible capillary height placement and its inlet is shown in Figure 3-2 (A) to (C). Two quartz glass plates sealed the reactive channel as well as the heating channel and granted optical accessibility. For a spatially resolved measurement of the gas composition the capillary was connected to a mass spectrometer (Pfeiffer GSD 301). The movement of the capillary was provided by an attached step motor with a step size up to 0.2 mm. The outlet gas tube was also heated up to prevent a condensation of the water gas before entering an appropriate condenser. A hand valve at the outlet was used to control the pressure

inside the reactor. The measurement data of several thermocouples, a pressure sensor and the position of the step motor was connected by LabVIEW™. Furthermore, a near-infrared camera (FLIR SC2500) was used to determine the catalyst surface temperature along the reactor. The exact mechanism is described in chapter 3.2.4 and 3.3.2, respectively.

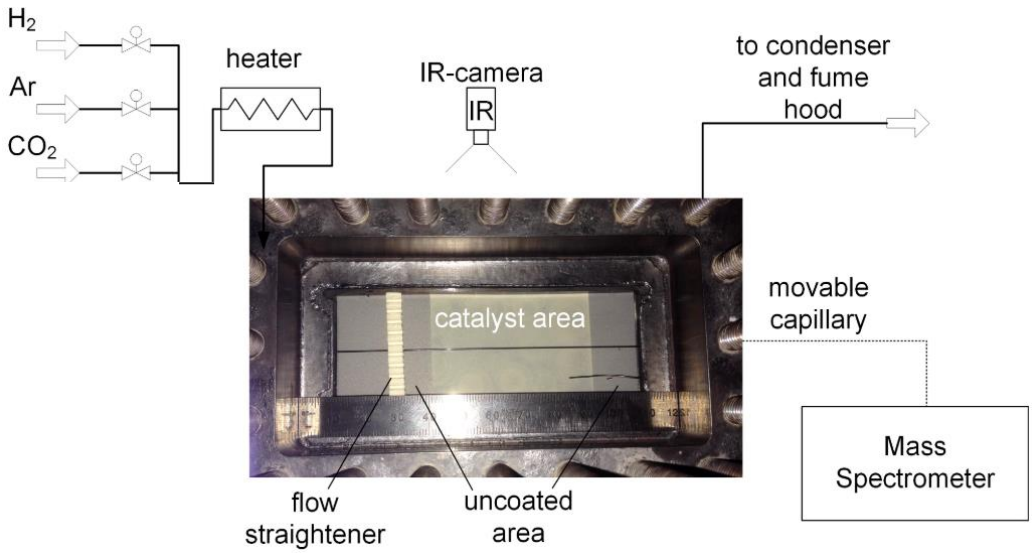

Figure 3-1 Schematic drawing of the catalytic plate reactor setup, adapted from [32]. Gas mixing and pre heating of gas flow takes place before entering the reactor. After the reactor exit produced water condenses before the fume hood. Temperature pressure and gas mixture measured in line.

The heating channel operated in counter flow direction to level the temperature along the reactor more evenly. On the lateral face of the reactor three openings could be used to insert measurement devices (e.g., thermocouples, capillary). Gas in- and outlet are located alongside the reactor.

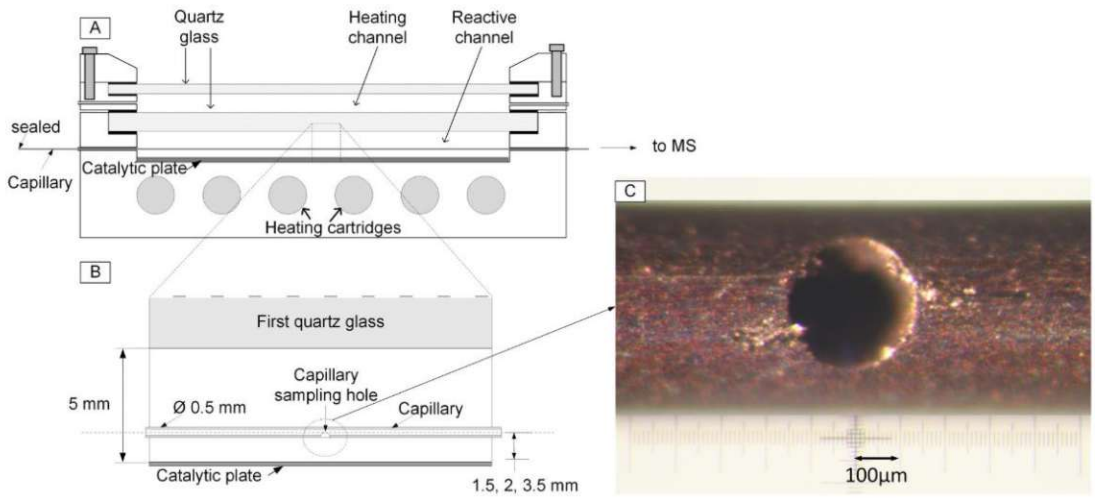

Figure 3-2 Schematic cross-section of reactor (A) with two quartz glasses for optical accessibility which are sealing the heating channel and the reactive channel. Six heating catridges placed below the catalytic plate; (B) Detailed view of the reactive channel with capillary placement; (C) Capillary inlet with dimensions [32]

To investigate the area of the reactor with a fully-developed velocity profile a computational fluid dynamic (CFD) analysis was performed by a member of the CPE team (Figure 3-3). At the beginning of the reactor a turbulent flow regime in form of swirls occurred for a length of approximately 2 cm. After a transition area laminar straight streamlines go along the plate starting at a length of 3 to 9 cm. Thus, the catalyst coated area was fully covered in a laminar flow regime. A more detailed look of the coated plate is presented in chapter 3.2.2.

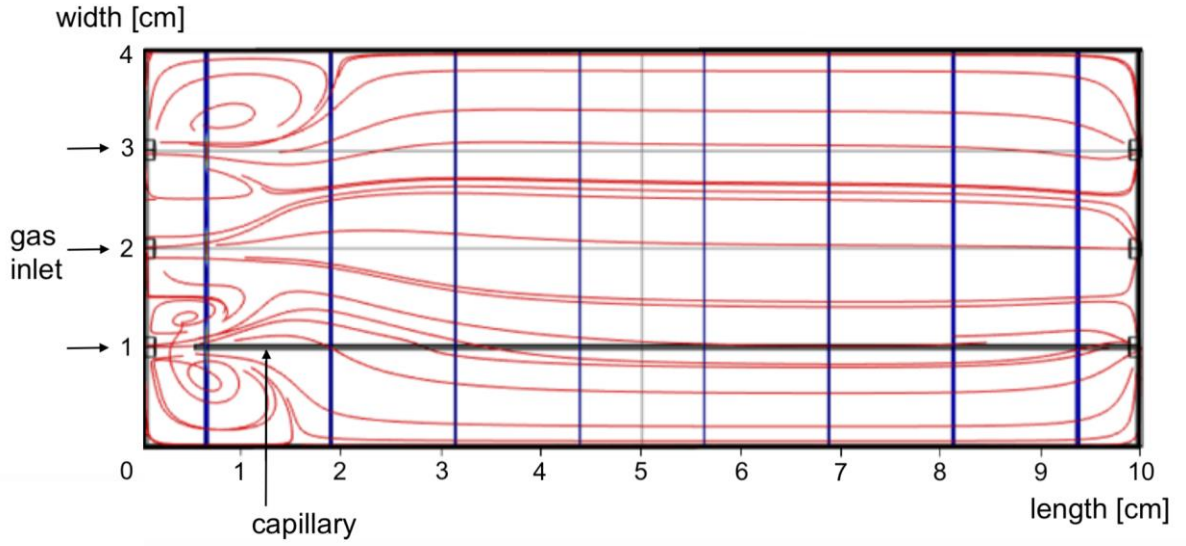

Figure 3-3 Streamlines inside the reactor with capillary insertion , adapted from [20] with a turbulent area until a length of 2 cm.

3.2 Preliminary work

3.2.1 Catalyst preparation

For this thesis a one pot, evaporation-induced self-assembly method (EISA) developed by Alijshi et al. was used to synthesize the catalyst [22]. In detail, ordered mesoporous nickel catalyst with alumina support were prepared. The samples were named OMA-15Ni-500 where OMA refer to **O**rdered **M**esoporous **A**lumina support, 15Ni referes to the nickel loading in wt.% and 500 to the calcination temperature in °C. Catalysts calcined at 500 °C were used in the current work, even though a calcination temperature of 700 °C showed a better performance in terms of CO_2 conversion and CH_4 selectivity in the fixed bed reactor [22].

To synthesize 1 g of catalyst, 1.05 g of triblock copolymer Pluronic® P123 (Sigma Aldrich), a soft template surfactant, was mixed with 20 ml anhydrous ethanol (Les Alcools de commerce) and stirred at moderate speed for half an hour. Subsequently 1.6 ml of nitric acid (67 wt.%, Sigma Aldrich) was added dropwise to the homogenous solution. To achieve the disired nickel concentration and alumina support approximately 3.22 g of aluminum isopropoxide (> 98 %, Sigma Aldrich) and around 0.76 g of nickel (II) nitrate hexahydrate (> 98.5 %, Sigma Aldrich) was added slowly to the mixture. Covered with Parafilm® the slurry was stirred at a constant speed of 620 rpm for at least six hours until a homogenous solution was obtained. After drying the mixture in an oven for 48 h at 60 °C the catalyst was transferred from a beaker into a combustion boat. A subsequent calcination was performed at a heating rate of 1 °C · min^{-1} until the desired temperature of 500 °C was reached. During the calcination process the soft template should evaporate and a hexagonal shaped mesoporous tube of aluminum oxide remains as support structure. A mass balance was performed to determine the yield of the catalyst synthesis as well as the nickel loading.

The yield should be in a range of 0.95 to 0.99 but an analysis of the mass balance shows values higher than one, as shown in Figure 3-4. Eventual measurement errors can be ruled out because statistical scattering of a balance requires results above as well as below an expected value. So a possible explanation could be a contamination because of the copolymer, ethanol or nitric acid even though their boiling points are approximately 149.0 °C, 78.3 °C and 120.5 °C, respectively [15], [33], [34]. However, a step of manual crushing combined with subsequent sieving completed the synthesis process. A schematic overview of the catalyst production is given in Figure 3-5. The final particle size classes are < 20 µm, 20 – 45 µm, 45 – 90 µm, 90 – 125 µm and > 125 µm whereby only particles between 20 – 45 µm were used for the catalytic plate reactor. A possible inhibition of mass transfer

kinetics was the reason not to use particle sizes bigger than 45 µm. A health risk for particles < 20 µm was the reason to reject this catalyst.

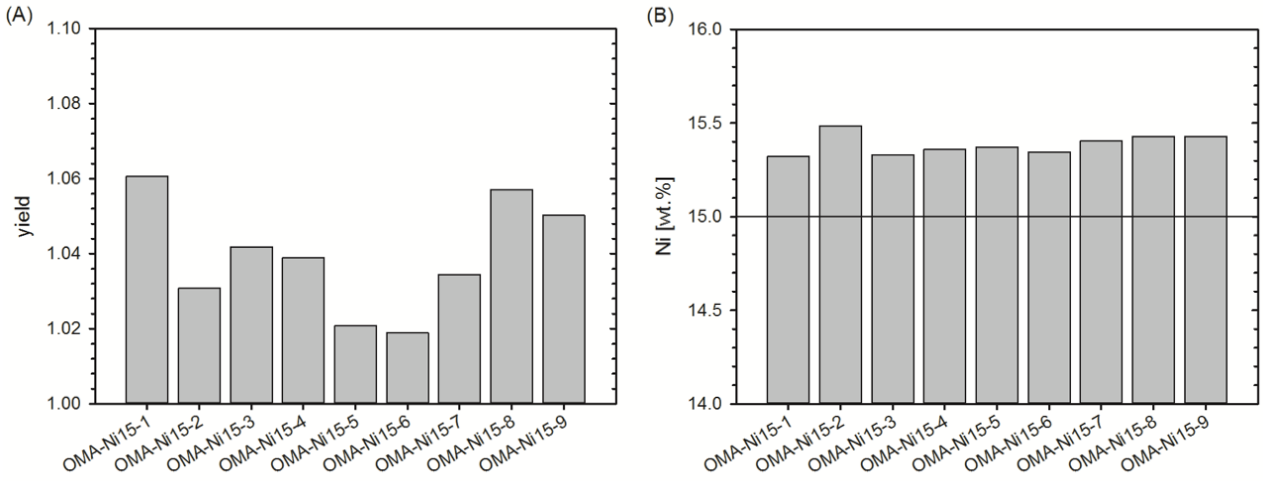

Figure 3-4 Yield (A) and nickel wt.% (B) of synthesis for several in lab produced catalysts. Yields above 100 % indicates contamination. Nickel weight percentage is slightly above 15 wt.% for all catalysts. A balance was used for all ingredients to calculate yield and wt.%.

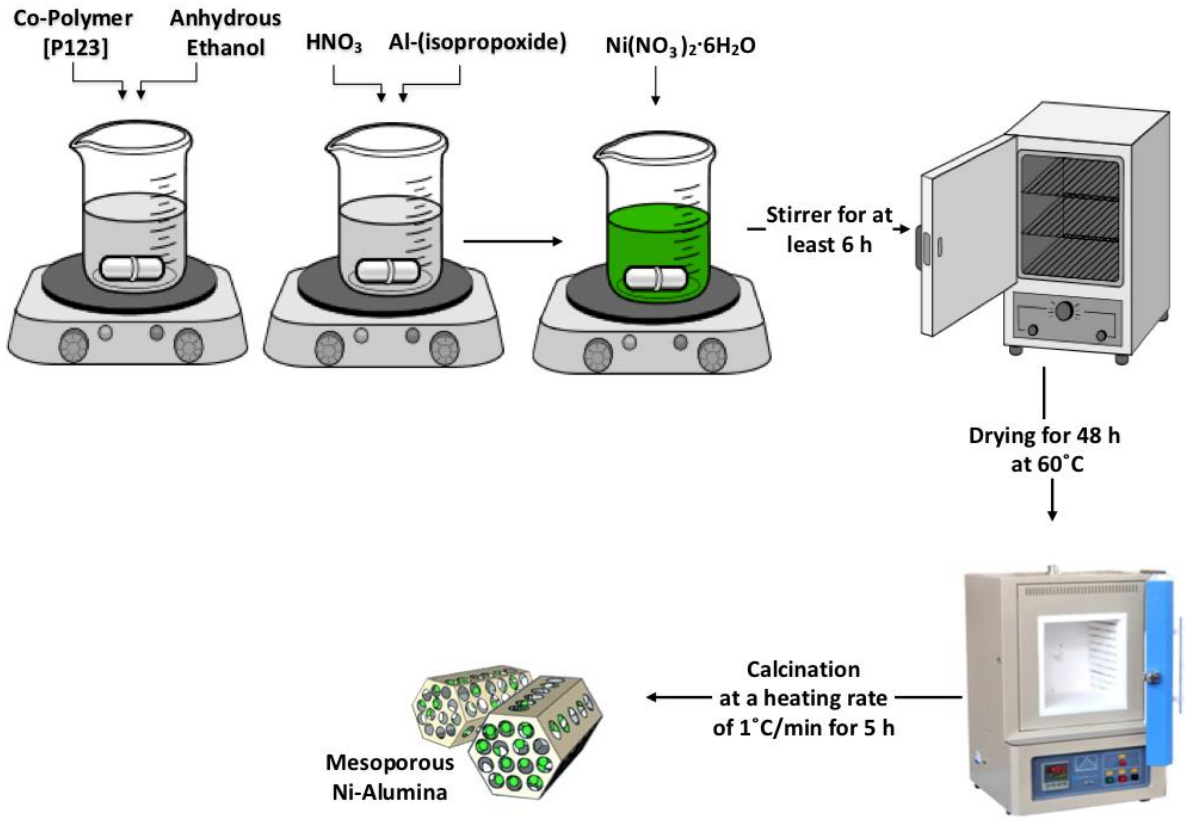

Figure 3-5 Graphical overview of catalyst synthesis, adapted from [22] where a Pluronic® P123 and anhydrous ethanol is mixed in a beaker followed by adding HNO_3 and Al-(isopropoxide). Nickel (II) nitrate hexahydrate is properly stirred before the catalyst is dried and calcinated at 500 °C.

3.2.2 Catalyst Coating

An appropriate technique to coat the plate with the catalyst is essential for an evenly distributed surface and thus a uniform catalyst mass distribution. The OMA catalyst was coated on the Fecralloy® support plate, which is an alloy of iron, chrome and aluminum. The plates were cut to 40 x 100 mm in order to fit in to the catalytic plate reactor. A schematic drawing of the plate is shown in Figure 3-6. The plates were either 0.5 or 1 mm thick. The different stiffness of a plate due to different thicknesses has advantages as well as disadvantages. On one hand a thicker plate is not that prone for deformation due to thermal stress, on the other hand it is easier to press a thinner plate properly to the bottom of the reactor to increase the heat transfer coefficient. It has to be noted that bending occurs in the range of up to 200 µm.

Prior to the coating a pre-treatment of the plate's surface was necessary to ensure a good interaction between the catalyst and the plate. Therefore, the Fecralloy® plate was cleaned with reverse osmosis (RO) water in an ultrasonic bath. After air drying a calcination process followed at 1000 °C for 36 hours using a heating rate of 10 °C · min^{-1}. This process converts aluminum oxide on the surface of the plate to γ-alumina, a whisker-like structure that bonds with binder and the support of the catalyst. This simplifies the application of the binder (e.g., Disperal® P2) to fix the catalyst on the plate and improves properties of the connection concerning mechanical stress. Unfortunately, it is possible that a binder covers the holes of a mesoporous support which leads to an inhibition of gases to block on the catalyst's surface. Until now it is just an assumption due to an experimental result and therefore a further investigation has to be done in the future. The coated area started at a length of 30 mm and ended at 85 mm. To coat the OMA catalyst evenly across the plate a technique called 'frame coating (FC)' was developed [35]. Therefore, a 3D – printed frame was attached with four clamps to the plate. The inner dimensions of the frame are approximately 1 mm bigger than the area to coat to avoid interface layer phenomena like adhesion to influence the coating. In addition, a not coated area on the side protects the coating against a destruction by a fixing bar. Simple Scotch® tape was used to cover and protect the uncoated area of the plate. A slurry containing the catalyst, isopropanol and RO-water was poured subsequently into the frame and the coating was air dried for a couple of hours. A schematic drawing of the frame coating technique is shown in Figure 3-7.

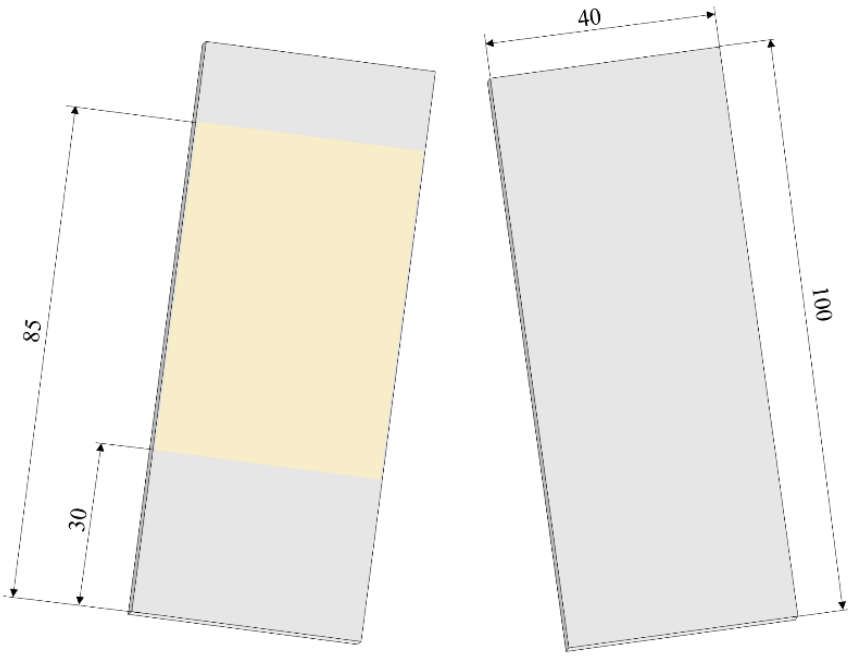

Figure 3-6 Front and backside of plate including dimensions. Plate dimensions were 100 x 40 mm with a coated area at the frontside (highlighted in ocher) with a dimension of 55 x 38 mm.

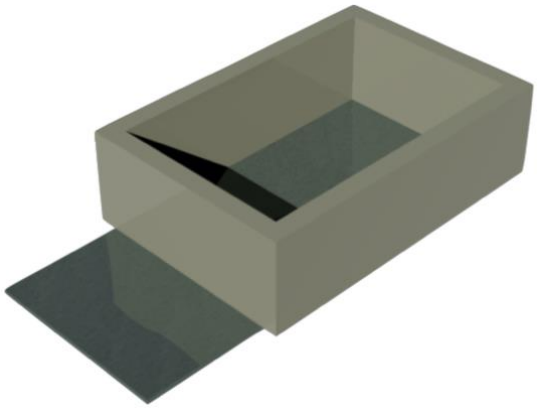

Figure 3-7 Plate with attached frame for frame coating (FC), adapted from [35]

A big advantage of this coating procedure compared to others like spin coating where centrifugal forces spread the catalyst over the plate or dip coating where a plate is dipped directly into the slurry is the amount of catalyst needed. In addition, the suspension leads to an equal distribution of the catalyst. Furthermore, it is possible to control the amount of catalyst on a plate by the amount of poured slurry. As mentioned before the suspension was a mixture of catalyst, isopropanol and RO water. The ratio of liquid to solid was approximately 20:1, the ratio of isopropanol to RO water 1:9. To prepare enough slurry to coat a plate around 0.125 g of catalyst were necessary. According to the ratios 2.25 ml of RO water as well as 0.25 ml of isopropanol was needed. Mixed together in a glass

vial, the suspension was stirred properly for 2 h at a speed of 1000 rpm. In the meantime, the frame coating was prepared by taping the plate, leveling the facility and fixing the frame. Immediately after the stirring of the slurry is stopped, approximately 2 ml of the slurry were taken with a pipette and the slurry was poured in the frame. To avoid a sedimentation of the catalyst in the pipette, this manual step had to be done fast. Recent studies in our laboratory try to slow sedimentation with the help of an acidic suspension. This results in an ionization of the particles and therefore an inhibition of the sedimentation process. Possible side effects have to be further investigated though. However, when the coating was dried the frame was removed carefully by taking off the clamps and the Scotch® tape was peeled off with tweezers. A subsequent calcination of the plate at 375 °C for 6 h with a constant a heating rate of 2 °C · min^{-1} finalized the coating process. An image (Figure 3-8) of a coated plate is shown below.

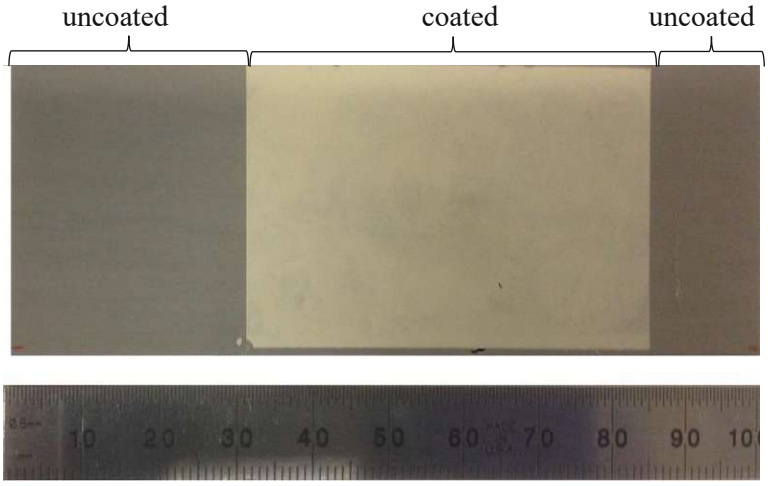

Figure 3-8 Plate after frame coating, catalyst: OMA-Ni15

3.2.3 Temperature Control

As mentioned before in chapter 3.1 LabVIEW™ was used to control and monitor the setup (heating, flow rates, pressure, capillary). Three K-type thermocouples (Omega KMTXL) were used to measure the temperature above the heating cartridges. The temperature was recorded by LabVIEW™ and compared to a set value using a negative feedback. The proportional-integral-derivate (PID) setting of the temperature controller for the current system were determined by using the Ziegler – Nichols (ZN) method [36].

The corresponding results are shown in Table 3-1 whereby the practical application of the method is described in the appendix. A subsequent test in the temperature range of 300 – 500 °C to check the

obtained PID parameters was performed successfully. In addition, it has to be noticed that LabVIEW™ also has an implemented auto tune setup which works with Ziegler – Nichols as well [37].

Table 3-1 Overview of PID parameters using Ziegler - Nichols method

Name	Nomenclature	ZN formula	Result
Ultimate proportional gain	K_{Pu}		13.5
Ultimate period	P_u		75 s
Proportional gain	K_P	$K_P = 0.6 \cdot K_{Pu}$	8.1
Integrative time	T_i	$T_i = 0.5 \cdot P_u$	37.5 s
Derivative time	T_d	$T_d = 0.25 \cdot T_i$	9.375 s

3.2.4 Empty Reactor Test

An empty reactor test was an essential step before performing catalyzed experiments by giving feedback about the uncatalyzed reaction. To be exact an uncoated plate was used inside the reactor at operating conditions to investigate whether an uncatalyzed reaction takes place or not. Additionally, this process was combined with an infrared camera calibration to explore the ability of different gases to absorb infrared radiation. For the empty reactor test a calcined 1 mm Fecralloy® plate was used at a temperature range of 300 to 450 °C. Following gas compositions were evaluated for this test: (1) Ar and H_2, (2) Ar and CO_2 and (3) a mixture of Ar, H_2 and CO_2. A total flowrate of 100 $ml_N \cdot min^{-1}$ was used for (1) and (2) at a ratio of 1:1 for the two gas mixtures respectively. The combination of all three substances was performed at a flowrate of 50 $ml_N \cdot min^{-1}$ for Ar as well as H_2 and 10 $ml_N \cdot min^{-1}$ for CO_2. However, according to the technical specifications of the FLIR SC2500 infrared camera a wavelength from 0.9 to 1.7 µm can be detected by the sensor [38]. The number of detected photons per pixel was accumulated over a specific time interval and was presented in form of a table with actual values or visualized as a picture. Figure 3-9 shows a graphical depiction of an uncoated plate at 350 °C with inserted flow straightener, thermocouple and capillary. The flow straightener was shaped like a honeycomb and the usage was tested during these preliminary experiments. On one hand, it would lead to a longer laminar flow regime and on the other hand the flow straightener would support the capillary which leads to a prevention of an unwanted bending. Unfortunately, the use of a flow straightener was combined with several new problems like an aggravated insertion of the thermocouple. Due to this it was not used for this thesis and a future research has to be done. A further problem is the correct usage of the thermocouple.

However, to guarantee a correct temperature measurement the tip of the thermocouple should touch the plate in a rectangular angle. As shown in Figure 3-9 this might not be the case in these preliminary experiments. Nevertheless, this imperfection is performed in all empty reactor tests and so a comparison of the results is still possible. The calibration curves for all gas compositions are presented in Figure 3-10. As the data shows there is no significant ability of different gas mixtures to absorb infrared radiation in this spectrum. It is commonly known that molecules like H_2 and Ar are not greenhouse gases but CO_2. The absorption spectrum of carbon dioxide shows no absorption of infrared light in the wavelength of 0.9 to 1.7 µm [39]. This also corresponds to the results of the preliminary test. In contrary, H_2O absorbs infrared light in this wavelength area and therefore a further investigation has to be done in the future. However, no significant increase of methane was detected by the mass spectrometer (MS).

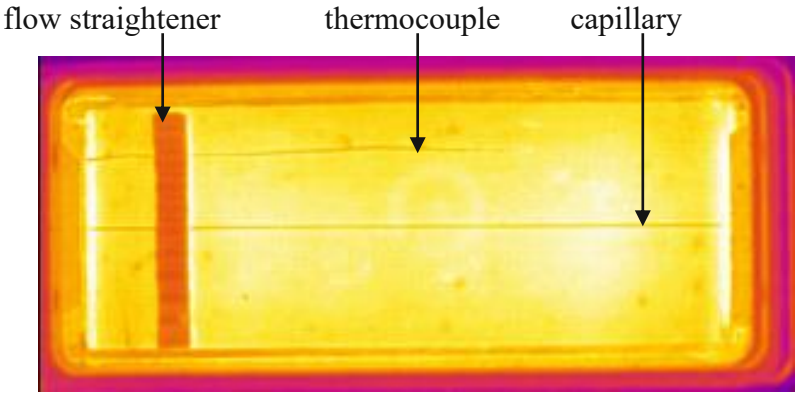

Figure 3-9 IR camera picture of empty plate reactor test with flow straightener, thermocouple and capillary

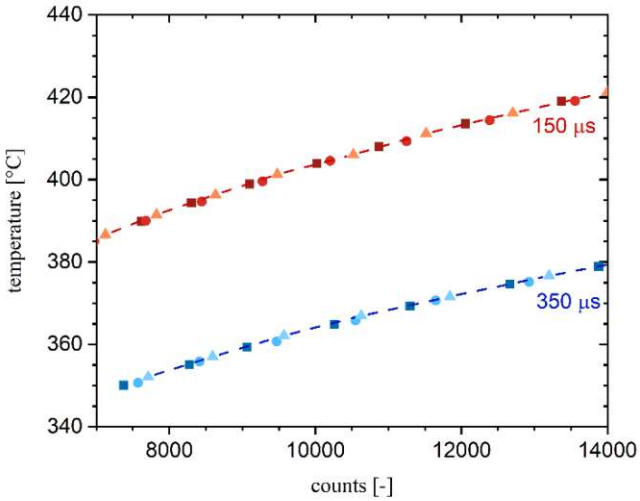

Figure 3-10 Influence of different gas mixtures (Ar with ▲ CO_2, ● H_2 or ■ H_2 / CO_2) on IR calibration through absorption of infrared light of Argon with different gas mixtures at an integration 150 µs and 350 µs

3.3 Experimental Procedure

The catalyst was synthesized and coated on a 1 mm Fecralloy® plate according to chapter 3.2.1 and 3.2.2. The coated plate was put into the reactor and pressed down with two fixing bars on each side. Right afterwards, the thermocouple was pulled through an opening of the reactor and bended down to ensure a contact in a rectangular angle. A visual as well as a data-based check was necessary to avoid an unwanted gap between the tip of the thermocouple and the surface of the plate. A difference of 1 °C between the surface and the three measured temperatures inside the body of the reactor was determined as acceptable. It has to be noticed that a cautious handling was necessary to prevent a destruction of the coating. Subsequently, the capillary was pushed slowly through a second reactor opening and moved carefully along the plate until it reaches the corresponding hole on the other end. Graphite gaskets combined with ferrules were used to ensure a sealing of the reactor. Then, the capillary was connected to the step motor as well as the mass spectrometer. For a proper measurement, it was essential that the hole of the capillary was facing down. After covering the reaction channel with quartz glass a second temperature check was completed. In addition, a leak test was performed by flushing 30 $ml_N \cdot min^{-1}$ of argon through the reactor and a detector called Snoop® (Swagelok®) was used to find possible leaks. If necessary, the ferrules were tightened firmer. This step had to be done at cold temperatures due to safety reasons even though gaskets expand with increasing temperature. However, after completing the leak test the second channel was installed, the reactor was closed with 16 screws and heated up slowly at a constant argon flow of 50 $ml_N \cdot min^{-1}$ until a temperature of 500 °C was reached.

3.3.1 Reduction of Catalyst

Nickel in the synthesized catalyst is in form of nickel oxide (NiO), which has no catalytic activity. Thus, prior to the acitvity measurements the NiO catalyst needed to be reduced to form zero-valent nickel. The reduction was carried under a diluted hydrogen atmosphere (50 vol% H_2 in Ar) at 575 °C. During the reduction, NiO reacts with H_2 to elemental Ni and H_2O.

The sampling capillary was moved to the end of the coating to measure the gas composition of the product gas via mass spectometry. H_2 and H_2O signals with their corresponding mass-to-charge ratio, m/z = 2 and m/z = 18, respectively, were monitored. During the reduction, the catalyst changed its color from beige to black. In general, this process took around seven to eight hours and was performed overnight. Thereby it was important that the pressure inside the reactor is higher than atmospheric pressure to ensure that no oxygen reaches the catalyst surface and passivates the catalyst. An image of a reduced catalyst is given in Figure 3-11.

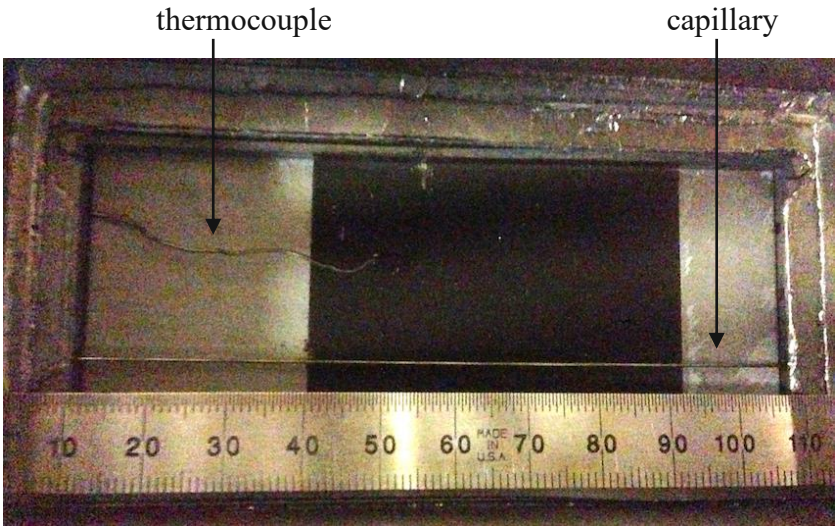

Figure 3-11 Reduced plate inside the reactor

3.3.2 IR Camera Calibration

As soon as the catalyst was fully reduced and turned black an IR camera calibration had to be done. The procedure always followed the same pathway: The plate's surface temperature was set to 290 °C. In the meantime, the program FLIR ResearchIR was started to monitor the infrared camera. For an accurate calibration, an area of 3 x 3 pixels was defined next to the tip of the thermocouple to ensure a proper correlation of temperature and counts. FLIR ResearchIR calculates the average counts in this defined area and provides the data to the user. As a subsequent step, the integration time of the camera was chosen. The integration time itself defines a time range in which the detected photons are accumulated. This can be compared with an exposure time of a regular camera. A longer exposure time is needed if there is less light (e.g., at night) and vice versa. The infrared camera is saturated at a value of approximately 15500 counts but the quality of the picture is better the closer this value is reached. Preliminary tests showed that a sufficient resolution was given between 8000 and 13000 counts. So, the approach for a proper IR calibration was to cover this specific range. After noting the surface temperature and the corresponding counts the reactor was heated up by 5 °C and another measurement was performed. This procedure was continued until the sensor was saturated. After this, the integration time was decreased and the process was repeated. In total, a temperature range from 290 to 460 °C had to be covered. The results of the IR calibration are presented below.

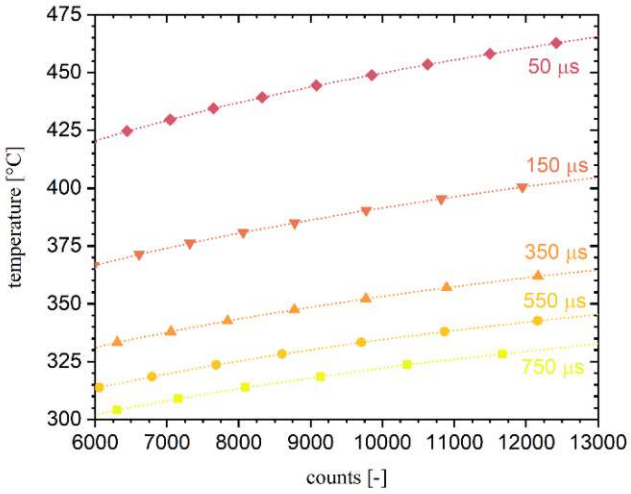

Figure 3-12 IR calibration curve FCOMA15-03 at different integration times

Preliminary tests showed that even a small difference in the amount of distributed catalyst led to different calibration results so the IR camera calibration had to be done for every plate. A 3-D model of the plate during an experimental test is shown in Figure 3-13. The thermocouple as well as the capillary are noticeable as furrows. The reason is the optical color change which results in a change of data point counts. However, at the area before the coating starts (length < 0 mm) the plate shows a higher count value than the region after the catalyst coating (length > 50 mm). This could indicate a leakage at the end of the plate which has to be considered in the kinetic study.

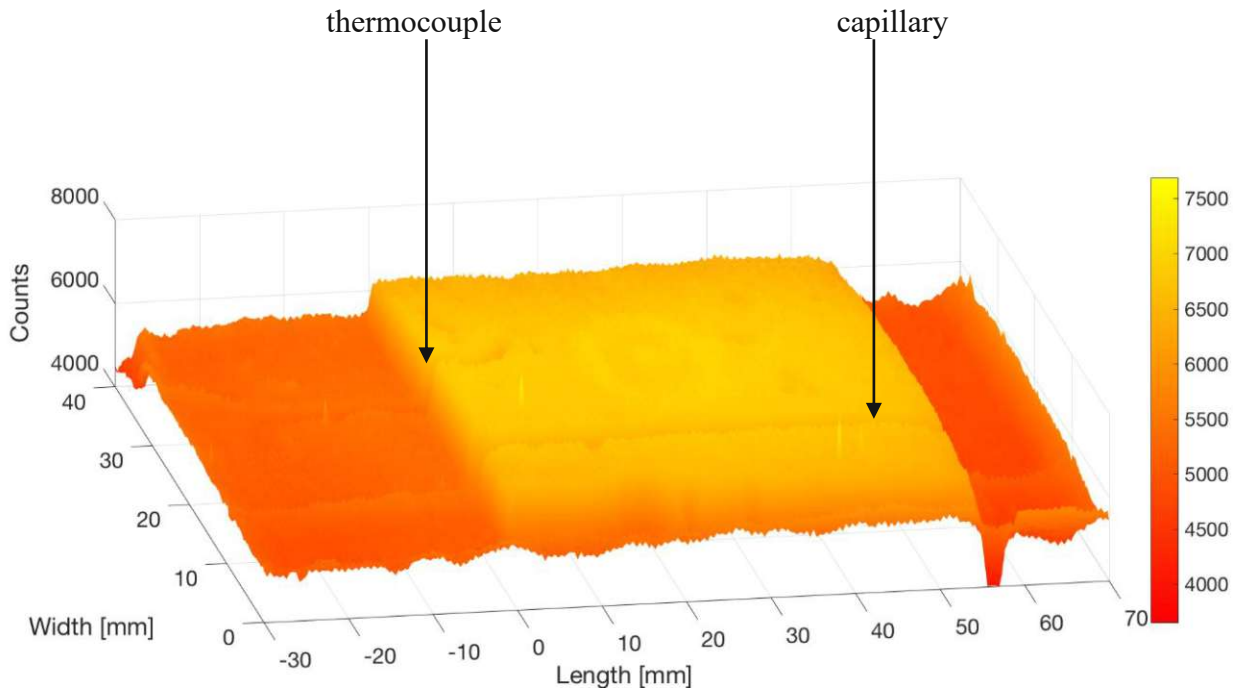

Figure 3-13: 3D-model of a plate during a pre-experimental test

3.3.3 CO_2 Methanation

For the methanation of carbon dioxide several experiments were performed to investigate the influence of different temperatures and flowrates. A constant pressure of 1 bar_g as well as an $Ar/H_2/CO_2$ ratio of 5:5:1 was kept as a constant for all experiments. In addition, just one plate, namely, FCOMA15-03 was used for the analysis in this thesis. Nonetheless, a temperature range from 300 to 450 °C was covered by steps of 50 °C, respectively. Flowrates varied from 55 to 220 $ml_N \cdot min^{-1}$ to investigate their influence on the methanation reaction. The highest flowrate was chosen on one hand in response to the mass flow controllers which had a maximal limit of 100 $ml_N \cdot min^{-1}$ and on the other hand due to the mass spectrometer where a H_2 fraction of 55 % and higher was not recommended.

However, in total 14 experiments were performed whereby two of them were repetitions of a base experiments to detect an eventual catalyst inactivity. An overview of the settings is shown in Table 3-2. It has to be mentioned that the respective temperatures are surface temperatures of the plate, measured by the thermocouple inside the reaction channel. Ex 1a is chosen as base experiment and Ex 1b and Ex 1c were the corresponding repetitions. The starting position of the capillary was set 15 mm before the coating, the corresponding final position was 5 mm after the coating. A high resolution and hence a small step size of 1 mm was programmed at the beginning and at the end of the catalytic part, in the middle of the coating a step was between 2 and 5 mm long. The gas composition was measured at every position for 30 seconds, respectively whereby a loop of the used MS took around eight seconds. This resulted in at least three gas composition measurements at every position. For future kinetic experiments, it is recommended to measure more than three gas compositions at every position. However, the temperature was measured before and during the reaction by the infrared camera. Before a reaction only Ar and H_2 were flushed through the reactor, but as shown in chapter 3.2.4 this leads to no significant change of the infrared measurement compared to a gas mixture with CO_2. In addition, due to steady state conditions a single data file during the methanation was defined as sufficient for a proper temperature measurement.

Table 3-2 Overview of experimental settings

Experiment	Plate	T_S [°C]	Flowrate [$ml_N \cdot min^{-1}$]
Ex 1a	FCOMA15-03	350	110
Ex 2	FCOMA15-03	350	55
Ex 3	FCOMA15-03	350	220
Ex 4	FCOMA15-03	300	110
Ex 5	FCOMA15-03	300	55
Ex 6	FCOMA15-03	300	220
Ex 7 | 1b	FCOMA15-03	350	110
Ex 8	FCOMA15-03	400	110
Ex 9	FCOMA15-03	400	55
Ex 10	FCOMA15-03	400	220
Ex 11	FCOMA15-03	450	110
Ex 12	FCOMA15-03	450	55
Ex 13	FCOMA15-03	450	220
Ex 14 | 1c	FCOMA15-03	350	110

T_S Surface temperature of the plate

Each experiment was started by flushing Ar and H_2 through the reactor at their respective flowrates. The pressure was adjusted to approximately 0.8 bar_g by opening or closing the hand valve. As soon as all CO_2 from previous experiments were removed from the reactor the step motor was set to position ‘zero’. Thus, the hole of the capillary was set to 15 mm before the coating. Stepwise CO_2 was induced into the reactor until the required flowrate was reached. Contemporaneous the pressure was regulated to a final value of 1 bar_g. After reaching steady state conditions the step motor was started. A good indicator of a steady state reaction was a detection of constant gas compositions by the MS. However, in total 40 different positions were measured during an experiment. It was necessary to overview a correct movement of the capillary constantly. After approximately 20 minutes the last position was reached, and the corresponding gas composition was measured and thus, the experiment was finished. In case of a failure the experiment was stopped and repeated from the beginning.

3.4 Post Processing Analysis

After completing all experiments, the reactor was cooled down and the screws were opened slightly. This small leakage provided oxygen to reach the catalyst's surface and hence to passivate the catalyst. This reaction is highly exothermic ($\Delta H_R^0 = -669.82\ \mathrm{kJ \cdot mol^{-1}}$) and therefore just a small amount of oxygen was allowed to enter the reactor. The passivation of the catalyst was usually performed overnight. Subsequently, the reactor was opened completely and the capillary as well as the thermocouple were removed carefully. A touching of the coating still had to be avoided for a proper post processing analysis. After removing the fixing bars the plate was taken out of the reactor and stored in a box.

3.4.1 Profilometry

To gain information of the mass distribution of the catalyst a profilometry measurement had to be done. Therefore, a preparation of the previously used plate was necessary. To do this several reference points on the plate were marked and in addition the coating was cut vertically with a scalpel every centimeter as shown in Figure 3-14. This was necessary to correct unavoidable curvatures of the plate. A detailed explanation of the correction mechanism is described by Jose Hernandez Lalinde et al [32]. Additionally, destructions of the coating by a careless handling of the capillary and due to the fixing bars are presented in Figure 3-14. The white dashed lines indicate the five regions where the height measurement is evaluated.

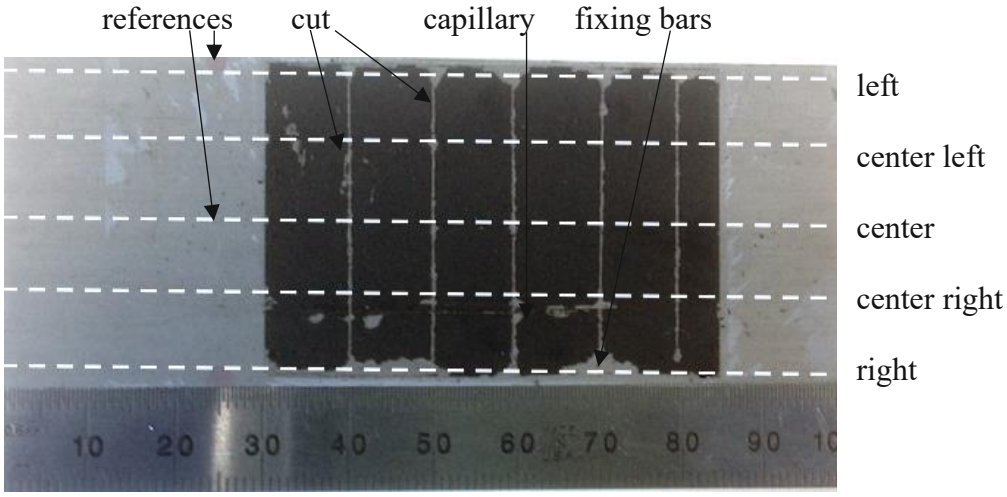

Figure 3-14 FCOMA15-01 prepared for profilometry and destructions due to fixing bars and the capillary

The profilometry was performed with an instrument called DektakXT stylus profiler. In general, a needle with a diameter of 12.5 µm travels along the plate and measures the corresponding vertical profile. The stylus force was set to the weakest possible value of 1 mg. This weak force avoids a further destruction of the coating but it could lead to an error due to an easy drift off. However, the stylus was adjusted to the reference point in the middle of the plate and this spot was defined as a starting value. The height profile along the center line of the plate was measured for a distance of 65 mm. Thereby, the specific resolution was 2000 points · mm^{-1}. After finishing a loop, the stylus was either set 1 cm to the left (center left line) or the right (center right line) and the measurement was repeated. The indicated lines 'left' and 'right' were 1.5 cm away from the center spot, respectively. The profilometry was performed line by line until every measurement was taken. The resulting raw data was used for further analysis.

3.4.2 Catalytic Surface Area

Physisorption measurements are commonly used to determine surface areas and pore size distributions of porous solids [40]. The investigation of these parameters was done by Nitrogen (N_2) adsorption/desorption using Autosorb IQ (Quantachrome Instruments) whereby the theoretical principle behind this analysis is the Brunauer-Emmett-Teller (BET) method. This theory is an extension of the Langmuir adsorption model but it is based on a multilayer instead of a monolayer physical adsorption [41]. The theoretical fundations of a BET analysis rests upon various assumptions: (1) a homogenous particle surface, (2) only 'vertical' interactions between molecules within the adsorbed layers are taken into account and (3) at saturated vapor pressure the number of adsorbed layers is infinite [41].

However, in 1985 the International Union of Pure and Applied Chemistry (IUPAC) declared six types of adsorbtion isotherms, see Figure 3-15 (A) Type I to VI. Thommes et al. proposed 30 years later an updated classification with eight characteristic types in which Type I and IV are divided into part (a) and (b), respectively [40]. Mesoporous adsorbents are characterized by Type IV isotherms, whereby Type IV(b) characterizes mesoporous of smaller widths. The hysteresis in contrary which is shown in Type IV(a) only occurs when the width of a pore exceeds a specific critical value depending on the adsorbate and the temperature. For N_2 this critical pore width is approximately 4 nm [42]. As additional information, different types of hysteresis loops are given in Figure 3-15 (B), whereby Type H1 represents a narrow range of uniform mesopores and H2 structures with network effects (e.g., pore blocking) [40].

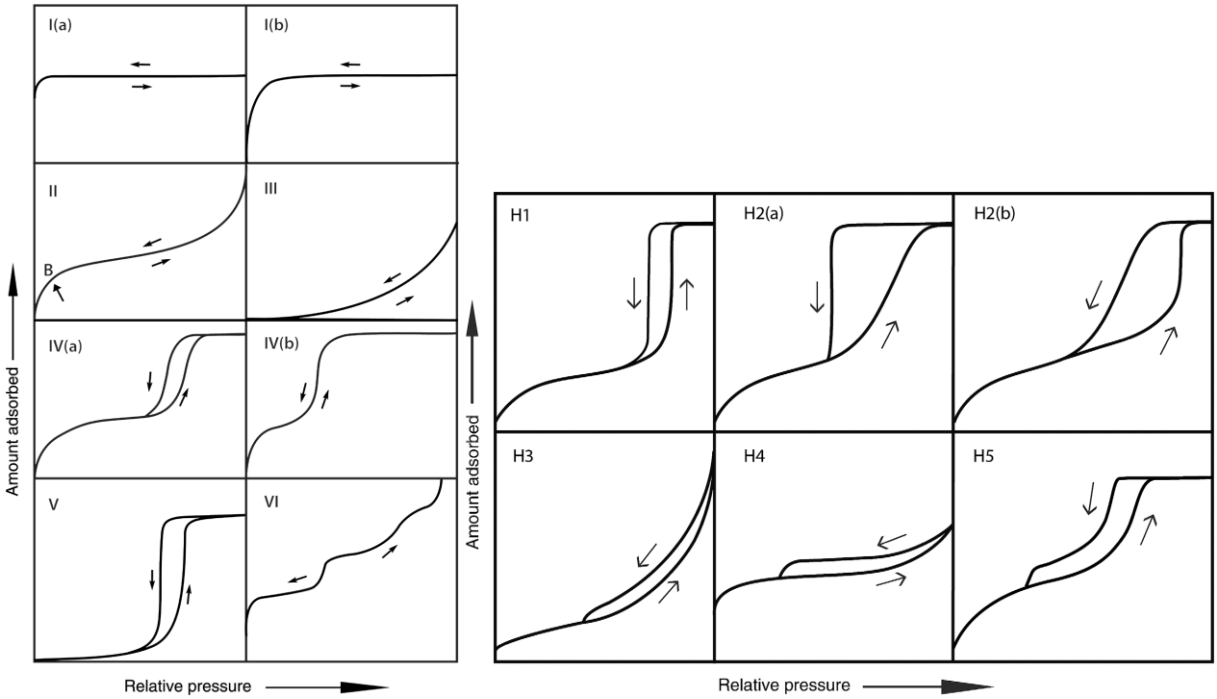

Figure 3-15 Classification of adsorbtion isotherms (A) and hysterisis loops (B) [40]

The BET specific surface area S_{BET} of an adsorbent can be calculated according to equation 3-1.

$$S_{BET} = \frac{x_m}{22414} \cdot N \cdot A_m \times 10^{-20} \qquad \textbf{3-1}$$

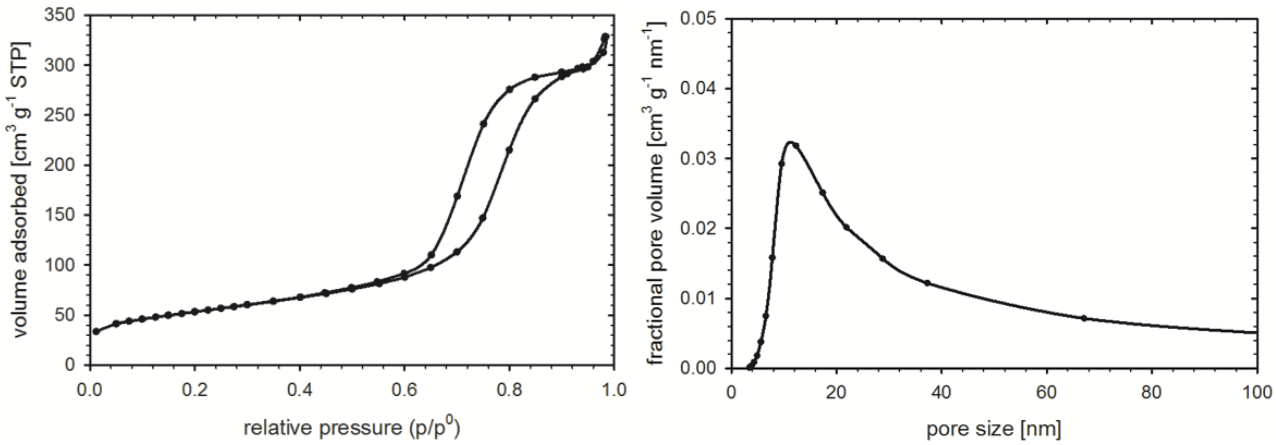

Figure 3-16 Physisorption isotherm (A), pore size distribution (B)

The slight upturn in Figure 3-16 (A) starting at a relative pressure of 0.9 is attributed to capillary condensation effects in macropores [41]. This also corresponds to the results of the pore size distribution (B) where coarse pores (pore size higher than 50 nm) occur.

3.4.3 Catalyst Morphology

A morphology analysis of the catalyst particles was performed using Phenom Pro scanning electrone microscope (SEM) with a back-scattered electron (BSE) detector [43]. Generally, SEMs are scanning the surface of a sample in a vacuum chamber with an electrone beam which interacts with surface or near-surface atoms resulting in signals of secondary electrons, back-scattered electrons, X-rays etc., whereby the detection of BSEs is one of the most common [44]. Prior to the analysis a pin stub was covered with a double-sided adhesive tape. Then, catalyst powder with a particle size of 20 – 45 µm was distributed carefully on the tape and any loose particles were removed using an air gun. These two steps were necessary to avoid a contamination of the vacuum chamber. Subsequently, the pin stub was pluged into the sample holder and placed into the SEM. The resulting images are presented in Figure 3-17. It is noticeable that the shape of the catalyst is not spherical and as far as it is possible to determine particle sizes in a two dimensional image it is strikable that there are many particles which are smaller or bigger than the expected 20 – 45 µm. A possible reason for longer cylindrical shaped particles to enter this mesh size is their smaller cross section. In addition is is not completely excluded that dust particles are contaminating the specimen. However, according to this result the crushing and sieving process is still worth of improvement.

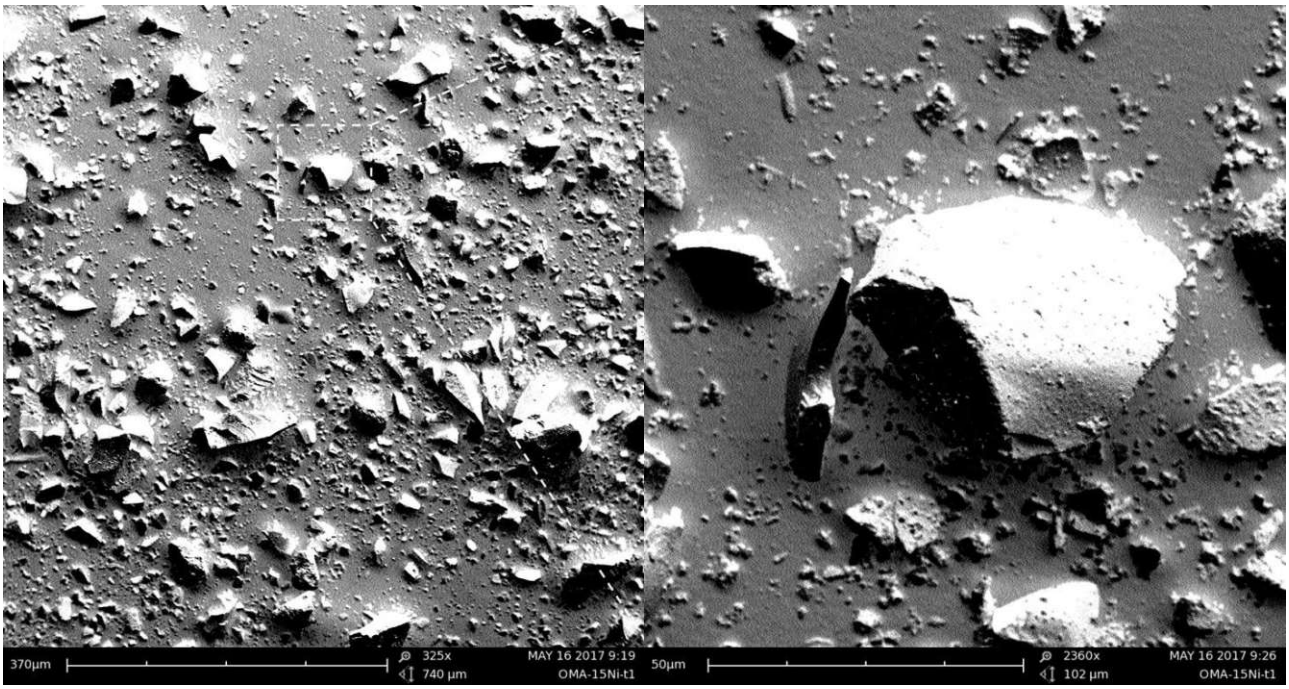

Figure 3-17 SEM image of catalyst particles

Chapter 4

4 Results and Discussion

4.1 Experimental results

In the following chapter the experimental results for different temperatures and flow rates are shown. As base experiment, experiment no.1 in Table 3-2 is used, and all changes in operating conditions are presented in respect to this reference experiment. In Section 4.1.1 the influence of a temperature change is investigated whereas temperatures reach from 300 °C to 450 °C, chapter 4.1.2 shows how flow rates from 55 to 220 $ml_N \cdot min^{-1}$ are affecting the methanation process and section 4.1.3 gives an overview about an eventual catalyst inactivity during these experiments. All experiments were done at a constant pressure of 1.0 bar_g.

4.1.1 Effect of different operating temperatures

For the reference experiment (plotted in Figure 4-1) the operating temperature as well as the flow rate were fixed at 350 °C and 110 $ml_N \cdot min^{-1}$ at a constant $Ar/H_2/CO_2$ ratio of 5:5:1. Figure 4-2 shows the results for 300 °C, 400 °C and 450 °C, respectively. The coated area of the reactor starts at a length of 0.0 mm and reaches until 55.0 mm, before and after the uncoated part of the plate is shown. In total 40 measurement points were taken for each experiment, whereas 30 of them are on a catalyst coated area. At the beginning of the plate from - 15 to 0 mm the values of CO, CO_2, CH_4 and H_2O remains the same. In contrary H_2 is slightly decreasing from 44.8 to 43.2 vol. %. This is a change in

flow rate from 49.1 to 46.4 $ml_N \cdot min^{-1}$. As temperature rises this effect increases. Possibility one (1) is a measurement error at the hydrogen peak. Second (2), a contamination with oxygen could convert hydrogen to H_2O but free oxygen also leads to a catalyst passivation. Third (3), a small leakage in the reactor which is more sensitive for hydrogen due to its small size and fourth (4), axial dispersion in combination with the sample size of the capillary is shifting the measurement results. At constant flowrates, reason (1) would affect all temperatures equally. For possibility (2), no significant catalyst deactivation is shown (see chapter 4.1.3). Case (3) does favour higher temperatures but at all flow rates would be equally affected. So reason (4) is a likely variance, as shown by Hernandez Lalinde [45].

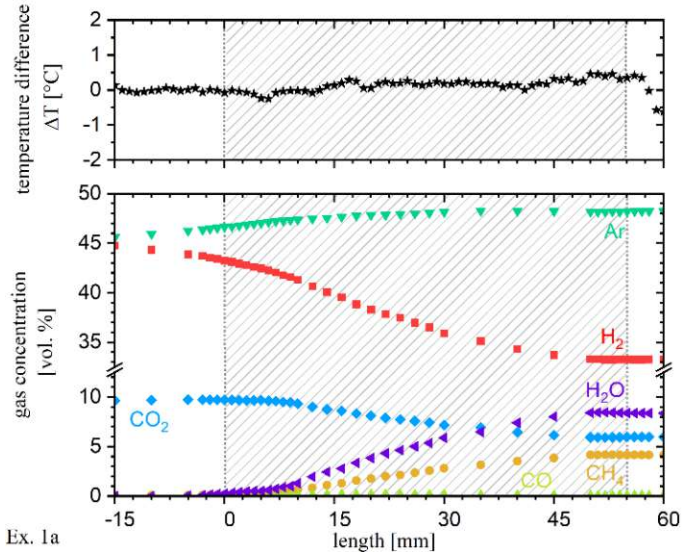

Figure 4-1 Change in temperature (above) and gas composition (below) for (▼) Ar, (■) H_2, (◀) H_2O, (◆) CO_2, (●) CH_4, and (▲) CO along the catalytic plate at operating temperature of 350 °C , flow rate of 110 $ml_N \cdot min^{-1}$ pressure of 1.0 bar_g (experiment 1a).

At the beginning of the coated area the concentration of CH_4 starts to rise continiously until a maximum of 4.2 vol. % is reached at a length of 50 mm until the end. At the last 5 mm of the coating no increase of methane concentration is visible. This effect occurs in all experiments, thus an inactivity of the catalyst in this area is possible. The concentration of CO is almost neglectable for all temperatures as it is not increasing significantly. Still, there is a small peak of 0.2 vol. % in CO concentration at a length of 20 mm and decreases to almost 0 vol. % until the end. Thus, the water gas shift reaction ($H_2 + CO_2 \leftrightarrow CO + H_2O$) partially takes place as an intermediate reaction. However, the H_2O concentration was not possible to measure with the MS so the values which are shown in all figures in chapter 4 are calculated stochiometric according to Rx-1 and Rx-2 in

chapter 2.1. Another possibility of calculating H_2O fractions is by calculating hydrogen or oxygen-balances. A deeper look is shown in chapter 4.1.4. The temperature graph illustrated in Figure 4-1 shows the change in temperature before and during the reaction ($T_{with\_CO2} - T_{w/o\_CO2}$). Before the coated area no temperature deviation is noticeable. Also for the first part of the coated region until a length of 15 mm the temperature does not increase significantly. The small decrease of 0.2 °C at 5 mm could be a measurement or data acqusation error. At the center of the coating up until the end the temperature deviation is slightly positive from 0.2 to 0.4 °C. In expermiment 1 a conversion of $X_{CO2} = 41.3$ % is reached for carbon dioxide, with a methane yield Y_{CH4} of 40.7 % and thus a selectivity S_{CH4} of 98.4 %.

For a temperature of 300 °C (see Figure 4-2, Ex. 4) the conversion X_{CO2} reaches 14 %. This leads to a methane production of roughly 1.3 vol. % and thus a yield Y_{CH4} of 13.2 % and a selectivity S_{CH4} of 97.6%. Overall the reaction slows down at lower temperatures. The deviation in temperature profile is more significant for this operating conditions. Along the catalyst surface a ΔT_{max} of 0.8 °C is reached at the end of the coated area. The volume concentration of H_2 decreases from 45 to 41.7 vol. %, the concentration of CO_2 declines from 9.6 vol. % at the beginning to 8.4 vol. % at the end. Again, a slight amount of CO is visible.

As temperature increases (Figure 4-2, Ex. 8 and Ex. 11, respectively) also the methane conversion increases up to gas concentration of 7.8 vol. % for a temperature of 400 °C and 8.8 vol. % for 450 °C. This time, the effect of an H_2 decline before the catalytic area is even more significant. Furthermore, the conversion of CH_4 stops again at a length of 50 mm. The conversion of CO_2 X_{CO2} increases to 69.1 and 76.6 % for 400 and 450 °C with a methane yield Y_{CH4} of 71.6 and 79.4 %, respectively. For both experiments the selectivity exceeds a value of 1 with roughly 103.7 %. Even though exothermic reactions favour lower temperatures the intermediate step of a CO_2 methanation requires a higher temperature level and thus, the conversion of CH_4 increases as temperature rises.

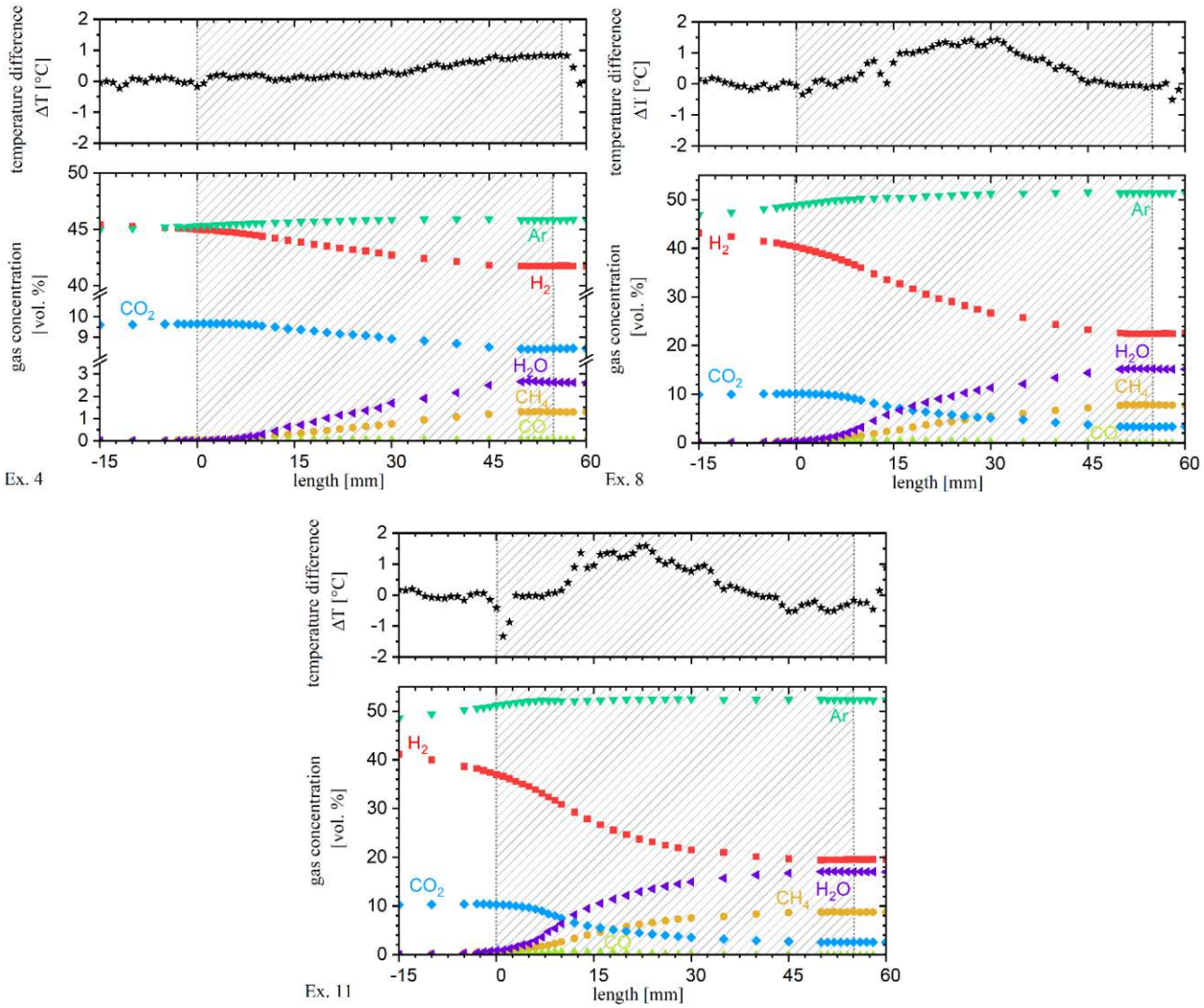

Figure 4-2 Effect of different operating temperature on gas composition at 300 °C (Ex. 4), 400 °C (Ex. 8) and 450 °C (Ex.11) and constant flow rates of 110 $ml_N \cdot min^{-1}$. Temperature difference along plate is shown above, concentration of (▼) Ar, (■) H_2, (◀) H_2O, (◆) CO_2, (●) CH_4, and (▲) CO is plotted below.

4.1.2 Effect of different flow rates

Analogous to chapter 4.1.1 the reference experiment was done at a temperature of 350 °C and a flowrate of 110 $ml_N \cdot min^{-1}$ with an $Ar/H_2/CO_2$ ratio of 5:5:1. This time only the flowrate were changed from 55 to 220 $ml_N \cdot min^{-1}$, respectively, and the results are plotted in Figure 4-3 Ex. 2 and Ex. 3, respectively.

A reduced flowrate of 55 $ml_N \cdot min^{-1}$ results in a steeper incline of CH_4 gas concentration along the reactor resulting in a total value of 6.2 vol. % and thus a yield Y_{CH4} of 59.6 %. Analogous, the conversion of CO_2 increases to 55.6 % compared to 41.3 % for 110 $ml_N \cdot min^{-1}$ as shown in Ex. 1. The selectivity S_{CH4} reaches again a value above one with 107.1 % though. The concentrations of H_2 and CO_2 decline from 40.0 to 27.4 and 10.1 to 4.6 vol. %. The temperature difference before and during the reaction is around ± 0.2 °C with a drop in temperature at a length of 45 mm to -0.4 °C.

Ex. 3 in comparison showed a steep incline in temperature difference along the coated area with an upper level of 0.8 °C. The gas concentration of H_2 and CO_2 reached a final value of 38.0 and 7.1 vol. %, respectively. At a flowrate of 220 $ml_N \cdot min^{-1}$ the hydrogen gas concentration is measured at 45.7 vol. % compared to 40.0 at a flowrate of 55 $ml_N \cdot min^{-1}$. In this experimental run the results for X_{CO2}, Y_{CH4} and S_{CH4} targeting values of 28.0, 23.8 and 85.2 %, respectively. The concentration of CO reaches up to 0.18 vol. % with no significant drop at the end of the plate as shown in the reference Ex. 1.

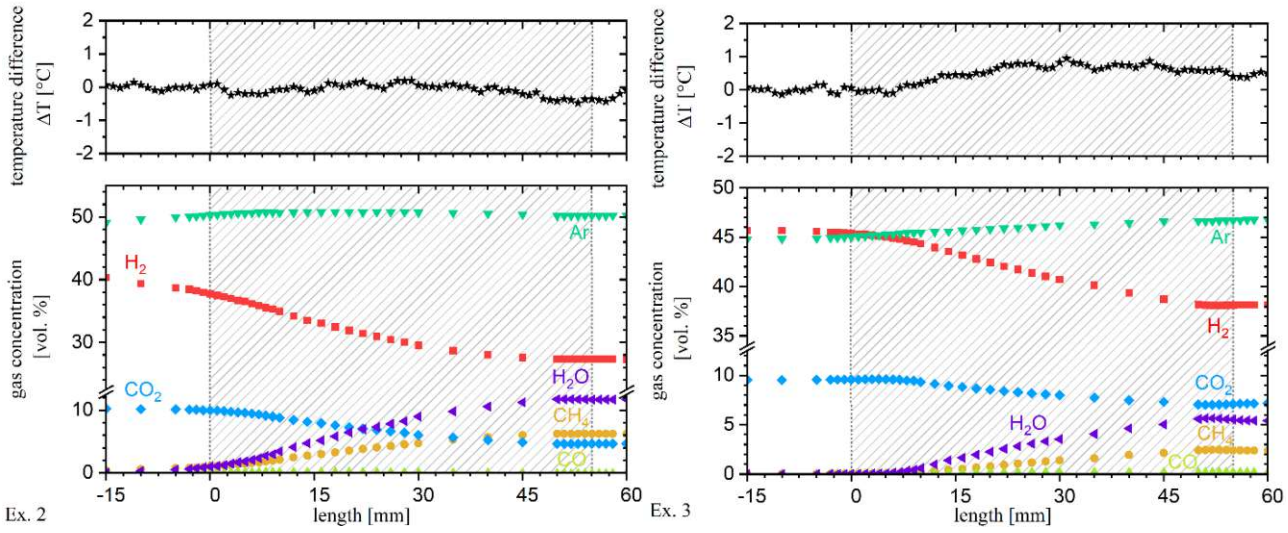

Figure 4-3 Effect of different feed flow rates of 55 and 220 $ml_N \cdot min^{-1}$. Operating temperature and pressure is constant at 350 °C and 1.0 bar_g. Change in concentration of (▼) Ar, (■) H_2, (◀) H_2O, (◆) CO_2, (●) CH_4, and (▲) CO is shown below.

4.1.3 Catalyst deactivation

To determine catalyst deactivation and to show repeatability of results the base experiment was performed between the temperature change from 300 to 400 °C (Ex. 1b) and at the end of all experiments (Ex. 1c). In Figure 4-4 the results are illustrated. For Ex. 1b no catalyst deviation is visible resulting in a difference of gas concentrations in a range of 0.1, 0.03 and 0.04 vol. % for H_2, CH_4 and CO_2, respectively. For Ex. 1c a slight drop of catalyst activity is noticeable resulting in a drop of methane concentration from 4.17 to 3.93 vol. %. The high operating temperatures of 450 °C could be a responsible for this. However, in general the results are reproducible.

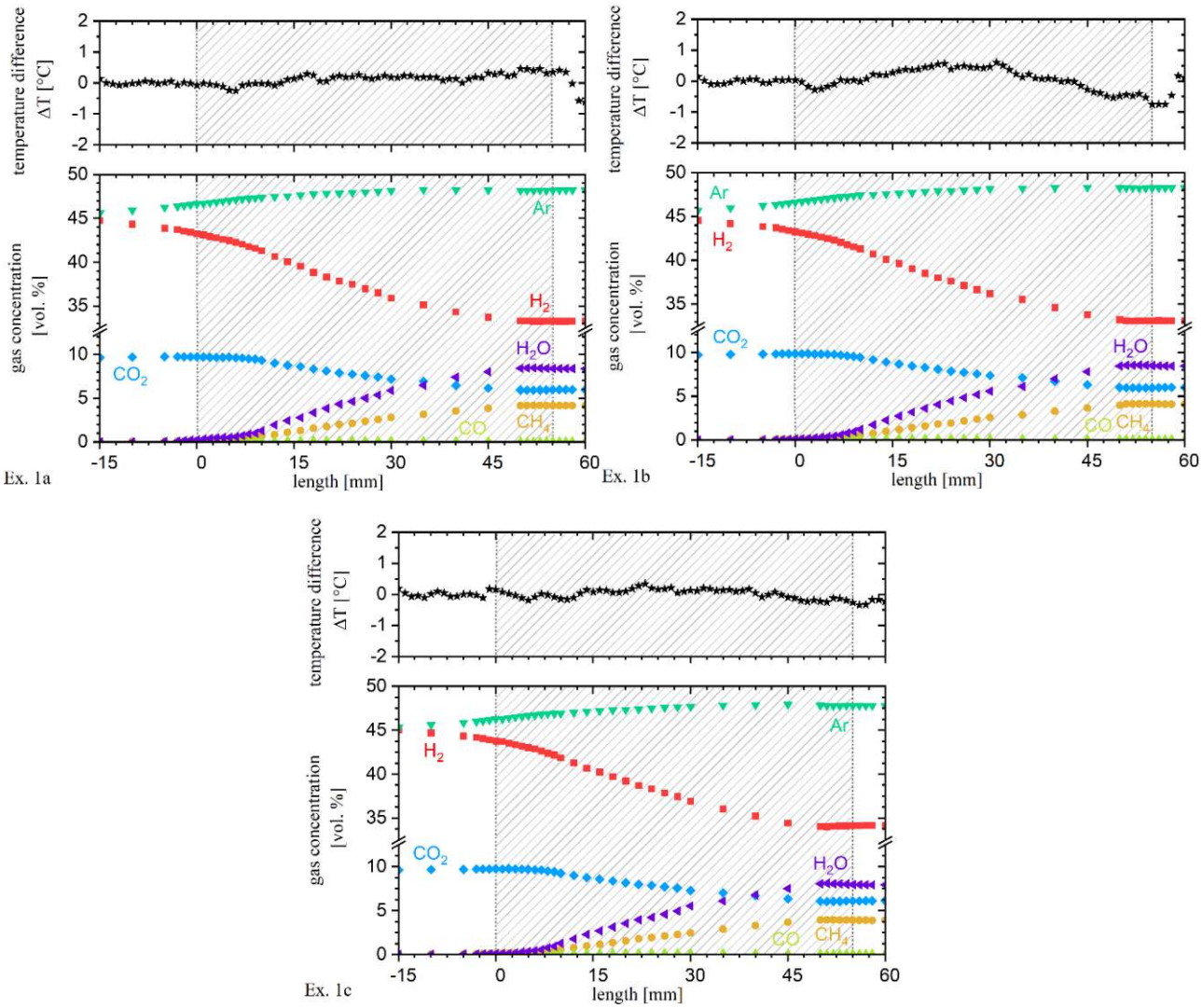

Figure 4-4 Reproducability and catalyst deactivation at operating temperatures of 350 °C, pressure of 1 bar_g and a feed flow rate of 110 $ml_N \cdot min^{-1}$ (Ex. 1a to 1c). (▼) Ar, (■) H_2, (◀) H_2O, (◆) CO_2, (●) CH_4, and (▲) CO compositions are shown below, change in temperature along plate is shown above.

4.1.4 Balance Calculations

To calculate the H_2O fraction several options are possible: (1) stoichiometric calculation according to Rx-1 $4\,H_2 + CO_2 \leftrightarrow CH_4 + 2\,H_2O$ with CH_4, (2) calculating with the drop of H_2 in Rx-1, (3) stoichiometric to Rx-1 and Rx-2 with CO_2 and CO, respectively, (4) with a general H balance and (5) with an O balance. The calculation with hydrogen is not recommended due to a volume concentration drop before the catalytic area. Thus, there would be a peak of H_2O before any reaction takes place. Thus, option 2 and 4 were not used. A oxygen balance calculation leads to flow rates above the initial values of 55, 110 and 220 $ml_N \cdot min^{-1}$, respectively. Whereby, the stoichiometric balance according to Rx-1 leads to a volume contraction. Thus, option 5 is not possible. A methane balanced H_2O calculation compared to the stoichiometric calculation with CO_2 and CO shows similar values. However, option (3) also includes the reversed WGS shift reaction ($H_2 + CO_2 \leftrightarrow CO + H_2O$).

The molar balance for carbon and oxygen are for all experiments in a range within ± 4 %, respectively. For small flow rates of 55 $ml_N \cdot min^{-1}$ the molar balance of hydrogen exceeds this area with deviations up to 10 %.

4.2 Catalyst mass distribution

To determine catalyst mass distribution a profilometry measurement as described in chapter 3.4.1 was performed as a post processing step. For the catalyst used in this thesis (FCOMA15-03) this measurement was not feasible due to a damaging of the plate while removing it from the reactor. Therefore, data acquistion of previous coating plates (FCOMA15-01 and FCOMA15-02, respectively) were analyzed to determine a mass distribution for FCOMA15-03. In Figure 4-5 a pathway of the profilometry measurements is shown in dashed lines whereby the white lines roughly approximate the actual measurement path. To reduce a plate bending influence on the measurement results the catalyst was removed carefully with a scalpel every 10 mm. In a post processing step the height difference at those cleaned areas was considered first, as shown in a systematic drawing in Figure 4-6. The change in height Δh where the catalyst was removed was set to the same level at both ends and all values inbetween were reduced by its correspondig triangular height. The final results of the fitting is shown in Figure 4-5 on the right side. In genereal the height of the catalyst varies between 40 and 85 µm. With a used particle size of 20 – 45 µm it is assumed that the catalytic layer is two to three particles high.

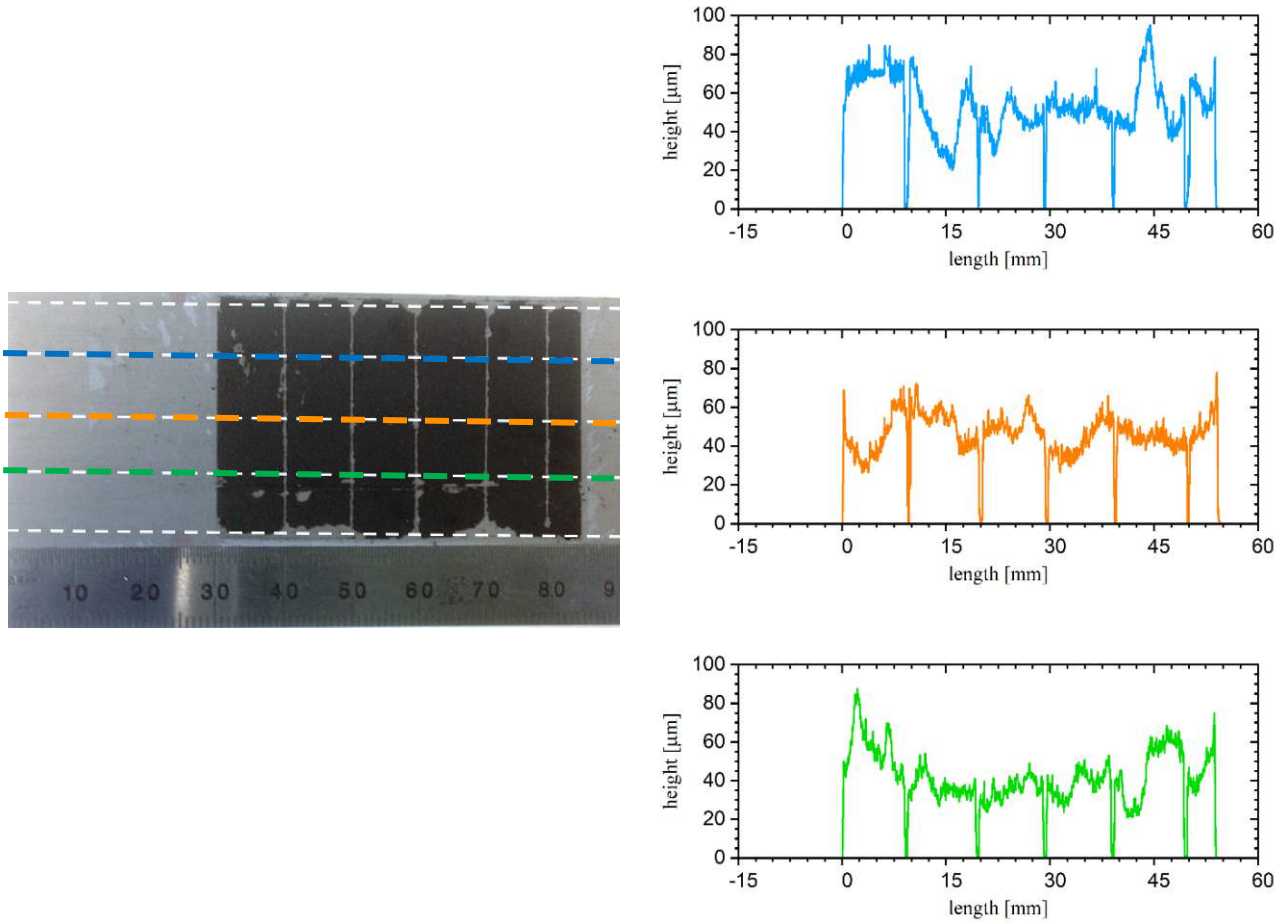

Figure 4-5: FCOMA15-02 plate with measured pathways (left) and already corrected profilometry results (right)

To calculate the final mass distribution all values within a distance of 1 mm are averaged and a fraction of the total catalyst mass was calculated. The final results for the 'center' position are shown in Figure 4-7 for FCOMA15-01 and FCOMA15-02. In these experiments the total catalyst mass for FCOMA15-01 and -02 were 142.5 mg and 79.2 mg, respectively. Plate A shows an evenly distributed catalyst with a mass of around 3.0 mg_{cat} mm^{-1} with small sinks at 10 mm and 25 mm. Plate B starts with a catalyst mass of 2.0 mg_{cat} mm^{-1} and drops constantly to a value of around 1.5 mg_{cat} mm^{-1}. Both phenoma are results of the coating process. Droplets while coating the plate could lead to sinks in the catalyst distribution and an unequal amount of slurry at both ends shows results as seen on plate B. A vibrating base could lead to an improvement of the frame coating procedure and an evenlier distributed catalyst. However, the results for both plates show that an assumption of an evenly distributed catalyst for FCOMA15-03 is given. Thus, a total mass of 130.2 mg_{cat} results in a distribution of 2.4 mg_{cat} mm^{-1}.

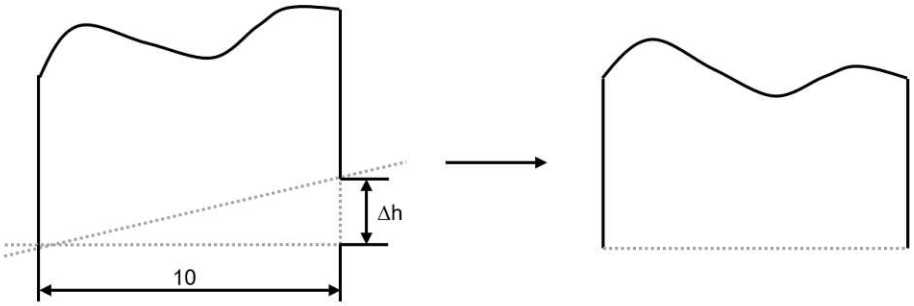

Figure 4-6 Schematic drawing of plate curvature correction

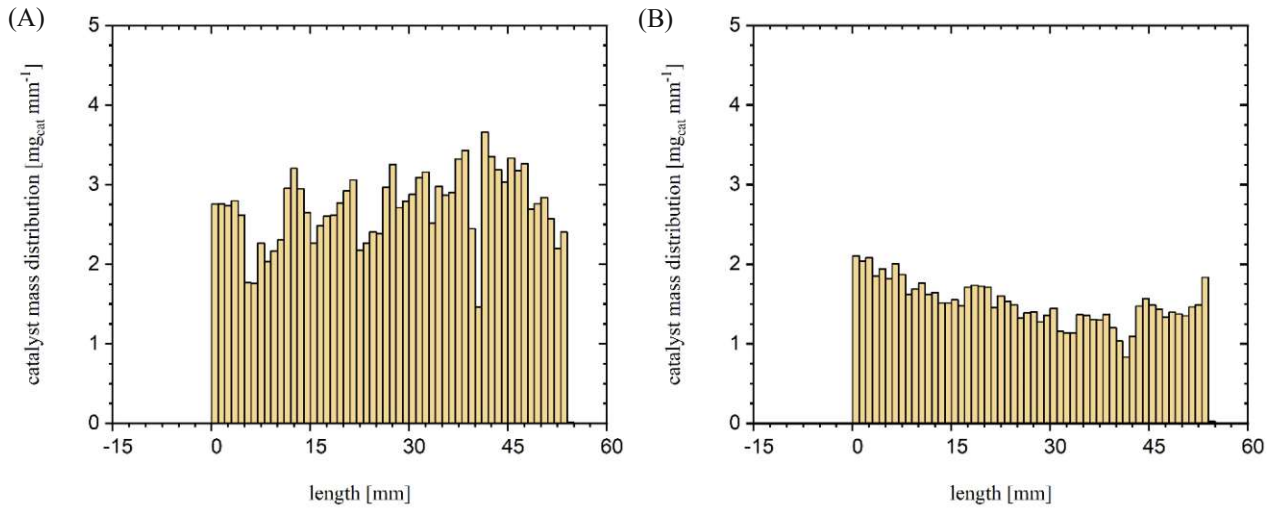

Figure 4-7 Catalyst mass distribution for FCOMA15-01 (A) and FCOMA15-02 (B)

4.3 Kinetic studies

4.3.1 Development of rate equations

The rate equations for the kinetic studies are developed according to the Langmuir-Hinshelwood mechanism based on an assumption of the rate-determining step (RDS) as stated by Kopyscinski and Koschany for the methanation of CO and CO_2, respectively [17], [46]. It is assumed as well, that all other reactions are either in equilibrium or irreversible. The Langmuir-Hinshelwood approach requires information about adsorbed reactants and products and their effects on reaction kinetics. Thus, the final rate equation contains an adsorption term and the specific partial pressure which represents the driving force of the reaction (see 4-1).

$$r = \frac{(kinetic\ term) \cdot (driving\ force)}{adsorption\ term} \qquad \textbf{4-1}$$

For the adsorption term, it is assumed that the surface coverages of reactants and products are in equilibrium. Thus, the rate of adsorption and desorption is equal. According to Kopyscinski, the amount of free active sides Θ_v is described by:

$$\Theta_v = 1 - \sum_i \Theta_i \qquad \textbf{4-2}$$

where Θ_i is defined as the surface coverage of a species *i*, which depends on the adsorption coefficient K_i, the partial pressure p_i and vacant sides:

$$\Theta_i = f(K_i, p_i, \Theta_v) \qquad \textbf{4-3}$$

The rate equations of adsorption and desorption for hydrogen ($H_2 + 2* \leftrightarrow 2\ H*$) are described by:

$$r_1 = k_1 \cdot p_{H_2} \cdot \Theta_v^2 \qquad \textbf{4-4}$$

$$r_1' = k_1' \cdot \Theta_H^2 \qquad \textbf{4-5}$$

As mentioned before, in equilibrium the rate of adsorption r_1 is equal to the rate of desorption r_1' and therefore the surface coverage of H_2 can be written as

$$\Theta_H^2 = \frac{k_1}{k_1'} \cdot p_{H_2} \cdot \Theta_v^2 \qquad \textbf{4-6}$$

whereby the adsorption constant is defined as

$$\frac{k_1}{k_1'} = K_1 \qquad \textbf{4-7}$$

and therefore, the surface coverage for a single hydrogen atom can be computed by:

$$\Theta_H = \sqrt{K_{H_2} \cdot p_{H_2}} \cdot \Theta_v \qquad \textbf{4-8}$$

All other reaction steps of mechanism A and B can be derived according to this approach. The correlations for mechanism A are shown below:

A2: $r_{A2} = k_{A2} \cdot p_{CO_2} \cdot \Theta_v$, $r'_{A2} = k'_{A2} \cdot \Theta_{CO_2} \cdot \Theta_v$ $\Rightarrow$ $\Theta_{CO_2} = K_{A2} \cdot p_{CO_2} \cdot \Theta_v$ **4-9**

A3: $r_{A3} = k_{A3} \cdot \Theta_{CO_2} \cdot \Theta_v$, $r'_{A3} = k'_{A3} \cdot \Theta_{CO} \cdot \Theta_O$ $\Rightarrow$ $\Theta_{CO} \cdot \Theta_O = K_{A3} \cdot \Theta_{CO_2} \cdot \Theta_v$ **4-10**

A4: $r_{A4} = k_{A4} \cdot \Theta_{CO}$, $r'_{A4} = k'_{A4} \cdot p_{CO} \cdot \Theta_v$ $\Rightarrow$ $\Theta_{CO} = K_{A4} \cdot p_{CO} \cdot \Theta_v$ **4-11**

A5: $r_{A5} = k_{A5} \cdot \Theta_{CO} \cdot \Theta_v$, $r'_{A5} = k'_{A5} \cdot \Theta_C \cdot \Theta_O$ $\Rightarrow$ $\Theta_C \cdot \Theta_O = K_{A5} \cdot \Theta_{CO} \cdot \Theta_v$ **4-12**

A6: $r_{A6} = k_{A6} \cdot \Theta_C \cdot \Theta_H$, $r'_{A6} = k'_{A6} \cdot \Theta_{CH} \cdot \Theta_v$ $\Rightarrow$ $\Theta_{CH} = K_{A6} \cdot \frac{\Theta_C \cdot \Theta_H}{\Theta_v}$ **4-13**

A7: $r_{A7} = k_{A7} \cdot \Theta_{CH} \cdot \Theta_H$, $r'_{A7} = k'_{A7} \cdot \Theta_{CH_2} \cdot \Theta_v$ $\Rightarrow$ $\Theta_{CH_2} = K_{A7} \cdot \frac{\Theta_{CH} \cdot \Theta_H}{\Theta_v}$ **4-14**

A8: $r_{A8} = k_{A8} \cdot \Theta_{CH_2} \cdot \Theta_H$, $r'_{A8} = k'_{A8} \cdot \Theta_{CH_3} \cdot \Theta_v$ $\Rightarrow$ $\Theta_{CH_3} = K_{A8} \cdot \frac{\Theta_{CH_2} \cdot \Theta_H}{\Theta_v}$ **4-15**

A9: $r_{A9} = k_{A9} \cdot \Theta_{CH_3} \cdot \Theta_H$, $r'_{A9} = k'_{A9} \cdot \Theta_{CH_4} \cdot \Theta_v$ $\Rightarrow$ $\Theta_{CH_4} = K_{A9} \cdot \frac{\Theta_{CH_3} \cdot \Theta_H}{\Theta_v}$ **4-16**

A10: $r_{A10} = k_{A10} \cdot \Theta_{CH_4}$, $r'_{A10} = k'_{A10} \cdot p_{CH_4} \cdot \Theta_v$ $\Rightarrow$ $\Theta_{CH_4} = K_{A10} \cdot p_{CH_4} \cdot \Theta_v$ **4-17**

A11: $r_{A11} = k_{A11} \cdot \Theta_O \cdot \Theta_H$, $r'_{A11} = k'_{A11} \cdot \Theta_{OH} \cdot \Theta_v$ $\Rightarrow$ $\Theta_O \cdot \Theta_H = K_{A11} \cdot \Theta_{OH} \cdot \Theta_v$ **4-18**

A12: $r_{A12} = k_{A12} \cdot \Theta_{OH} \cdot \Theta_H$, $r'_{A12} = k'_{A12} \cdot \Theta_{H_2O} \cdot \Theta_v$ $\Rightarrow$ $\Theta_{OH} = K_{A12} \cdot \frac{\Theta_{H_2O} \cdot \Theta_v}{\Theta_H}$ **4-19**

A13: $r_{A13} = k_{A13} \cdot \Theta_{H_2O}$, $r'_{A13} = k'_{A13} \cdot p_{H_2O} \cdot \Theta_v$ $\Rightarrow$ $\Theta_{H_2O} = K_{A13} \cdot p_{H_2O} \cdot \Theta_v$ **4-20**

4.3.2 Methanation

To determine the reaction rate r_{CH_4} a kinetic model can be set up for all RDS. As an example the adsorption of CO_2 is derived in model 1.

Model 1

The CO_2 adsorption is assumed as the RDS. This pathway occurs in all mechanism (A, B), thus the limiting step is A2 or B2: $CO_2 + * \leftrightarrow CO_2*$

$$r_{CH_4} = k_r \cdot p_{CO_2} \cdot \Theta_v \qquad \textbf{4-21}$$

The catalyst surface is covered by H and OH [45]. With equation 4-2 this leads to

$$\Theta_v = 1 - \Theta_H - \Theta_{OH} \qquad \textbf{4-22}$$

To calculate Θ_H and Θ_{OH} equations 4-8, 4-19 and 4-20 are necessary. Thus, the surface coverage of an OH group is

$$\Theta_{OH} = K_{OH} \cdot \frac{p_{H_2O} \cdot \Theta_v^2}{\Theta_H} \qquad \textbf{4-23}$$

Which leads with the surface coverage of hydrogen in equation 4-8 to:

$$\Theta_{OH} = K_{OH} \cdot \frac{p_{H_2O} \cdot \Theta_v}{\sqrt{p_{H_2}}} \qquad \textbf{4-24}$$

Thus, Θ_v can be expressed as

$$\Theta_v = \frac{1}{1 + K_{H_2}^{0.5} \cdot p_{H_2}^{0.5} + K_{OH} \cdot \frac{p_{H_2O}}{p_{H_2}^{0.5}}} \qquad \textbf{4-25}$$

Combined with model 1 the equation for the reaction rate is

$$r_{CH_4} = \frac{k_r \cdot p_{CO_2}}{1 + K_{H_2}^{0.5} \cdot p_{H_2}^{0.5} + K_{OH} \cdot \frac{p_{H_2O}}{p_{H_2}^{0.5}}} \qquad \textbf{4-26}$$

Model 2

The dissociation of CO_2 is assumed as the RDS. This pathway occurs in mechanism A and B, thus the limiting step is either A2: $CO_2 + 2 * \leftrightarrow CO* + O*$

$$r_{CH_4} = k_r \cdot p_{CO_2} \cdot \Theta_v^2 \qquad \textbf{4-27}$$

The catalyst surface is covered by H and OH, thus the calculation of Θ_v is analogous to model 1.

Model 3

The desorption of CO is assumed as the RDS. This pathway only occurs in mechanism A, thus the limiting step is A3: CO* ↔ CO + *

$$r_{CH_4} = k_r \cdot p_{CO} \cdot \Theta_v \quad \textbf{4-28}$$

Despite CO, the catalyst surface is covered by H and OH.

Model 4

The dissociation of CO to surface C is assumed as the RDS. This pathway only occurs in mechanism A, thus the limiting step is A4: CO* + * ↔ C* + O*

$$r_{CH_4} = k_r \cdot \Theta_{CO} \cdot \Theta_v \quad \textbf{4-29}$$

with

$$\Theta_{CO} = K_{CO} \cdot p_{CO} \cdot \Theta_v \quad \textbf{4-30}$$

this leads to:

$$r_{CH_4} = k_r \cdot K_{CO} \cdot p_{CO} \cdot \Theta_v^2 \quad \textbf{4-31}$$

Despite CO, the catalyst surface is covered by H and OH.

Model 5

The formation of formates (COOH) is assumed as the RDS. This pathway only occurs in mechanism B, thus the limiting step is B4: CO_2* + H* ↔ COOH* + *

$$r_{CH_4} = k_r \cdot \Theta_{CO_2} \cdot \Theta_H \quad \textbf{4-32}$$

with

$$\Theta_{CO_2} = K_{CO_2} \cdot p_{CO_2} \cdot \Theta_v \quad \textbf{4-33}$$

and

$$\Theta_H = \sqrt{K_{H_2} \cdot p_{H_2}} \cdot \Theta_v \quad \textbf{4-34}$$

leads to:

$$r_{CH_4} = k_r \cdot K_{CO_2} \cdot p_{CO_2} \cdot \sqrt{K_{H_2} \cdot p_{H_2}} \cdot \Theta_v^2 \quad \textbf{4-35}$$

Despite CO_2, the catalyst surface is covered by H and OH.

Model 6

The dissociation of formates is assumed as the RDS. This pathway only occurs in mechanism B, thus the limiting step is B5: COOH* + * ↔ CO* + OH*

$$r_{CH_4} = k_r \cdot \Theta_{COOH} \cdot \Theta_v \quad \textbf{4-36}$$

with

$$\Theta_{COOH} = K_{B3} \cdot \frac{\Theta_{CO_2} \cdot \Theta_H}{\Theta_v} \quad \textbf{4-37}$$

leads to:

$$r_{CH_4} = k_r \cdot K_{COOH} \cdot p_{CO_2} \cdot \sqrt{K_{H_2} \cdot p_{H_2}} \cdot \Theta_v^2 \quad \textbf{4-38}$$

Despite COOH, the catalyst surface is covered by H and OH.

Model 7

The formation of formyl is assumed as the RDS. This pathway only occurs in mechanism B, thus the limiting step is B6: CO* + H* ↔ COH* + *

$$r_{CH_4} = k_r \cdot \Theta_{CO} \cdot \Theta_H \quad \textbf{4-39}$$

with

$$\Theta_{CO} = \frac{K_{B3} \cdot p_{CO_2} \cdot \Theta_v^2}{\Theta_O} \quad \textbf{4-40}$$

According to Koschany the rate of the oxygen hydrogenation is double the rate of the RDS at steady state conditions and the equilibrium of the hydrogenation of oxygen (reaction A10 and B12, respectively) is assumed to be shifted far to the right [46]. Thus:

$$r_{B12} = 2 \cdot r_{B6} \quad \textbf{4-41}$$

whereas

$$r_{B6} = K_{B6} \cdot \Theta_{CO} \cdot \Theta_H \quad \textbf{4-42}$$

$$r_{B12} = K_{B12} \cdot \Theta_O \cdot \Theta_H \quad \textbf{4-43}$$

leads to:

$$\Theta_O = \frac{2 \cdot K_{B6}}{K_{B12}} \cdot \Theta_{CO} \quad \textbf{4-44}$$

So, the final rate equation is:

$$r_{CH_4} = k_r \cdot K_{CO} \cdot \sqrt{p_{CO_2}} \cdot \sqrt{K_{H_2} \cdot p_{H_2}} \cdot \Theta_v^2 \quad \textbf{4-45}$$

Despite CO, the catalyst surface is covered by H and OH.

Model 8

The formation of CH species is assumed as the RDS. This pathway only occurs in mechanism B, thus the limiting step is B7: COH* + * ↔ CH* + O*

$$r_{CH_4} = k_r \cdot \Theta_{COH} \cdot \Theta_v \quad \textbf{4-46}$$

This leads to:

$$r_{CH_4} = k_r \cdot K_{COH} \cdot \sqrt{p_{CO_2}} \cdot \sqrt{K_{H_2} \cdot p_{H_2}} \cdot \Theta_v^2 \quad \textbf{4-47}$$

Despite COH, the catalyst surface is covered by H and OH.

Model 9

The hydrogenation of C is assumed as the RDS. This pathway only occurs in mechanism A, thus the limiting step is A5: C* + H* ↔ CH* + *

$$r_{CH_4} = k_r \cdot \Theta_C \cdot \Theta_H \quad \textbf{4-48}$$

The surface coverage of carbon is derivated similar to model 7, thus

$$\Theta_C = K_C \cdot \sqrt[3]{p_{CO_2}} \cdot \Theta_v \quad \textbf{4-49}$$

leads to

$$r_{CH_4} = k_r \cdot K_C \cdot \sqrt[3]{p_{CO_2}} \cdot \sqrt{K_{H_2} \cdot p_{H_2}} \cdot \Theta_v^2 \quad \textbf{4-50}$$

For this case, the catalyst surface is covered by adsorbed C, H, and OH.

Model 10

The hydrogenation of CH is assumed as the RDS. This pathway occurs in mechanism A and B, thus the limiting step is A6 or B8: CH* + H* ↔ CH_2* + *

$$r_{CH_4} = k_r \cdot \Theta_{CH} \cdot \Theta_H \quad \textbf{4-51}$$

whereby Θ_{CH} is described by

$$\Theta_{CH} = K_{A6} \cdot \frac{\Theta_C \cdot \Theta_H}{\Theta_v} \quad \textbf{4-52}$$

which leads subsequently to

$$r_{CH_4} = k_r \cdot K_{CH} \cdot \sqrt[3]{p_{CO_2}} \cdot \sqrt{K_{H_2}} \cdot p_{H_2} \cdot \Theta_v^2 \quad \textbf{4-53}$$

For this case, the catalyst surface is covered by adsorbed CH, H, and OH.

Model 11

The CH_2 hydrogenation is assumed as the RDS. This pathway also occurs in both mechanism, thus the limiting step is A7 or B9: CH_2* + H* ↔ CH_3* + *

$$r_{CH_4} = k_r \cdot \Theta_{CH_2} \cdot \Theta_H \quad \textbf{4-54}$$

According to the approach in model 10 this leads to

$$r_{CH_4} = k_r \cdot K_{CH_2} \cdot \sqrt[3]{p_{CO_2}} \cdot \sqrt{K_{H_2}} \cdot p_{H_2}^{1.5} \cdot \Theta_v^2 \quad \textbf{4-55}$$

For this case, the catalyst surface is covered by adsorbed CH_2, H, and OH.

In total, there are 11 different rate equation models with different catalyst surface coverages. In model 1 and 2 adsorbed H and OH is present:

$$\Theta_v = 1 - \Theta_H - \Theta_{OH} \quad \textbf{4-56}$$

Thus, the adsorption term for the final rate equation in the presence of OH can be written as:

$$\Theta_v = 1 - \sqrt{K_{H_2} \cdot p_{H_2}} \cdot \Theta_v - K_{OH} \cdot \frac{p_{H_2O}}{\sqrt{p_{H_2}}} \cdot \Theta_v \quad \textbf{4-57}$$

or as

$$\Theta_v = \frac{1}{1 + \sqrt{K_{H_2} \cdot p_{H_2}} + K_{OH} \cdot \frac{p_{H_2O}}{\sqrt{p_{H_2}}}} \quad \textbf{4-58}$$

This approach can be continued for all models. In model 3, 4 and 7 the surface is covered by CO, H and OH, respectively:

$$\Theta_v = 1 - \Theta_{CO} - \Theta_H - \Theta_{OH} \quad \textbf{4-59}$$

The catalyst surface in model 5 could be covered by CO_2, H and OH:

$$\Theta_v = 1 - \Theta_{CO2} - \Theta_H - \Theta_{OH} \quad \textbf{4-60}$$

In model 6 the surface is covered by COOH, H and OH:

$$\Theta_v = 1 - \Theta_{COOH} - \Theta_H - \Theta_{OH} \quad \textbf{4-61}$$

In model 8 the surface coverage includes COH, H and OH:

$$\Theta_v = 1 - \Theta_{COH} - \Theta_H - \Theta_{OH} \quad \textbf{4-62}$$

In model 9 the catalyst might be covered by C, H and OH:

$$\Theta_v = 1 - \Theta_C - \Theta_H - \Theta_{OH} \quad \textbf{4-63}$$

In model 10 C, H and OH are covering the catalyst.

$$\Theta_v = 1 - \Theta_{CH} - \Theta_H - \Theta_{OH} \quad \textbf{4-64}$$

In model 11 adsorbed CH_2, H and OH are present:

$$\Theta_v = 1 - \Theta_{CH_2} - \Theta_H - \Theta_{OH} \quad \textbf{4-65}$$

According to Hernandez Lalinde et al. a total of 20 models with RDS are potentially possible whereas the published model 11 and 15 showed the highest posterior probability at a value of 61.8 % and 37.4 %, respectively[45]. Model 15 from Hernandez Lalinde et al. uses the same RDS and surface coverage as model 6 in this thesis [45]. Thus, model 6 and model 11 from Hernandez Lalinde (from now on called 'HL') were considered within this thesis. Model HL uses as the RDS the dissociation of formyl as described in a separate reaction mechanism AB (see chapter 5.1). The reaction step is AB7 [45]. For model 6 the RDS is step B4 as described in equation 4-36 (dissociation of COOH* complex).

In model 6 the surface calculation of the free vacant sides in the present of COOH, H and OH can be done by using equations AC1-4, AC1-2 (see Appendix C1, respectively) 4-8 and 4-24. Thus, the surface coverage of Θ_{COOH} can be described as:

$$\Theta_{COOH} = K_{COOH} \cdot p_{CO_2} \cdot K_{H_2}^{0.5} \cdot p_{H_2}^{0.5} \cdot \Theta_v \quad \textbf{4-66}$$

Subsequently, the free vacant side can be calculated with equation 4-61:

$$\Theta_v = \frac{1}{1 + K_{COOH} \cdot p_{CO_2} \cdot K_{H_2}^{0.5} \cdot p_{H_2}^{0.5} + \sqrt{K_{p_{H_2}} \cdot p_{H_2}} + K_{OH} \cdot \frac{p_{H_2O}}{\sqrt{p_{H_2}}}} \quad \textbf{4-67}$$

Which leads with equation 4-38 to a total rate equation:

Model 6

$$r_{CH_4} = \frac{k_r \cdot K_{COOH} \cdot p_{CO_2} \cdot K_{H_2}^{0.5} \cdot p_{H_2}^{0.5} \cdot \left(1 - \left(\frac{p_{H_2O}^2 \cdot p_{CH_4}}{p_{H_2}^4 \cdot p_{CO_2} \cdot K_{eq}}\right)\right)}{\left(1 + K_{COOH} \cdot p_{CO_2} \cdot K_{H_2}^{0.5} \cdot p_{H_2}^{0.5} + \left(K_{H_2} \cdot p_{H_2}\right)^{0.5} + K_{OH} \cdot \frac{p_{H_2O}}{p_{H_2}^{0.5}}\right)^2} \quad \textbf{4-68}$$

In a similar approach model HL can be calculated. According to Hernandez Lalinde et al. [45] the reaction equation is stated as:

Model HL

$$r_{CH_4} = \frac{k_r \cdot K_{COH} \cdot p_{CO_2}^{0.5} \cdot K_{H_2} \cdot p_{H_2} \cdot \left(1 - \left(\frac{p_{H_2O}^2 \cdot p_{CH_4}}{p_{H_2}^4 \cdot p_{CO_2} \cdot K_{eq}}\right)\right)}{\left(1 + K_{COH} \cdot p_{CO_2}^{0.5} \cdot p_{H_2}^{0.5} + \left(K_{H_2} \cdot p_{H_2}\right)^{0.5} + K_{OH} \cdot \frac{p_{H_2O}}{p_{H_2}^{0.5}}\right)^2} \quad \textbf{4-69}$$

For both equations 4-68 and 4-69, respectively the reaction rate r_{CH_4} is given in mol s^{-1} kg_{cat}^{-1}, k_r is the rate constant of CO_2 methanation, K_{H_2}, K_{OH}, K_{COH} and K_{COOH} are adsorption constants. The partial pressure p_i is given in bar. The equilibrium constant for the CO_2 methanation is defined as K_{eq}. Additionally, a modeling of the water gas shift reaction was also considered by Hernandez Lalinde et al. which is not used here. [45]

4.4 Modeling and kinetic parameter determination

The previously assumed rate equations can be validated by a computational model analogous to Kopyscinski's approach for the methanation of CO [17]. The goal is to calculate gas concentrations with estimated parameters and to compare them with measured results. A one-dimensional (1-D) mathematical model can be used to study kinetics and parameter fittings. The model is based on two different phases, a bulk phase and a catalyst phase (see chapter 2-2) which are connected by diffusive mass transfer. Chemical reactions in the bulk phase can be neglected due to preliminary empty reactor experimenents. Thus, a constant concentration and temperature profile in y-direction is assumed. In addition, several further assumptions to reduce complexity are considered, namely:

- steady-state conditions and ideal gas behavior,
- isothermal behaviour → no energy balance,
- isobaric behaviour → no momentum balance,
- equal catalyst mass distribution along the plate (see chapter 4-2),
- no carbon deposition,
- velocity change caused by volume contracten is not considered,
- transport resistance is neglected due to thin catalyst layer
- average = measured gas concentration

Figure 4-8 shows an illustrated version of a finite control volume with a specific length Δx for a 1-D model.

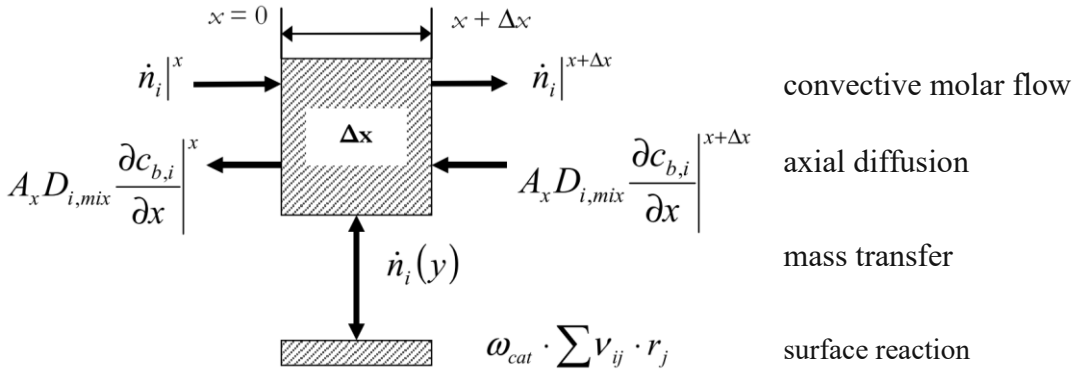

Figure 4-8 Finite control volume of the reactor

According to the law of mass conservation the illustrated model can be formulated as:

$$0 = \dot{n}_i|^{x} - \dot{n}_i|^{x+\Delta x} + A_x \cdot D_{i,mix} \cdot \left(-\frac{\partial c_{b,i}}{\partial x}\Big|^{x} + \frac{\partial c_{b,i}}{\partial x}\Big|^{x+\Delta x} \right) - \dot{n}_i(y) \qquad \textbf{4-70}$$

with the area A_x defined by:

$$A_x = b \cdot h \qquad \textbf{4-71}$$

where b and h describe width and height of a control volume, respectively. The missing mass transfer correlation between the bulk phase and the catalyst phase can be written as:

$$\frac{\dot{n}_i}{A_y} = K_{G,i} \cdot \Delta c_i \qquad \textbf{4-72}$$

where $K_{G,i}$ represents the mass transfer coefficient in $m \cdot s^{-1}$ and Δc_i the driving force, namely, the concentration difference of a species i in both phases $(c_{b,i} - c_{s,i})$. The surface area of the control volume in y-direction A_y is defined by:

$$A_y = \Delta x \cdot b \qquad \textbf{4-73}$$

where Δx is as mentioned the length and b the width of the control volume.
The molar balances of a species i in the bulk and catalyst phase can now be calculated by:

$$0 = -\frac{\partial \dot{n}_{b,i}}{\partial x} + A_x \cdot \frac{\partial}{\partial x}\left(D_{i,mix} \cdot \frac{\partial c_{b,i}}{\partial x} \right) - b \cdot K_{G,i} \cdot (c_{b,i} - c_{s,i}) \qquad \textbf{4-74}$$

$$-\left[\frac{mol}{s \cdot m}\right] + \left[m^2 \cdot \frac{m^2}{s}\frac{mol}{m^3 \cdot m^2}\right] - \left[m \cdot \frac{m}{s}\frac{mol}{m^3}\right]$$

$$0 = b \cdot K_{G,i} \cdot \left(c_{b,i} - c_{s,i}\right) + \omega_{cat} \cdot R_i \qquad \textbf{4-75}$$

$$\left[m \cdot \frac{m}{s}\frac{mol}{m^3}\right] + \left[\frac{kg_{cat}}{m}\frac{mol}{s \cdot kg_{cat}}\right]$$

The dimensionless Sherwood number is defined by:

$$Sh = \frac{K_{G,i} \cdot l_{ch}}{D_{i,mix}} \qquad \textbf{4-76}$$

Applying the Sherwood correlation on equation 4-74 and 4-75, respectively, the molar balance for the bulk phase transforms to:

$$0 = -\frac{\partial \dot{n}_{b,i}}{\partial x} + A_x \cdot \frac{\partial}{\partial x}\left(D_{i,mix} \cdot \frac{\partial c_{b,i}}{\partial x}\right) - b \cdot \frac{Sh \cdot D_{i,mix}}{l_{ch}} \cdot \left(c_{b,i} - c_{s,i}\right) \qquad \textbf{4-77}$$

and the molar balance for the catalyst phase converts to:

$$0 = b \cdot \frac{Sh \cdot D_{i,mix}}{l_{ch}} \cdot \left(c_{b,i} - c_{s,i}\right) + \omega_{cat} \cdot R_i \qquad \textbf{4-78}$$

whereas the overall reaction term R_i is defined by:

$$R_i = \sum v_{ij} \cdot r_j \qquad \textbf{4-79}$$

Thus, the global reaction rate of the involved species H_2, CO_2, CO, CH_4, H_2O and Ar for the CO_2 methanation is:

$$R_{H_2} = -4 \cdot r_1 \qquad \textbf{4-80}$$

$$R_{CO_2} = -r_1 \qquad \textbf{4-81}$$

$$R_{CO} = 0 \qquad \textbf{4-82}$$

$$R_{CH_4} = r_1 \qquad \textbf{4-83}$$

$$R_{H_2O} = 2 \cdot r_1 \qquad \textbf{4-84}$$

$$R_{Ar} = 0 \qquad \textbf{4-85}$$

The molar balance of the bulk phase (equation 4-77) consists of a second order derivative of x, therefore, two boundary conditions are necessary:

$$\dot{n}_{b,i}\big|_{x=0} = \dot{n}_{b,i,feed} - A_x \cdot D_{i,mix} \frac{\partial c_{b,i}}{\partial x} \qquad \textbf{4-86}$$

$$\left.\frac{\partial \dot{n}_{b,i}}{\partial x}\right|_{x=L} = 0 \qquad \textbf{4-87}$$

At position $x = 0$ (initial condition) the convective molar flow $\dot{n}_{b,i}$ is the difference between the initial molar flow of the feed and the axial diffused molar flow and at position $x = L$ the gradient of the molar flow is defined as zero.

One dimensional model without axial dispersion:

The bulk phase equation is defined by:

$$0 = -\frac{\partial \dot{n}_{b,i}}{\partial x} - b \cdot \frac{Sh \cdot D_{i,mix}}{l_{ch}} \cdot \left(c_{b,i} - c_{s,i}\right) \qquad \textbf{4-88}$$

The equation for catalyst phase is described by:

$$0 = b \cdot \frac{Sh \cdot D_{i,mix}}{l_{ch}} \cdot \left(c_{b,i} - c_{s,i}\right) + \omega_{cat} \cdot R_i \qquad \textbf{4-89}$$

For a 1-D model without axial dispersion, the molar balance of the bulk phase changed to a first order derivative, thus, there is only one boundary condition at the initial value $x = 0$:

$$\dot{n}_i|_{x=0} = \dot{n}_{b,i,feed} \qquad \textbf{4-90}$$

Thermodynamic properties

Since the diffusion coefficient and the equilibrium constant K_{eq} are temperature dependent thermodynamic properties, they were calculated for a specific temperature and gas composition. The diffusion coefficient of a species i in a gas mixture was described by Wilke [47]

$$D_{i,mix} = \frac{1 - x_i}{\sum_j \frac{x_j}{D_{i,j}}} \qquad \textbf{4-91}$$

whereas the binary gas-phase diffusion coefficient can be calculated according to Fuller et al. [48] as follows:

$$D_{i,j} = 0.01013 \cdot \frac{T^{1.75} \cdot \left(\frac{1}{M_i} + \frac{1}{M_j}\right)^{0.5}}{p \cdot \left[\left(\sum v_i\right)^{1/3} + \left(\sum v_j\right)^{1/3}\right]^2} \quad \textbf{4-92}$$

In equation 4-51 the temperature T is in units of K, the molar mass M in g · mol^{-1}, the pressure p in Pa and the so called 'diffusion volumes' $\sum v$ in m^3 · mol^{-1}. The corresponding values for the molar mass and the diffusion volumes of the considered species are listed in Table 4-2 [49]. It has to be mentioned that the data for atoms and molecules, e.g., H_2, CO, CO_2, and Ar were determined as such, the diffusion volumes for CH_4 and H_2O however were calculated by a simple addition of the determined atomic diffusion volumes for H, C and O, respectively.

Table 4-1: Molar mass and diffusion volumes for different species

	M [g · mol^{-1}]	$\sum v$ [m^3 · mol^{-1}]
H_2	2.016	6.12
CO_2	44.01	26.7
CO	28.01	18.0
CH_4	16.04	25.14
H_2O	18.02	13.1
Ar	39.95	16.12

Modeling with Athena Visual Studio

For the modeling a program called Athena Visual Plus® v 20.1, developed by Caracotsios and Stewart was used within this thesis [50]. The parameter estimation of the pre-exponential factors $\theta_{k,j}$, $\theta_{K,i}$ as well as the activation energy $\theta_{E,j}$ and heat of adsorption $\theta_{H,i}$ was evaluated by a single response Bayesian estimation within the GREGPLUS solver.

$$k_j = k_j^0 \cdot exp\left(-\frac{E_{A,j}}{\Re \cdot T}\right) \quad \textbf{4-93}$$

$$K_i = K_i^0 \cdot exp\left(-\frac{\Delta H_i}{\Re \cdot T}\right) \quad \textbf{4-94}$$

Starting from the base equations of Arrhenius' (eq. 4-94) and van't Hoff (eq. 4-95) modified versions were used to limit high orders of magnitude for the pre-exponential factors k_j^0 and K_i^0, as described by Hernandez Lalinde et al [45]. As a base temperature T_{base} 350 °C is used. With $\theta_{k,j} = ln(k_{j,Tbase})$ and $\theta_{K,i} = ln(K_{i,Tbase})$ for the pre-exponential factors and $\theta_{E,j} = \frac{E_{A,j}}{\Re \cdot T_{base}}$ for activation energy as well as $\theta_{H,i} = \frac{\Delta H_i}{\Re \cdot T_{base}}$ for the heat of adsorption the modified equations turn to:

$$k_j = exp(\theta_{k,j}) \cdot exp\left(\theta_{E,j}\left(1 - \frac{T_{base}}{T}\right)\right) \quad \textbf{4-95}$$

$$K_i = exp(\theta_{K,i}) \cdot exp\left(\theta_{H,i}\left(1 - \frac{T_{base}}{T}\right)\right) \quad \textbf{4-96}$$

Modeling description

The model in Athena Visual Plus® v 20.1 was build up step-by-step starting from the reaction equation. First, only the algebraic equation in the catalyst phase was considered (see equation 4-89). Next, the diffusion model was set up to calculate the material transfer between the bulk and catalyst phase. In the bulk, only the first spatial resolved measurement was considered and subsequently enlarged for the whole reactor. Finally, all 182 experimental data points were added and the parameter estimation was started. Since the RWGS reaction was not considered in the model the 'Bayesian Single Response Estimation' was set as solver option with measured CH_4 concentration as response data. Analogous to Hernandez-Lalinde et al. only the central part of the catalytic plate (10 to 40 mm) was considered in the model [45]. However, the model code is shown in Appendix B2.

The results for the parameter estimation of model HL and model 6 are given in Table 4-3 and 4-5, respectively. In each table all estimated dimensionless parameters are summarized with optimal estimated values, HPD (highest posterior density) intervals and the normalized covariance matrix. The covariance matrix values E_{ij} can be interpreted as a correlation coefficient between two paramters i and j where 1.0 (-1.0) shows a high correlation (anti correlation) [45]. The HPD interval encases a region where 95 % of all potential estimation results are found [45].

Table 4-2 Modeling results for model HL, dimensionless parameters, HDP interval and normalized covariance matrix

Model HL	95% HPD interval	Normalized covariance matrix							
$\ln k_r(T_{ref})$	3.12 ± 0.09	1.00							
$E_{Ar}/(\Re \cdot T_{ref})$	19.68 ± 20.06	-0.28	1.00						
$\ln K_{COH}(T_{ref})$	-1.71 ± 1.34	0.00	0.00	1.00					
$\Delta H_{COH}/(\Re \cdot T_{ref})$	-0.40 ± 0.85	0.00	0.00	0.78	1.00				
$\ln K_H(T_{ref})$	-3.29 ± 1.51	0.00	0.00	-0.99	-0.80	1.00			
$\Delta H_H/(\Re \cdot T_{ref})$	-6.52 ± 23.84	0.27	-1.00	0.00	0.00	0.00	1.00		
$\ln K_{OH}(T_{ref})$	1.51 ± 0.28	0.73	0.69	0.00	0.00	0.00	0.69	1.00	
$\Delta H_{OH}/(\Re \cdot T_{ref})$	6.60 ± 1.96	0.21	-0.98	0.00	0.00	0.00	0.98	0.63	1.00
RSS	**34.1**								

The normalized covariance matrix in Table 4-3 shows that the dimensionless parameters for the the pre-exponential factors of H as well as COH and the heat of adsorption of COH were estimated in a separate modeling step (element values = 0). For the heat of adsorption of the hydroxyl group an initial result of -6.52 was modeled with and HPD interval of 23.84 and a normalized covariance matrix value of -1.00 in respect to the activation energy. Therefore, also the activation energy has a high uncertainty with an HDP region higher than the initial result of 19.86. Further, this results in a smaller confidence level in respect to fixed ambience for the second estimation step. However, the residual sum of squares (*RSS*) did not change significantly in the following run.

In Table 4-4 the calculated kinetic parameters for model HL are shown. The value for k_r of 22.65 mol kg_{cat}^{-1} s^{-1} $bar^{-0.5}$ is higher than in literature and the activation energy of 102,89 kJ mol^{-1} with such a high HDP interval can not be compared. However, due to the different approach of lumped parameters a comparison with published data from Hernandez-Lalinde et al. is difficult [45]. Thus, these values have to be used with caution. Additional modeling data in different pressure ranges could lead to an improved HPD interval.

Table 4-3 Estimated kinetic parameters plus HPD intervals for activation energy and heat of adsorption

Parameter	Units	Values
$k_r(T_{ref})$	mol kg_{cat}^{-1} s^{-1} $bar^{-0.5}$	22.65
E_{Ar}	kJ mol^{-1}	102.89 ± 103.93
$K_{COH}(T_{ref})$	$bar^{-0.5}$	0.18
ΔH_{COH}	kJ mol^{-1}	-2.07 ± 4.40
$K_H(T_{ref})$	bar	0.04
ΔH_H	kJ mol^{-1}	-33.78 ± 123.52
K_{OH}	bar^{-1}	4.53
ΔH_{OH}	kJ mol^{-1}	34.19 ± 10.15

The parity plot for model HL in Figure 4-9 shows the predicted gas concentration from the parameter estimation in Athena versus the observed experimental data. The computational model result for methane is mainly in the ± 15 % confidence interval, whereby predicted values exceeds both upper and lower limit by a small margin. However, there is a slight drift towards the + 15 % limit with increasing reactor length. In Figure 4-10 the modeled gas concentration is pictured along the catalytic plate. For hydrogen, the deviation between observed and predicted gas concentration differs by up to 4%.

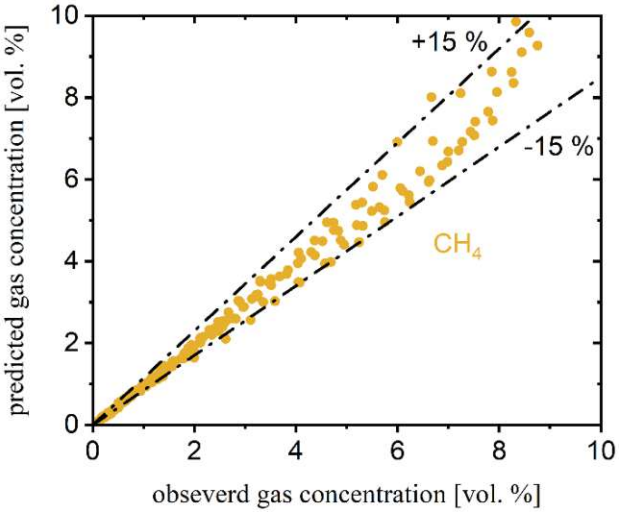

Figure 4-9 Observed and predicted gas concentration (model HL) of (●) CH_4 in a parity plot with a ± 15 % confidence interval

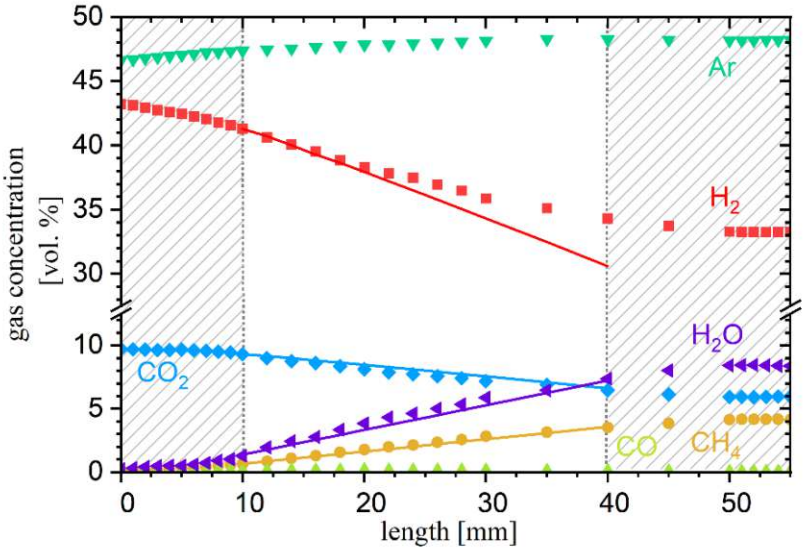

Figure 4-10 Gas concentration along catalytic plate (▼) Ar, (■) H_2, (◀) H_2O, (◆) CO_2, (●) CH_4 with estimated results ('model HL' shown as a line) for Ex. 1a at a temperature of 350 °C and a total flow rate of 110 $ml_N \cdot min^{-1}$. The hatched area is not modeled

As for model HL the dimensionless parameters for model 6 were estimated in two separated steps with indetermined results in the first run for the pre-exponential factors as well as the heat of adsorption for COOH and hydrogen. In the second loop the already estimated parameters were marked as fixed and only the remaining four elements were estimated. This resulted in a big HPD interval for $\ln(K_{COOH})$, $\ln(K_H)$ and ΔH_H. The values for *RSS* remained nearly the same.

Table 4-4 Modeling results for model 6, dimensionless parameters, HPD interval and normalized covariance matrix

Model 6	**95% HPD interval**	**Normalized covariance matrix**							
$\ln k_r(T_{ref})$	3.28 ± 0.10	1.00							
$E_{Ar}/(\Re \cdot T_{ref})$	19.92 ± 1.28	-0.48	1.00						
$\ln K_{COOH}(T_{ref})$	-1.63 ± 3.59	0.00	0.00	1.00					
$\Delta H_{COOH}/(\Re \cdot T_{ref})$	-0.36 ± 2.92	0.00	0.00	-0.77	1.00				
$\ln K_H(T_{ref})$	-0.95 ± 1.70	0.00	0.00	-1.00	0.76	1.00			
$\Delta H_H/(\Re \cdot T_{ref})$	-0.22 ± 6.19	0.00	0.00	0.78	-1.00	-0.78	1.00		
$\ln K_{OH}(T_{ref})$	1.64 ± 0.20	0.80	-0.17	0.00	0.00	0.00	0.00	1.00	
$\Delta H_{OH}/(\Re \cdot T_{ref})$	5.91 ± 1.52	-0.73	0.68	0.00	0.00	0.00	0.00	-0.80	1.00
RSS	**36.3**								

Table 4-5 Estimated kinetic parameters for model 6 plus HDP intervals for activation energy and heat of adsorption

Parameter	Units	Values
$k_r(T_{ref})$	mol kg_{cat}^{-1} s^{-1} $bar^{-0.5}$	26.58
E_{Ar}	kJ mol^{-1}	103.20 ± 6.63
$K_{COOH}(T_{ref})$	$bar^{-0.5}$	0.19
ΔH_{COOH}	kJ mol^{-1}	-1.86 ± 15.13
$K_H(T_{ref})$	bar	0.38
ΔH_H	kJ mol^{-1}	-1.14 ± 32.07
K_{OH}	bar^{-1}	5.16
ΔH_{OH}	kJ mol^{-1}	30.61 ± 7.87

To test the dimensionless parameters modeled in a separate estimation, a new loop was started for both models with already estimated results for H and COX. This estimation did not result in any parameter deviation after the third significant digit.

Activation energy in model 6 is in a similar range as in model HL. As for model HL the results may differ from literature due to a change in lumped parameters. For model 6 the parity plot is also comparable to model HL in Figure 4-9. The predicted gas concentration of methane is mostly within a ± 15 % confidence interval with only a few outliers. An upwards trend towards the positive confidence limit for higher observed concentration is also visible. The gas concentration along the catalytic plate also tends to a gap for hydrogen between modeled and experimental data.

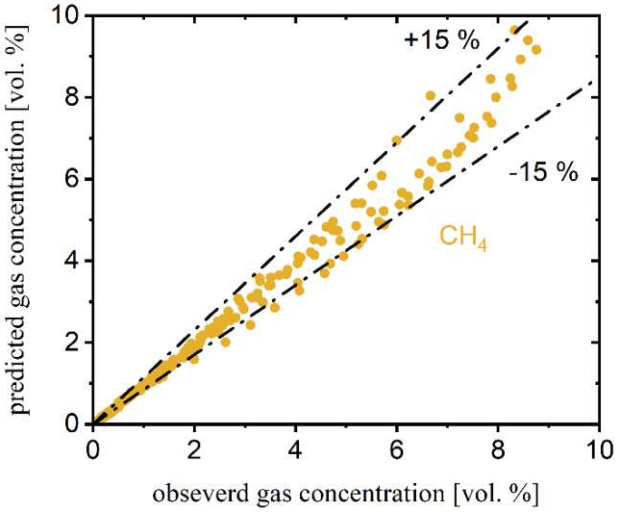

Figure 4-11 Observed and predicted gas concentration (model 6) of (●) CH_4 in a parity plot with a ± 15 % confidence interval

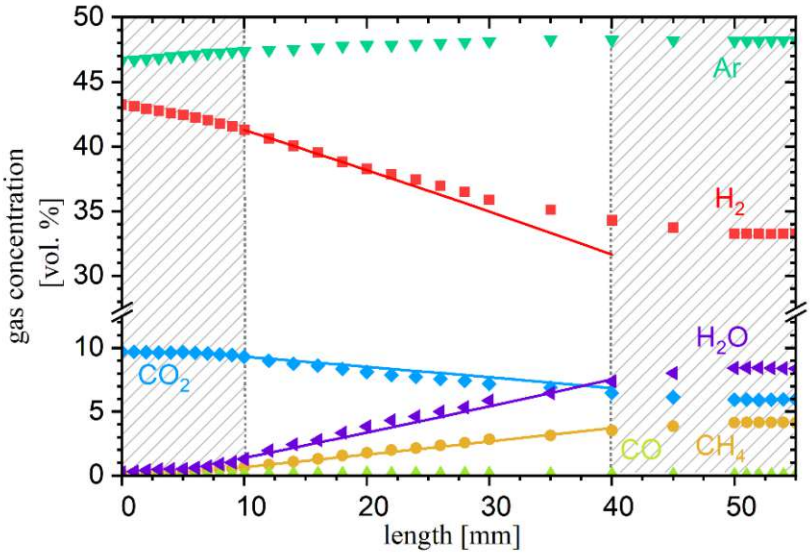

Figure 4-12 Gas concentration along catalytic plate (▼) Ar, (■) H_2, (◀) H_2O, (◆) CO_2, (●) CH_4 with estimated results ('model 6' shown as a line) for Ex. 1a at a temperature of 350 °C and a total flow rate of 110 $ml_N \cdot min^{-1}$. The hatched area is not modeled

Summarized, the modeling results show a couple of findings for the CO_2 methanation for a Ni-Al_2O_3 catalyst:

1. For both models from Hernandez Lalinde et al. [45] (HL and model 6) the predicted gas concentration for the single response (CH_4) is within a confidence interval of ± 15 %.
2. The activation energy with 102.89 and 103.2 kJ mol^{-1} is in the rage of published literature [45]. Still, it is noteworthy to mention that in this thesis no reversed water gas shift reaction (RWGS) was considered in the model.
3. In both models the pre-exponential factors of K_{COX} and K_{H2} were estimated in a separate second run.
4. The residual sum of squares *RSS* is comparable for both models. However, the activation energy in model HL is highly uncertain.
5. The parity plot slightly drifts away at the end of the modeled area. Therefore, it is reasonable to cover only the reactor length from 10 to 40 mm.
6. Considering the HDP intervals there is a slight indication for the COOH* complex as the RDS.

Chapter 5

5 Conclusions and Recommendations

5.1 Conclusions

5.1.1 Modeling

As described in chapter 4.3.2 a third possible mechanism for the CO_2 methanation is used by Hernandez Lalinde et al [45]. A drawing of all possible pathways (mechanim A, B and AB) is shown in Figure 5-1. The third mechanism – called intermediate mechanism AB – is highlighted in a dashed rectangle. This pathway includes an adsorption and dissoctiation of CO_2 according to mechanism A (A1 to A3) and a subsequent formation of formaldehyde before the carbon-oxygen bond dissociation. The formation of CH_4 and H_2O are identical for mechanism AB [45].

In total there are 16 reaction steps for mechanism AB (shown in Table 5-1) whereas only step AB4 to AB10 are determined as RDS. The development of rate equation for other RDS of mechanism AB can be derived analogous to model 1 shown in this thesis, with catalyst coverage of CO_2, CO, COH, COH_2, CH, CH_2, H and OH [45].

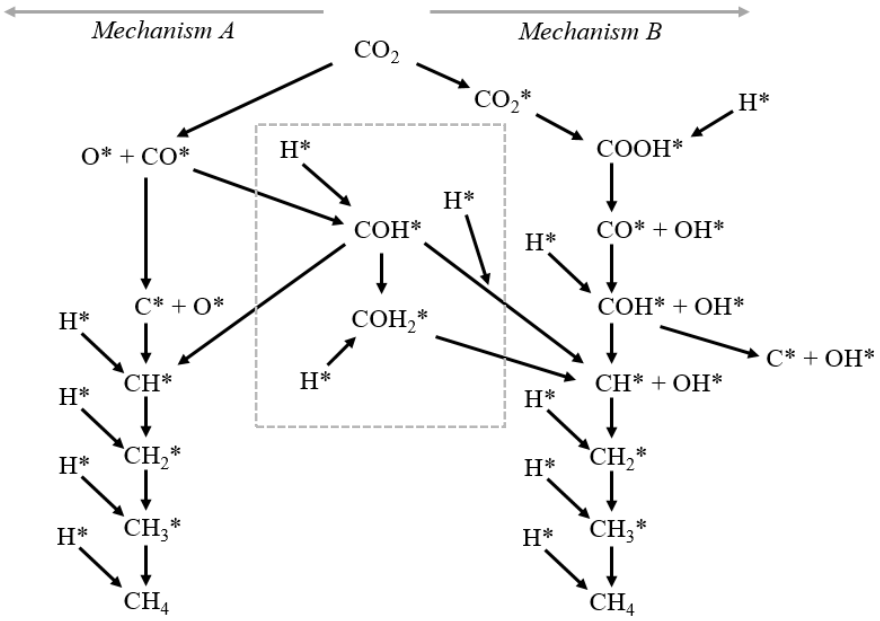

Figure 5-1: Reaction pathway with mechanism AB in dashed lines, adapted from [51]

Table 5-1 Step-by-step reaction pathways (mechanism AB) with possible rate-determining steps (RDS) [45]

H_2	+ 2*	↔	2 H*			Adsorption of H_2	**AB1**
CO_2	+ *	↔	CO_2*			Adsorption of CO_2	**AB2**
CO_2*	+ *	↔	CO*	+ O*		Dissociation of CO_2	**AB3**
CO*	+ H*	↔	HCO*	+ *	RDS	Formation of formyl	**AB4**
CO*	+ 2H*	↔	H_2CO*	+ 2*	RDS	Formation of H_2CO	**AB5**
HCO*	+ *	↔	CH*	+ O*	RDS	Dissociation of formyl	**AB6**
HCO*	+ H*	↔	CH*	+ OH*	RDS	Dissociation of formyl	**AB7**
H_2CO*	+ *	↔	CH*	+ OH*	RDS	Dissociation of H_2CO	**AB8**
CH*	+ H*	↔	CH_2*	+ *	RDS	Hydrogenation of CH	**AB9**
CH_2*	+ H*	↔	CH_3*	+ *	RDS	Hydrogenation of CH_2	**AB10**
CH_3*	+ H*	↔	CH_4*	+ *		Hydrogenation of CH_3	**AB11**
CH_4*		↔	CH_4(g)	+ *		Desorption of CH_4	**AB12**
O*	+ H*	↔	OH*	+ *		OH formation	**AB13**
OH*	+ H*	↔	H_2O*	+ *		H_2O formation	**AB14**
H_2O*		↔	H_2O(g)	+ *		H_2O desorption	**AB15**
CO*		↔	CO(g)			CO desorption	**AB16**

* free active side
CO* Adsorbed species (e.g. adsorbed carbon monoxide)
RDS Rate-determining step (proposed from literature)

As noted before the RDS for model HL and model 6 uses a COH* or a COOH* complex. A schematic drawing of the RDS configuration is shown in Figure 5-2. It is not clear whether hydrogen is bonded directly to carbon or is present with oxygen in form of a hydroxyl species. Thus, both variants are pictured below.

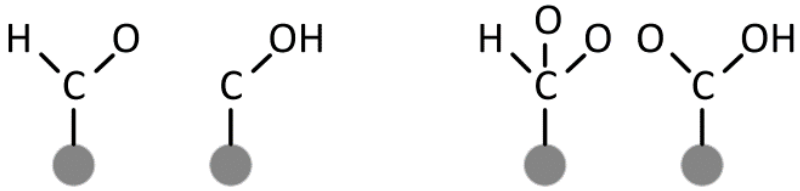

Figure 5-2 Drawing of RDS configuration for HL11 (left) and model 6 (right) [51]

5.2 Recommendations for Future Work

An updated computational model is needed to define more precisely the RDS. Therefore, a possible solution is a splitted feedback loop with several modeling packs (f.e. 0 – 10, 10 – 40, 40 – 55 mm). Additionally, the measured Ar gas composition can be used as a fixed parameter which is only allowed to change within a small region.

Additionally, in future works a bigger variety of catalysts have to be evaluated to reduce activation energy for CO_2 methanation. For this purpose an optically accessible catalytic plate reactor with spatially resolved measurement is a useful concept. For an industrial use a lot of research is still to do. As a bridge technology to an emission free environment a synthetic natural gas reactor can be considered. In the industry the feed gases CO_2 and H_2 have to be present in high concentrations and the outgoing gas mix needs to be separated. Thus, the plate reactor should operate at a higher pressure to use the pressure as a driving force for any subsequent CH_4 splitting process, e.g. membranes.

In future models the possibility of two separate reaction pathways have to be considered. There is still an open question about the correct reaction mechanism. Thus, it is also possible that the CO_2 methanation follows two co-existing pathways.

Additionally, the calculation of the plate curvature (see chapter 3.4.1 and 4.2) is inaccurate. In Figure 4-6 the schematic drawing of the plate correction does not include an overall bending of the plate. Thus, there can be a curvature change within a 10 mm range which leads to a triangle shape instead of a trapezoidal. Hence, a wrong catalyst mass distribution is determined and therefore, a deviation in the modeling result is possible.

However, for other chemical processes the use of a plate reactor for other catalytic processes is a suitable way to gain more knowledge about catalysts and RDS.

In times of climate crisis catalysts are a big player in reducing energy invest and producing essential goods.

Nomenclature

Latin symbols

A	m^2	Area
b	m	Width
c	$mol \cdot m^3$	Concentration
$c_{p,i}$	$kJ \cdot mol^{-1} \cdot K^{-1}$	Specific heat capacity
Δc	$mol \cdot m^3$	Driving force
D	$m^2 \cdot s^{-1}$	Diffusion coefficient
E_A	$kJ \cdot mol^{-1}$	Activation Energy
h	m	Height
$\Delta H_{f,i}^0$	$kJ \cdot mol^{-1}$	Standard enthalpy of formation
ΔH_R^0	$kJ \cdot mol^{-1}$	Standard reaction enthalpy
$\Delta H_R(T)$	$kJ \cdot mol^{-1}$	Heat of reaction
K_i	$mol \cdot Pa^{-1} \cdot s^{-1}$	Adsorption coefficient (of species i)
K_G	$m \cdot s^{-1}$	Mass transfer coefficient
K_P	-	Proportional gain
K_{Pu}	-	Ultimate proportional gain

k_r	differ	Reaction constant
M	$g \cdot mol^{-1}$	Molar mass
$\dot{n}$	$mol \cdot s^{-1}$	Molar flow
p	Pa	Pressure
P_u	s	Ultimate period
$\Re$	$kJ \cdot mol^{-1} \cdot K^{-1}$	Gas constant
R	$mol \cdot s^{-1}$	Overall reaction term
r	$mol \cdot s^{-1}$	Rate (e.g. reaction rate, adsorption/desorption rate)
S	-	Selectivity
Sh	-	Sherwood number
$S(\theta_k)$	-	Objective function
T	K	Temperature
T_0	K	Standard temperature (298.15 K)
T_d	s	Derivative time
T_i	s	Integrative time
T_S	°C	Surface temperature of the plate
X	-	Conversion
Y	-	Yield

Greek symbols

Θ_i	-	Surface coverage of species i
Θ_v	-	Free active side
ν_i	-	Stoichiometric coefficient
ω	$kg \cdot m^{-1}$	Mass distribution

Subscripts and superscripts

ads	Adsorbed
b	Bulk phase
BET	Brunauer – Emmett – Teller
cal	Calcination
cat	Catalyst
g	Gauge pressure
i	Species i
mix	Gas mixture
N	Normal temperature and pressure (20 °C, 1 bar)
s	Solid phase (catalyst)
x	x-Direction
y	y-Direction

Abbreviation

1-D	One-dimensional
CFD	Computational fluid dynamics
CPE	Chemical and process engineering
CPR	Catalytic plate reactor
C*	Adsorbed species (e.g. adsorbed carbon)
IR	Infrared
IUPAC	International Union of Applied Chemistry
EISA	Evaporation-induced self-assembly
Ex	Experiment
FC	Frame coating
H1	Hysteresis (e.g. hysteresis 1)
HPD	Highest posterior density
n/a	Not available

MS	Mass spectrometer
OM	Ordered mesoporous catalyst
OMA	Ordered mesoporous alumina supported catalyst
P2G	Power to Gas
PID	Proportional-integral-derivate
P&ID	Piping and instrumentation diagram
RDS	Rate-determining step
RO	Reverse osmosis
RSS	Residual Sum of Squares
Rx	Reaction
SEM	Scanning electron microscope
SNG	Synthetic Natural Gas
TPR	Temperature-programmed reduction
WGS	Water-gas shift
ZN	Ziegler – Nichols
*	Free active side

Solid species

Al	Aluminum
C	Carbon
Co	Cobalt
Fe	Iron
Ni	Nickel
NiO	Nickel oxide
Rh	Rhodium
Ru	Ruthenium

Liquid species

HNO_3	Nitric Acid

Gas species

Ar	Argon
CO	Carbon monoxide
CO_2	Carbon dioxide
CH_4	Methane
H_2	Hydrogen
H_2O	Water

References

[1] H. W. Kendall, "World Scientists' Warning to Humanity," *A Distant Light*. pp. 198–201, 1997, doi: 10.1007/978-1-4419-8507-1_19.

[2] W. J. Ripple *et al.*, "World Scientists ' Warning to Humanity : A Second Notice," vol. XX, no. X, pp. 1–3, 2017, doi: 10.1093/biosci/bix125/4605229.

[3] European Council, *Proposal for a DIRECTIVE OF THE EUROPEAN PARLIAMENT AND OF THE COUNCIL on the promotion of the use of energy from renewable sources (recast)*, vol. 0382, no. 2016. 2017.

[4] Government of Canada, *PAN - CANADIAN FRAMEWORK on Clean Growth and Climate Change*. 2016.

[5] H. Chen, T. Ngoc, W. Yang, C. Tan, and Y. Li, "Progress in electrical energy storage system : A critical review," *Prog. Nat. Sci.*, vol. 19, no. 3, pp. 291–312, 2009, doi: 10.1016/j.pnsc.2008.07.014.

[6] I. Hadjipaschalis, A. Poullikkas, and V. Efthimiou, "Overview of current and future energy storage technologies for electric power applications," vol. 13, pp. 1513–1522, 2009, doi: 10.1016/j.rser.2008.09.028.

[7] R. B. Schainker, "Executive Overview : Energy Storage Options For A Sustainable Energy Future," pp. 1–6.

[8] REN 21, "Renewables Global Futures Report: Great Debates Towards 100% Renewable Energy," 2017.

[9] M. G??tz *et al.*, "Renewable Power-to-Gas: A technological and economic review," *Renew. Energy*, vol. 85, pp. 1371–1390, 2016, doi: 10.1016/j.renene.2015.07.066.

[10] M. Conte, P. P. Prosini, and S. Passerini, "Overview of energy / hydrogen storage : state-of-the-art of the technologies and prospects for nanomaterials," vol. 108, pp. 2–8, 2004, doi: 10.1016/j.mseb.2003.10.107.

[11] P. Sabatier and J.-B. Senderens, “New synthesis of methane,” *J. Chem. Soc.*, vol. 82, p. 333, 1902.

[12] V. A. Naumov and O. V Krylov, “Kinetics of the Sabatier reaction over a nickel catalyst in a flow-circulation system,” *Kinet. Katal*, vol. 20, pp. 1344–1346, 1979.

[13] S. ichiro Fujita, H. Terunuma, M. Nakamura, and N. Takezawa, “Mechanisms of Methanation of CO and CO2 over Ni,” *Ind. Eng. Chem. Res.*, vol. 30, no. 6, pp. 1146–1151, 1991, doi: 10.1021/ie00054a012.

[14] S. ichiro Fujita, M. Nakamura, T. Doi, and N. Takezawa, “Mechanisms of methanation of carbon dioxide and carbon monoxide over nickel/alumina catalysts,” *Appl. Catal. A, Gen.*, vol. 104, no. 1, pp. 87–100, 1993, doi: 10.1016/0926-860X(93)80212-9.

[15] BYU DIPPR® Thermophysical Properties Laboratory, “DIPPR® 801 Database,” 2017. .

[16] H. Le Châtelier, “Experimental and Theoretical Studies on Chemical Equilibrium,” in *Annales des Mines*, vol. 13, no. 2, 1888, pp. 157–382.

[17] J. Kopyscinski, “Production of synthetic natural gas in a fluidized bed reactor,” pp. 1–252, 2010, doi: 10.3929/ethz-a-006031831.

[18] G. D. Weatherbee and C. H. Bartholomew, “Hydrogenation of CO2 on Group VIII Metals,” vol. 472, pp. 460–472, 1982.

[19] D. Schlereth, “Kinetic and Reactor Modeling for the Methanation of Carbon Dioxide,” 2015.

[20] J. A. Hernandez Lalinde, “Development of a catalytic plate reactor with spatially resolved measurement capability to investigate CO2 methanation mechanism,” 2016.

[21] P. Frontera, A. Macario, M. Ferraro, and P. L. Antonucci, “Supported catalysts for CO2 methanation: A review,” *Catalysts*, vol. 7, no. 2, pp. 1–28, 2017, doi: 10.3390/catal7020059.

[22] A. Aljishi, G. Veilleux, J. Augusto, H. Lalinde, and J. Kopyscinski, “Applied Catalysis A , General The e ff ect of synthesis parameters on ordered mesoporous nickel alumina catalyst for CO 2 methanation,” *Appl. Catal. A, Gen.*, vol. 549, no. October 2017, pp. 263–272, 2018, doi: 10.1016/j.apcata.2017.10.012.

[23] L. Xu *et al.*, “CO $_2$ methanation over a Ni based ordered mesoporous catalyst for the production of synthetic natural gas,” *RSC Adv.*, vol. 6, no. 34, pp. 28489–28499, 2016, doi: 10.1039/C6RA01139J.

[24] W. Wang and J. Gong, “Methanation of carbon dioxide : an overview,” vol. 5, no. 1, pp. 2–10, 2011, doi: 10.1007/s11705-010-0528-3.

[25] H. Tian, X. Li, L. Zeng, and J. Gong, “Recent Advances on the Design of Group VIII Base-Metal Catalysts with Encapsulated Structures,” 2015, doi: 10.1021/acscatal.5b01221.

[26] International Union of Pure and Applied Chemistry (IUPAC), “RECOMMENDATIONS FOR THE Recommendations for the characterization of porous solids,” vol. 66, no. 8, pp. 1739–1758, 1994.

[27] H. Tian, S. Li, L. Zeng, H. Ma, and J. Gong, “Assembly of ordered mesoporous alumina-supported nickel nanoparticles with high temperature stability for CO methanation,” *Sci. China Mater.*, vol. 58, no. 1, pp. 9–15, 2015, doi: 10.1007/s40843-014-0014-1.

[28] C. Ding *et al.*, “One step synthesis of mesoporous NiO–Al2O3 catalyst for partial oxidation of methane to syngas: The role of calcination temperature,” *Fuel*, vol. 162, pp. 148–154,

2015, doi: 10.1016/j.fuel.2015.09.002.

[29] J. Kopyscinski, T. J. Schildhauer, and S. M. A. Biollaz, “Production of synthetic natural gas (SNG) from coal and dry biomass - A technology review from 1950 to 2009,” *Fuel*, vol. 89, no. 8, pp. 1763–1783, 2010, doi: 10.1016/j.fuel.2010.01.027.

[30] S. Rönsch *et al.*, “Review on methanation - From fundamentals to current projects,” *Fuel*, vol. 166, no. October, pp. 276–296, 2016, doi: 10.1016/j.fuel.2015.10.111.

[31] M. Rüdisüli, T. J. Schildhauer, S. M. A. Biollaz, and J. R. Van Ommen, “Scale-up of bubbling fluidized bed reactors — A review,” *Powder Technol.*, vol. 217, pp. 21–38, 2012, doi: 10.1016/j.powtec.2011.10.004.

[32] J. A. Hernandez Lalinde, K. Kofler, X. Huang, and J. Kopyscinski, “Improved kinetic data acquisition using an optically accessible catalytic plate reactor with spatially-resolved measurement techniques. Case of study: CO2 methanation,” *Catalysts*, vol. 8, no. 2, 2018, doi: 10.3390/catal8020086.

[33] Sigma-Aldrich, “MSDS - Pluronic P123,” 2017.

[34] Sigma-Aldrich, “MSDS - Nitric Acid 65 - 70 wt.%,” 2017.

[35] J. A. H. Lalinde, J. S. Jiang, G. Jai, and J. Kopyscinski, “Preparation and characterization of Ni/Al2O3 catalyst coatings on FeCrAl-loy plates used in a catalytic channel reactor with in-situ spatial profiling to study CO2 methanation,” *Chem. Eng. J.*, vol. 357, no. June 2018, pp. 435–446, 2019, doi: 10.1016/j.cej.2018.09.161.

[36] F. Haugen, “Article : Ziegler-Nichols ’ Closed-Loop Method,” no. July, pp. 1–7, 2010.

[37] National Instruments, “LabVIEW - PID and Fuzzy Logic Toolkit User Manual,” 2009.

[38] FLIR Systems, “FLIR SC2500 - Technical Specifications,” 2009.

[39] R. Fleagle and J. Businger, *An introduction to Atmosperic Physics*. 1980.

[40] M. Thommes *et al.*, “Physisorption of gases , with special reference to the evaluation of surface area and pore size distribution (IUPAC Technical Report),” 2015, doi: 10.1515/pac-2014-1117.

[41] S. J. Gregg and K. S. W. Sing, *Adsorption, Surface Area and Porosity*. Academic Press Inc., 1967.

[42] J. Landers, G. Y. Gor, and A. V Neimark, “Colloids and Surfaces A : Physicochemical and Engineering Aspects Density functional theory methods for characterization of porous materials,” *Colloids Surfaces A Physicochem. Eng. Asp.*, vol. 437, pp. 3–32, 2013, doi: 10.1016/j.colsurfa.2013.01.007.

[43] Phenom-World BV, “Phenom Pro Specification Sheet,” 2017.

[44] W. Zhou, R. P. Apkarian, and Z. L. Wang, “Fundamentals of Scanning Electron Microscopy,” in *Scanning Microscopy for Nanotechnology Techniques and Applications*, 2006.

[45] J. A. Hernandez Lalinde, P. Roongruangsree, J. Ilsemann, M. Bäumer, and J. Kopyscinski, “CO2 methanation and reverse water gas shift reaction. Kinetic study based on in situ spatially-resolved measurements,” *Chem. Eng. J.*, vol. 390, no. November 2019, p. 124629, 2020, doi: 10.1016/j.cej.2020.124629.

[46] F. Koschany, D. Schlereth, and O. Hinrichsen, “On the kinetics of the methanation of carbon dioxide on coprecipitated NiAl(O)x,” *Appl. Catal. B Environ.*, vol. 181, pp. 504–516, 2016, doi: 10.1016/j.apcatb.2015.07.026.

[47] F. D. Fairbanks and C. R. Wilke, “Diffusion Coefficients in Multicomponent Gas Mixtures,” *Ind. Eng. Chem.*, no. March, pp. 471–475, 1950, doi: 10.1021/ie50483a022.

[48] E. Fuller, P. Schettler, and C. Giddings, “A New Method For Prediction Of Binary Gas - Phase Diffusion Coefficients,” *Ind. Eng. Chem.*, vol. 58, 1966.

[49] E. N. Fuller, K. Ensley, and J. C. Giddings, “Diffusion of Halogenated Hydrocarbons in Helium - The Effect of Structure on Collision Cross Sections,” *J. Phys. Chem.*, vol. 75, no. 11, 1969, doi: 10.1021/j100845a020.

[50] I. AthenaVisual, “AthenaVisual, Inc.” https://athenavisual.com/.

[51] J. A. Hernandez Lalinde, “Investigation of CO2 methanation over order mesoporous Ni/Al2O3 catalyst using a catalytic plate reactor with spatially resolved measurement capability,” p. 190, 2019.

A

Appendices

A1 PID tuning by using Ziegler – Nichols method

The tuning process of a PID controller by using Ziegler – Nichols method follows a specific pathway: (1) Heat the reactor to a specific operating temperature, (2) deactivate the integrative and derivative term by setting each value to zero; in addition set also K_P to the starting value zero, (3) increase the proportional gain until a stable oscillation is noticed, this smallest stable value is called K_{Pu}, (4) measure the corresponding time of a period P_u and finally (5) calculate the according Ziegler – Nichols values for a PID controller whereby $K_P = 0.6 \cdot K_{Pu}$, $T_i = 0.5 \cdot P_u$ and $T_d = 0.25 \cdot T_i$ [36]. The temperature curve for the critical proportional gain is shown in Figure 3-7.

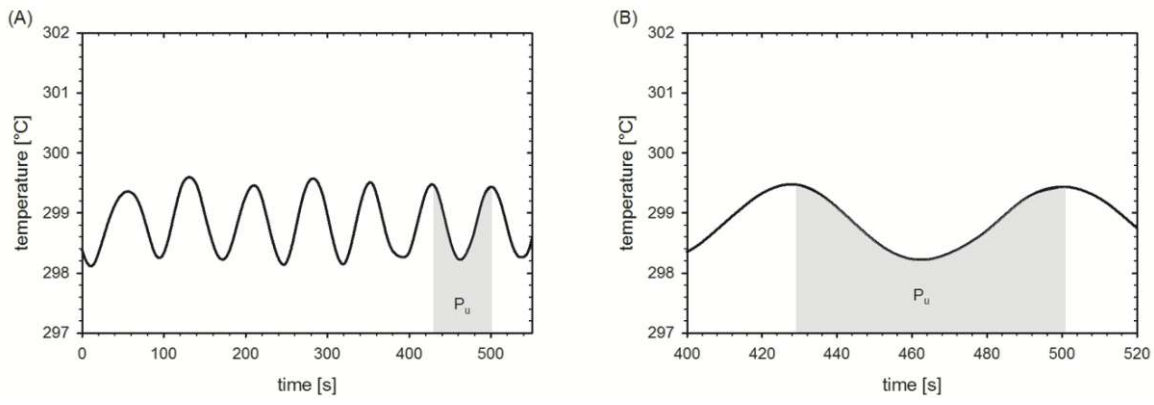

Figure A-1 Temperature profile for K_{Pu} = 13.5 (A), corresponding ultimate period (B)

B1 Athena script for modeling data

```
!**********************************Parameter Definition*****************************************
Parameter NCC = 5 As Integer
Parameter R = 8.314472 As Real

!**********************************Declaration of Variables*************************************
Global r1 As Real                          !
Global Rate(NCC) As Real                   !
Global ppsi(NCC) As Real                   !Partial pressure of species i .....[Pa]
Parameter wcat = 0.00236727  As Real       ! Catalyst mass distribution .....[kg_cat/m]
Global pH2, pCO2, pCH4, pH2O, pArg  As Real !Partial pressure of H2/CO2/CH4/H2O/Arg .....[Pa]

Global Keq1              As Real           ! Equilibrium constant for Rx1.....[differ]
Global k1, k01, Ea1      As Real           ! Kinetic constansts for Rx1 .....[differ]
Global kH,k0H,dhH        As Real           ! Adsorption constant and heat of adsorption for H2
Global kCOX,k0COX,dhCOX  As Real           ! Adsorption constant and heat of adsorption for COH/COOH
Global kOH,k0OH,dhOH     As Real           ! Adsorption constant and heat of adsorption for OH

Global mFlow(NCC) As Real                  ! molarFlow at experimental point

!**********************************Geometric Variables******************************************
Global Width     As Real                   ! Reactor width .....[m]
Global Height    As Real                   ! Reactor height .....[m]
Width   = 0.038                            ! w  = 40 mm - 2*1 mm (Fixing bars)
Height  = 0.0046                           ! h  = 4 mm + 0.6 (gasket) mm

Global Sh        As Real                   ! Sherwood number .....[-]
Global lch       As Real                   ! Characteristic diffusion length .....[m]
Sh = 3.7                                   ! Raja2000   with channel diameter .....[-]
lch = Height                               ! Channel length (to calculate Sherwood Number).....[-]

Global expPosition As Real

!**********************************Thermodynamic properties*************************************

Parameter PFeed = 2.0E5 As Real            ! Feed pressure .....[Pa]
```

```
Parameter TRef = 623.15 As Real          ! Reference (base) temperature .....[K]
Global TFeed As Real                     ! Feed temperature .....[K]
Global Tcat As Real                      ! Catalyst temperature .....[K]
Global TE As Real

!*****************************************************************************************
@Connect Variables
!*****************************************************************************************
expPosition = Xu(1)
Tcat = Xu(2)
mFlow(1) = Xu(3)
mFlow(2) = Xu(4)
mFlow(3) = Xu(5)
mFlow(4) = Xu(6)
mFlow(5) = Xu(7)

TE  = (1.0 - TRef/Tcat)
TFeed = Tcat - 5.0

k01   = exp(Par(1))      ! ln(k01)
EA1   = Par(2)           ! EA1/(R*Tbase)

k0COX = exp(Par(3))      ! ln(k0COX)
dhCOX = Par(4)           ! DCOX/(R*Tbase)

k0H   = exp(Par(5))      ! ln(k0H)
dhH   = Par(6)           ! DH/(R*Tbase)

k0OH  = exp(Par(7))      ! ln(k0OH)
dhOH  = Par(8)           ! DOH/(R*Tbase)

k1   = k01   * exp(TE * EA1)
kCOX = k0COX * exp(TE * dhCOX)
kOH  = k0OH  * exp(TE * dhOH)
kH   = k0H   * exp(TE * dhH)
```

```
!-------------------------------------------------------------------------------------
!Calculation Dij

Global Dij(NCC,NCC) As Real
Global mFracH2  As Real          ! Diffusion Volume H2 .....[m3/mol]
Global mFracCO2 As Real          ! Diffusion Volume CO2 .....[m3/mol]
Global mFracCH4 As Real          ! Diffusion Volume CH4 .....[m3/mol]
Global mFracH2O As Real          ! Diffusion Volume H2O .....[m3/mol]
Global mFracArg As Real          ! Diffusion Volume Ar .....[m3/mol]
Global vH2, vCO2, vCH4, vH2O, vArg As Real  ! Molecular weight of species .....[g/mol]

vH2  = 6.12
vCO2 = 26.7
vCH4 = 25.14
vH2O = 13.1
vArg = 16.2

Global MWH2,MWCO2,MWCH4,MWH2O,MWArg As Real  ! Molecular weight of species .....[g/mol]

MWH2 =  2.016
MWCO2 = 44.01
MWCH4 = 16.04
MWH2O = 18.01
MWArg = 39.84

! Calculation of Dij .....i = H2(1)....j = CO2(2), CO(3), CH4(4), H2O(5), Ar(6)
 Dij(1,2) = 0.01013*TFeed^1.75*(1/MWH2+1/MWCO2)^0.5/(PFeed*(vH2^(1/3)+vCO2^(1/3)))^2
 Dij(1,3) = 0.01013*TFeed^1.75*(1/MWH2+1/MWCH4)^0.5/(PFeed*(vH2^(1/3)+vCH4^(1/3)))^2
 Dij(1,4) = 0.01013*TFeed^1.75*(1/MWH2+1/MWH2O)^0.5/(PFeed*(vH2^(1/3)+vH2O^(1/3)))^2
 Dij(1,5) = 0.01013*TFeed^1.75*(1/MWH2+1/MWArg)^0.5/(PFeed*(vH2^(1/3)+vArg^(1/3)))^2

! Calculation of Dij .....i = CO2(2)....j = H2(1), CO(3), CH4(4), H2O(5), Ar(6)
 Dij(2,3) = 0.01013*TFeed^1.75*(1/MWCO2+1/MWCH4)^0.5/(PFeed*(vCO2^(1/3)+vCH4^(1/3)))^2
 Dij(2,4) = 0.01013*TFeed^1.75*(1/MWCO2+1/MWH2O)^0.5/(PFeed*(vCO2^(1/3)+vH2O^(1/3)))^2
 Dij(2,5) = 0.01013*TFeed^1.75*(1/MWCO2+1/MWArg)^0.5/(PFeed*(vCO2^(1/3)+vArg^(1/3)))^2
```

! Calculation of Dij .....i = CH4(4)....j = H2(1), CO2(2), CO(3), H2O(5), Ar(6)

Dij(3,4) = 0.01013*TFeed^1.75*(1/MWCH4+1/MWH2O)^0.5/(PFeed*(vCH4^(1/3)+vH2O^(1/3)))^2

Dij(3,5) = 0.01013*TFeed^1.75*(1/MWCH4+1/MWArg)^0.5/(PFeed*(vCH4^(1/3)+vArg^(1/3)))^2

! Calculation of Dij.....i = H2O(5)....j = H2(1), CO2(2), CO(3), CH4(4), Ar(6)

Dij(4,5) = 0.01013*TFeed^1.75*(1/MWH2O+1/MWArg)^0.5/(PFeed*(vH2O^(1/3)+vArg^(1/3)))^2

Global Dmi(NCC) As Real

Global cb(NCC) As Real

Global cs(NCC) As Real

Global MFrac(NCC) As Real

Global MFracU(NCC) As Real

Global mTotal, mTotalU As Real

Global mFlowU(NCC) As Real

mTotal = mFlow(1)+mFlow(2)+mFlow(3)+mFlow(4)+mFlow(5)

MFrac(1) = mFlow(1) / mTotal **! Molar fraction flow of H2 .....[-]**

MFrac(2) = mFlow(2) / mTotal **! Molar fraction flow of CO2 .....[-]**

MFrac(3) = mFlow(3) / mTotal **! Molar fraction flow of CH4 .....[-]**

MFrac(4) = mFlow(4) / mTotal **! Molar fraction flow of H2O .....[-]**

MFrac(5) = mFlow(5) / mTotal **! Molar fraction flow of Ar .....[-]**

! Calculation of bulk concentration ..... cb(i) = x(i)*p/(R*T)

cb(1) = MFrac(1) * PFeed / (R*TFeed) **! Molar concentration of H2...[mol/m3]**

cb(2) = MFrac(2) * PFeed / (R*TFeed) **! Molar concentration of CO2..[mol/m3]**

cb(3) = MFrac(3) * PFeed / (R*TFeed) **! Molar concentration of CH4...[mol/m3]**

cb(4) = MFrac(4) * PFeed / (R*TFeed) **! Molar concentration of H2O..[mol/m3]**

cb(5) = MFrac(5) * PFeed / (R*TFeed) **! Molar concentration of Ar..[mol/m3]**

! Calculation of catalyst concentration ..... cs(i)

cs(1) = cb(1)*0.9

cs(2) = cb(2)*0.9

cs(3) = cb(3)

cs(4) = cb(4)

cs(5) = cb(5)

! Calculation of partial pressure ..... ppsi(i) = cs(i)*R*T

ppsi(1) = cs(1) * R * Tcat / 100000 **! Partial pressure of H2 .....[bar]**

ppsi(2) = cs(2) * R * Tcat / 100000 **! Partial pressure of CO2 .....[bar]**

ppsi(3) = cs(3) * R * Tcat / 100000 **! Partial pressure of CH4 .....[bar]**

ppsi(4) = cs(4) * R * Tcat / 100000 **! Partial pressure of H2O .....[bar]**

ppsi(5) = cs(5) * R * Tcat / 100000 **! Partial pressure of Ar .....[bar]**

pH2 = ppsi(1)

pCO2 = ppsi(2)

pCH4 = ppsi(3)

pH2O = ppsi(4)

pArg = ppsi(5)

!----------

!Calculation of reaction rate (r) and rate of formation (Rate)

Keq1 = 137*Tcat^3.998*exp(158.7/(R*Tcat))

!Model HL

r1 = k1*kCOX*sqrt(pCO2)*kH*pH2*(1-(pH2O^2*pCH4/(pH2^4*pCO2*Keq1)))/((1+kCOX*sqrt(pCO2)*sqrt(kH)*sqrt(pH2)+sqrt(kH*pH2)+kOH*pH2O/sqrt(pH2))^2)

!Model 6

r1 = k1*kCOX*pCO2*sqrt(kH)*sqrt(pH2)*(1-(pH2O^2*pCH4/(pH2^4*pCO2*Keq1)))/((1+kCOX*pCO2*sqrt(kH)*sqrt(pH2)+sqrt(kH*pH2)+kOH*pH2O/sqrt(pH2))^2)

Rate(1) = -4*r1

Rate(2) = -r1

Rate(3) = r1

Rate(4) = 2*r1

Rate(5) = 0

```
!*************************************************************************************************
@Initial Conditions
!*************************************************************************************************
 U(1:5) = mFlow(1:5)
 U(6:10) = cs(1:5)



!-------------------------------------------------------------------------------------------
! Calculation of DiMix 'Dmi'
 mFlowU(1) =  U(1)
 mFlowU(2) =  U(2)
 mFlowU(3) =  U(3)
 mFlowU(4) =  U(4)
 mFlowU(5) =  U(5)

 mTotalU = mFlowU(1)+mFlowU(2)+mFlowU(3)+mFlowU(4)+mFlowU(5)
 MFracU(1) = mFlowU(1) / mTotalU        ! Molar flow of H2 .....[-]
 MFracU(2) = mFlowU(2) / mTotalU        ! Molar flow of CO2 .....[-]
 MFracU(3) = mFlowU(3) / mTotalU        ! Molar flow of CH4 .....[-]
 MFracU(4) = mFlowU(4) / mTotalU        ! Molar flow of H2O .....[-]
 MFracU(5) = mFlowU(5) / mTotalU        ! Molar flow of Ar .....[-]

 Dmi(1) = (1-MFracU(1)) / ( MFracU(2)/Dij(1,2) + MFracU(3)/Dij(1,3) + MFracU(4)/Dij(1,4) + MFracU(5)/Dij(1,5) )
 Dmi(2) = (1-MFracU(2)) / ( MFracU(1)/Dij(1,2) + MFracU(3)/Dij(2,3) + MFracU(4)/Dij(2,4) + MFracU(5)/Dij(2,5) )
 Dmi(3) = (1-MFracU(3)) / ( MFracU(1)/Dij(1,3) + MFracU(2)/Dij(2,3) + MFracU(4)/Dij(3,4) + MFracU(5)/Dij(3,5) )
 Dmi(4) = (1-MFracU(4)) / ( MFracU(1)/Dij(1,4) + MFracU(2)/Dij(2,4) + MFracU(3)/Dij(3,4) + MFracU(5)/Dij(4,5) )
 Dmi(5) = (1-MFracU(5)) / ( MFracU(1)/Dij(1,5) + MFracU(2)/Dij(2,5) + MFracU(3)/Dij(3,5) + MFracU(4)/Dij(4,5) )

!*************************************************************************************************
@Model Equations
!*************************************************************************************************
 F(1)  = U(1) - Sh * Dmi(1) * Width / lch * (cb(1)-U(6))
 F(2)  = U(2) - Sh * Dmi(2) * Width / lch * (cb(2)-U(7))
 F(3)  = U(3) - Sh * Dmi(3) * Width / lch * (cb(3)-U(8))
 F(4)  = U(4) - Sh * Dmi(4) * Width / lch * (cb(4)-U(9))
```

```
F(5)  = U(5) - Sh * Dmi(5) * Width / lch * (cb(5)-U(10))

F(6)  = Sh * Dmi(1) * Width / lch * (cb(1)-U(6))  + wcat * Rate(1)
F(7)  = Sh * Dmi(2) * Width / lch * (cb(2)-U(7))  + wcat * Rate(2)
F(8)  = Sh * Dmi(3) * Width / lch * (cb(3)-U(8))  + wcat * Rate(3)
F(9)  = Sh * Dmi(4) * Width / lch * (cb(4)-U(9))  + wcat * Rate(4)
F(10) = Sh * Dmi(5) * Width / lch * (cb(5)-U(10)) + wcat * Rate(5)

!*****************************************************************************************
@Coefficient Matrix
!*****************************************************************************************
 E(1)  = 1.0
 E(2)  = 1.0
 E(3)  = 1.0
 E(4)  = 1.0
 E(5)  = 1.0

 E(6)  = 0.0        ! algebraic equation for the catalyst phase
 E(7)  = 0.0        ! algebraic equation for the catalyst phase
 E(8)  = 0.0        ! algebraic equation for the catalyst phase
 E(9)  = 0.0        ! algebraic equation for the catalyst phase
 E(10) = 0.0        ! algebraic equation for the catalyst phase

!*****************************************************************************************
@Response Model
!*****************************************************************************************
 Dim mFlowTotal As Real
 mFlowTotal = U(1)+U(2)+U(3)+U(4)+U(5)

 Y(1) = U(3)/mFlowTotal*100       ! molar flow of methane .....[mol%]
```

C1 Rate equations for mechanism B

B1:	$r_1 = k_1 \cdot p_{H_2} \cdot \Theta_v^2$ $r_1' = k_1' \cdot \Theta_H^2$	$\Theta_H = \sqrt{K_1 \cdot p_{H_2}} \cdot \Theta_v$	**AC1-1**
B2:	$r_2 = k_2 \cdot p_{CO_2} \cdot \Theta_v$ $r_2' = k_2' \cdot \Theta_{CO_2}$	$\Theta_{CO_2} = K_2 \cdot p_{CO_2} \cdot \Theta_v$	**AC1-2**
B3:	$r_3 = k_3 \cdot p_{CO_2} \cdot \Theta_v^2$ $r_3' = k_3' \cdot \Theta_{CO} \cdot \Theta_O$	$\Theta_{CO} \cdot \Theta_O = K_3 \cdot p_{CO_2} \cdot \Theta_v^2$	**AC1-3**
B4:	$r_4 = k_4 \cdot \Theta_{CO_2} \cdot \Theta_H$ $r_4' = k_4' \cdot \Theta_{COOH} \cdot \Theta_v$	$\Theta_{COOH} = K_4 \cdot \frac{\Theta_{CO_2} \cdot \Theta_H}{\Theta_v}$	**AC1-4**
B5:	$r_5 = k_5 \cdot \Theta_{COOH} \cdot \Theta_v$ $r_5' = k_5' \cdot \Theta_{COH} \cdot \Theta_O$	$\Theta_{COH} = K_5 \cdot \frac{\Theta_{COOH} \cdot \Theta_v}{\Theta_O}$	**AC1-5**
B6:	$r_6 = k_6 \cdot \Theta_{CO} \cdot \Theta_H$ $r_6' = k_6' \cdot \Theta_{COH} \cdot \Theta_v$	$\Theta_{COH} = K_6 \cdot \frac{\Theta_{CO} \cdot \Theta_H}{\Theta_v}$	**AC1-5**
B7:	$r_7 = k_7 \cdot \Theta_{COH} \cdot \Theta_v$ $r_7' = k_7' \cdot \Theta_{CH} \cdot \Theta_O$	$\Theta_{CH} = K_7 \cdot \frac{\Theta_{COH} \cdot \Theta_v}{\Theta_O}$	**AC1-6**
B8:	$r_8 = k_8 \cdot \Theta_{CH} \cdot \Theta_v$ $r_8' = k_8' \cdot \Theta_{CH_2} \cdot \Theta_v$	$\Theta_{CH_2} = K_8 \cdot \frac{\Theta_{CH} \cdot \Theta_H}{\Theta_v}$	**AC1-7**
B9:	$r_9 = k_9 \cdot \Theta_{CH_2} \cdot \Theta_H$ $r_9' = k_9' \cdot \Theta_{CH_3} \cdot \Theta_v$	$\Theta_{CH_3} = K_9 \cdot \frac{\Theta_{CH_2} \cdot \Theta_H}{\Theta_v}$	**AC1-8**
B10:	$r_{10} = k_{10} \cdot \Theta_{CH_3} \cdot \Theta_H$ $r_{10}' = k_{10}' \cdot \Theta_{CH_4} \cdot \Theta_v$	$\Theta_{CH_4} = K_{10} \cdot \frac{\Theta_{CH_3} \cdot \Theta_H}{\Theta_v}$	**AC1-9**
B11:	$r_{11} = k_{11} \cdot \Theta_{CH_4}$ $r_{11}' = k_{11}' \cdot \mathrm{p}_{CH_4} \cdot \Theta_v$	$\Theta_{CH_4} = K_{11} \cdot \mathrm{p}_{CH_4} \cdot \Theta_v$	**AC1-10**
B12:	$r_{12} = k_{12} \cdot \Theta_O \cdot \Theta_H$ $r_{12}' = k_{12}' \cdot \Theta_{OH} \cdot \Theta_v$	$\Theta_O \cdot \Theta_H = K_{12} \cdot \Theta_{OH} \cdot \Theta_v$	**AC1-11**
B13:	$r_{13} = k_{13} \cdot \Theta_{OH} \cdot \Theta_H$ $r_{13}' = k_{13}' \cdot \Theta_{H_2O} \cdot \Theta_v$	$\Theta_{OH} = K_{13} \cdot \frac{\Theta_{H_2O} \cdot \Theta_v}{\Theta_H}$	**AC1-12**
B14:	$r_{14} = k_{14} \cdot \Theta_{H_2O}$ $r_{14}' = k_{14}' \cdot \mathrm{p}_{H_2O} \cdot \Theta_v$	$\Theta_{H_2O} = K_{14} \cdot \mathrm{p}_{H_2O} \cdot \Theta_v$	**AC1-13**